University of New Mexico
UNM Digital Repository

Fall 11-15-2018

Frameworks to Investigate Robustness and Disease Characterization/Prediction Utility of Time-Varying Functional Connectivity State Profiles of the Human Brain at Rest

Anees Abrol

Doctoral Student, Electrical Engineering

Recommended Citation

Anees Abrol

Candidate

Electrical and Computer Engineering

Department

This dissertation is approved, and it is acceptable in quality and form for publication:

Approved by the Dissertation Committee:

Dr. Vince D. Calhoun, Chairperson

Dr. Ramiro Jordan

Dr. Manel Martinez-Ramon

Dr. Robyn L. Miller

FRAMEWORKS TO INVESTIGATE ROBUSTNESS AND DISEASE CHARACTERIZATION/PREDICTION UTILITY OF TIME-VARYING FUNCTIONAL CONNECTIVITY STATE PROFILES OF THE HUMAN BRAIN AT REST

by

ANEES ABROL

B.E., Panjab University, 2010
M.E.S., Auckland University of Technology, 2012

DISSERTATION

Submitted in Partial Fulfillment of the
Requirements for the Degree of

**Doctor of Philosophy
Engineering**

The University of New Mexico
Albuquerque, New Mexico

December 2018

DEDICATION

This work is dedicated to my parents, Rita Abrol and Vijay Abrol, for their eternal love and support. The grace in their perpetual encouragement to shine like a sun and unfurl like a rainbow in tough times of life has led my way so far!

ACKNOWLEDGEMENTS

FRAMEWORKS TO INVESTIGATE ROBUSTNESS AND DISEASE CHARACTERIZATION/PREDICTION UTILITY OF TIME-VARYING FUNCTIONAL CONNECTIVITY STATE PROFILES OF THE HUMAN BRAIN AT REST

by

Anees Abrol

B.E., Panjab University, 2010

M.E.S., Auckland University of Technology, 2012

Ph.D., Engineering, University of New Mexico, 2018

ABSTRACT

Neuroimaging technologies aim at delineating the highly complex structural and functional organization of the human brain. In recent years, several unimodal as well as multimodal analyses of structural MRI (sMRI) and functional MRI (fMRI) neuroimaging modalities, leveraging advanced signal processing and machine learning based feature extraction algorithms, have opened new avenues in diagnosis of complex brain syndromes and neurocognitive disorders. Generically regarding these neuroimaging modalities as filtered, complimentary insights of brain's anatomical and functional organization, multimodal data fusion efforts could enable more comprehensive mapping of brain structure and function.

Large scale functional organization of the brain is often studied by viewing the brain as a complex, integrative network composed of spatially distributed, but functionally interacting, sub-networks that continually share and process information. Such whole-brain

functional interactions, also referred to as patterns of functional connectivity (FC), are typically examined as levels of synchronous co-activation in the different functional networks of the brain. More recently, there has been a major paradigm shift from measuring the whole-brain FC in an oversimplified, time-averaged manner to additional exploration of time-varying mechanisms to identify the recurring, transient brain configurations or brain states, referred to as time-varying FC state profiles in this dissertation. Notably, prior studies based on time-varying FC approaches have made use of these relatively lower dimensional fMRI features to characterize pathophysiology and have also been reported to relate to demographic characterization, consciousness levels and cognition.

In this dissertation, we corroborate the efficacy of time-varying FC state profiles of the human brain at rest by implementing statistical frameworks to evaluate their robustness and statistical significance through an in-depth, novel evaluation on multiple, independent partitions of a very large rest-fMRI dataset, as well as extensive validation testing on surrogate rest-fMRI datasets. In the following, we present a novel data-driven, blind source separation based multimodal (sMRI-fMRI) data fusion framework that uses the time-varying FC state profiles as features from the fMRI modality to characterize diseased brain conditions and substantiate brain structure-function relationships. Finally, we present a novel data-driven, deep learning based multimodal (sMRI-fMRI) data fusion framework that examines the degree of diagnostic and prognostic performance improvement based on time-varying FC state profiles as features from the fMRI modality. The approaches developed and tested in this dissertation evince high levels of robustness and highlight the utility of time-varying FC state profiles as potential biomarkers to characterize, diagnose and predict diseased brain conditions. As such, the findings in this work argue in favor of the view of FC investigations of the brain that are centered on time-varying FC approaches, and also highlight the benefits of combining multiple neuroimaging data modalities via data fusion.

CONTENTS

LIST OF FIGURES

Chapter 1: Introduction

1.1 Significance of the Problem

Neuroimaging technologies aim at delineating the highly complex structural and functional organization of the human brain. Structural neuroimaging modalities evaluate anatomical brain structure and tissue type (e.g. structural MRI or sMRI) or brain tissue microstructure (e.g. diffusion MRI), whereas functional neuroimaging modalities indirectly estimate brain function/activity through respective characteristic "source signals" or "indicators" of the underlying neuronal (e.g. electroencephalography, magnetoencephalography), metabolic (e.g. positron emission tomography) or hemodynamic (e.g. functional MRI or fMRI) activity. In recent years, several unimodal as well as multimodal analyses of the sMRI and fMRI neuroimaging modalities, leveraging advanced signal processing and machine learning based feature extraction algorithms, have opened new avenues in diagnosis of complex mental syndromes such as schizophrenia, bipolar disorder, depression, anxiety, etc., neurocognitive degenerative disorders such as Alzheimer's disease (AD), Huntington's disease, Parkinson's disease, multiple sclerosis, etc., developmental brain disorders such as autism spectrum disorder, attention deficit hyperactivity disorder, dyslexia, etc., and other trauma, breathing, cardiovascular, metabolic, and drug and alcohol related brain disorders.

The fMRI neuroimaging modality is commonly used to detect and delineate brain regions that change their activation levels in response to experimental paradigms (task-based fMRI) or in the resting state (rest-fMRI). In fMRI studies, the large scale functional organization of the brain is often studied by viewing the brain as a complex, integrative

network composed of spatially distributed, but functionally interacting, sub-networks that continually share and process information. Progressively, the whole-brain functional inter-relationships amongst these spatially distinct functional networks of the brain, for example, how different brain regions couple to establish a specific function of the brain, etc., are typically studied as levels of their synchronous co-activation. In neuroimaging literature, these functional inter-relationships are widely referred to as functional connectivity (FC) between the different functional networks of the brain.

Studies assessing FC primarily leverage popular approaches such as seed-based correlation analysis (SCA) and spatial independent component analysis (ICA) to decompose the preprocessed fMRI brain signals into distributed functional networks exhibiting high temporal correlation in intrinsic activity. Followingly, the statistical properties of the temporal activations estimated for these functional networks (i.e. functional network time-courses) are studied to evaluate whole-brain FC measures. More recently, there has been a major paradigm shift from measuring the whole-brain FC and associated summary statistics in an oversimplified, time-averaged manner to additional exploration of time-varying mechanisms to identify the recurring, transient "brain configurations" or "brain states", referred to as "time-varying FC state profiles" in this work, that we discuss in detail in the next paragraph. Analysis of the temporal dynamics of the estimated network time-courses is generally carried on by applying a sliding window correlation (SWC) approach, although other approaches such as phase synchronization (PS), dynamic conditional correlation (DCC), co-activation patterns (CAP), time-frequency coherence, etc. have also been proposed.

Most of the previous time-varying FC work has used the SWC method to evaluate inter-network temporal FC by calculating the correlation between the network time-courses at all time-points within a chosen window and repeating the process by gradually moving the window through the scan length. This essentially results in window-indexed correlation matrices that record snapshots of inter-network FC evolving in time. FC analysis using the SWC method is often proceeded by a rigorous FC state profile estimation and characterization process using clustering or blind source signal separation algorithms, wherein, as discussed in the previous paragraph, the FC state profiles are referred to the distinct discrete, transient patterns of FC, conceptually analogous to the quasi-stable EEG microstates. The estimated whole-brain FC state profiles represent transient patterns of FC that vary over time; it has been reported that subjects tend to remain in the same FC state profile for lengthy periods of time before transitioning to one of the other state profiles (i.e. transitions occur after multiple time samples). Notably, prior studies based on time-varying FC approaches have made use of these relatively lower dimensional fMRI features to characterize pathophysiology (i.e. identification of disease states), reported better diagnostic performance than time-averaged assessments of FC, and have also been reported to relate to demographic characterization, consciousness levels and cognition.

Furthermore, generically regarding the different neuroimaging modalities as filtered, complimentary insights of brain's anatomical and functional organization, multimodal data fusion efforts could enable more comprehensive mapping of brain structure and function. Studies featuring multimodal neuroimaging data fusion for understanding brain function and structure, or disease characterization, leverage the partial information available in each of the modalities to reveal data variations not exhibited

through the independent analyses. Several previous studies have suggested interactions between anatomical and functional connectivity of the brain, and it is reasonable to hypothesize covariation between feature spaces of a structural and functional modality. The joint information on such interactions between the feature spaces is extracted through model-driven or data-driven multimodal fusion approaches based on linear mixture models that differ in the optimization strategies they evolve the data sources through as well as in their basic limitations. Evidently, multimodal studies with advanced signal processing, machine learning and statistical modeling methods assume greater significance in diagnosis of complex brain syndromes and disorders that usually feature striking pathological and etiological heterogeneity.

Studies leveraging such multimodal data fusion approaches have revealed significant information on clinical aspects of complex brain syndromes and disorders. The previously discussed, promising success of time-varying FC state profiles in recent neuroimaging literature suggest them to be powerful features in scope of the fMRI modality. Using these as features from the fMRI modality in a multimodal fusion study based on advanced signal processing and machine learning approaches can be useful to explore where and how brain structure corresponds to these time-varying functional connections. This can significantly improve our understanding of the brain and help in characterization of diseased brain conditions.

Advanced machine learning approaches are now being increasingly used to process and reduce dimensionality of the very high dimensional neuroimaging data since they allow for information extraction at the level of the individual thus making them capable of assisting the investigator in diagnostic and prognostic decision-making of the patients. The

last few years have seen an emergence of deep structured or hierarchical computational learning architectures to automatically learn optimal data representations through a series of non-linear transformations on the input data space to enhance diagnostic classification performance as well as predicting cognitive decline. These architectures hierarchically learn multiple levels of abstract data representations at the multiple cascaded layers, making them more suitable to learn subtle differences in the data. Proven superiority of these deep architectures in the broader imaging community motivates their exploration on neuroimaging data. Previous multimodal studies have reported prediction performance improvements with use of multiple modalities as compared to a single studied modality; hence, such architectures could be utilized in a multimodal fusion framework to generate a collective feature space for identifying brain regions most discriminative of a disease as well as predicting a patient's chances of progressing to a specific disease after a given time-period. Fusing time-varying state profiles (as features from fMRI modality) with non-linear features extracted from rigorously training a structural data modality such as sMRI on a deep learning framework could be reasonably hypothesized to enhance the diagnostic or predictive precision.

Overall, despite fundamental evidence of availability of considerable, interesting spatiotemporal dynamic connectivity information through these time-varying FC approaches, the robustness and statistical significance of the estimated time-varying whole-brain FC profiles and associated statistical measures is yet not clear. Additionally, their utility as features for multimodal frameworks based on fMRI and sMRI modalities, and aimed at characterizing and predicting diseased brain conditions, has been sparingly explored. Indeed, these research topics assume critical importance in neuroimaging

literature in paving way for future methodological developments towards characterization of temporal coupling of the human brain, a research topic of high significance to learn how the human brain works and reveal how its functionality is altered under different disease conditions.

1.2 Dissertation Statement

This Ph.D. dissertation will implement advanced signal processing and machine learning based frameworks to estimate time-varying FC state profiles from rest-fMRI data, investigate robustness and statistical significance of these estimated time-varying FC state profiles and associated state summary measures using extensive validation testing on real and surrogate rest-fMRI data, and develop advanced signal processing and machine learning based frameworks to evaluate their utility for several applications such as disease characterization, establishing brain structure-function relationships, and enhancing diagnostic and prognostic power of neuroimaging data.

1.2.1 Research Aims and Contributions

The specific research aims and expected contributions of this Ph.D. dissertation are listed below:

1. The first aim of this Ph.D. dissertation is to corroborate the efficacy of time-varying FC state profiles of the human brain at rest by implementing statistical frameworks to evaluate their robustness and statistical significance through an in-depth, novel evaluation on multiple, independent partitions of a very large resting state fMRI dataset, as well as extensive validation testing on surrogate rest-fMRI datasets. Such corroborating evidence is of utmost importance to (a) the neuroimaging

literature at the current stage where several studies involve use of time-varying

approaches to study FC, and (b) the ongoing debate of nature and properties of

fMRI features extracted through use of time-varying approaches.

2. The second aim of this Ph.D. dissertation is to develop a novel data-driven, blind

source separation based multimodal (sMRI-fMRI) data fusion framework that uses

the time-varying FC state profiles as features from the fMRI modality to

characterize diseased brain conditions and substantiate brain structure-function

relationships. This development highlights (a) the utility of these fMRI features for

disease characterization and identification of critical brain structure-function inter-

relationships disrupted during the course of a disease, and (b) the benefits of using

the additional information available in the augmented (i.e. fused) domain for such

disease characterization objectives.

3. The final aim of this Ph.D. dissertation is to develop a deep learning based

multimodal (sMRI-fMRI) fusion framework to examine the degree of diagnostic

and prognostic performance improvement based on time-varying FC state profiles

as features from the fMRI modality. This development highlights (a) the utility of

these fMRI features for disease diagnosis and making future predictions of disease

risk, (b) the advantages of using deep learning approaches for feature extraction to

make such predictions, and (c) the advantages of making such predictions in the

augmented (i.e. fused) domain space.

1.3 Outline of the Dissertation Structure

In this section, we discuss the outline of the rest of this dissertation. Chapter 2 presents a brief background of the fundamentals of the data modalities studied, data decomposition, data fusion and deep learning algorithms implemented, and time-varying statistical frameworks explored to estimate whole-brain FC in this work.

After the brief review of the background information, the next four chapters (Chapters 3, 4, 5 and 6) include details of the major aspects of this dissertation. Chapter 3 presents an in-detail evaluation of replicability of the time-varying FC state profiles and associated summary measures as estimated using two independent time-varying FC estimation frameworks. Chapter 4 demonstrates the statistical significance of the above time-varying FC measures by extensive internal and external validation in both tested dynamic frameworks.

Chapter 5 demonstrates a disease characterization framework based on multimodal fusion of the sMRI and fMRI modalities. This framework proposes use of the time-varying FC state profiles as features from the fMRI modality with an objective of revealing and understanding disrupted links in brain structure and function in the diseased brain.

Followingly the discussion on the data fusion for disease characterization work, Chapter 6 presents details of the novel deep learning based multimodal fusion framework that leverages the gray-matter and time-varying FC state profiles feature spaces to make future predictions on healthy and diseased brain conditions.

Finally, Chapter 7 provides a conclusion of the significant established contributions of the work undertaken in this dissertation, followed by a discussion of the scope of future work.

1.4 List of Publications

This dissertation interpolates material from my published, under review and in preparation manuscripts as referenced below. Apart from the chapters listed below, some of the material from the referenced work has also been included in Chapters 1, 2 and 7.

Chapter 3 and 4: Abrol, Chaze et al. (2016), Abrol, Damaraju et al. (2017)

Chapter 5: Abrol, Rashid et al. (2017)

Chapter 6: Abrol, Bhattarai et al. (2018), Abrol, Fu et al. (2018), Abrol, Rokham et al. (2018)

Chapter 2: Background

2.1 Magnetic Resonance Imaging

Magnetic Resonance Imaging (MRI) is a non-invasive medical imaging technique that uses a strong magnetic field, electrical field gradient and radio waves to record detailed cross-sectional images of the body's internal anatomical structures and physiological processes. Currently, it can be regarded as the most sensitive non-invasive imaging test of the brain in clinical practice and is used to diagnose conditions including tumors, stroke, abnormalities, hemorrhage, seizures, dementia, and several other conditions attributable to disorders in the brain.

Structural MRI (sMRI) and functional MRI (fMRI) are two commonly used MRI modalities that are intrinsically dissimilar in acquisition and nature. While the sMRI neuroimaging modality measures the static anatomy or morphology of the brain by estimating the volumes of different brain tissues or fluids such as gray matter, white matter and cerebrospinal fluid, the fMRI modality provides the dynamic physiological information in an indirect way by recording changes in blood-oxygen levels and blood flow measures in response to neural activity in the brain. The brain morphology and functional connectivity both change considerably during childhood and adolescence, and often in old age and under different psychiatric or dementia conditions as well; hence, both modalities are being increasingly studied to identify these changes, although sMRI is more commonplace because of more established research findings and relative ease of interpretation. Furthermore, the sMRI scans are high resolution images and are often used

as a reference for multiple pre-processing steps such as co-registration, normalization and segmentation of the raw fMRI images onto a standard space. The standard preprocessing pipelines implemented on the raw sMRI and fMRI data involve a series of preprocessing operations as outlined in Figure 2-1.
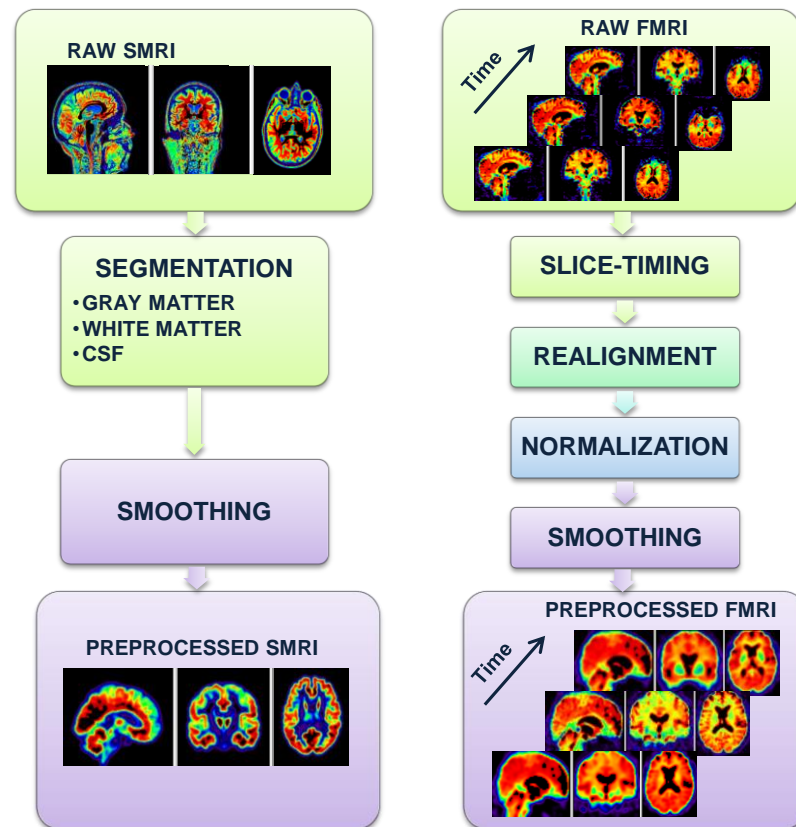
Figure 2-1: Standard preprocessing pipelines for sMRI and fMRI data.

The most extensively recorded form of fMRI uses blood-oxygenation-level-dependent (BOLD) contrast to highlight changes in blood flow related to energy consumed by brain cells (i.e. hemodynamic response). The recorded fMRI data is obscured by various noise sources that necessitate a series of statistical procedures to de-noise the underlying signal. This modality is used to study the functional activations induced due to some

experimental stimuli (i.e. task-based fMRI) or in task-free (or task-negative) resting state of the human brain (rest-fMRI). Task-based fMRI is primarily targeted at identification of brain networks that activate and/or deactivate in a specific task performance. Rest-fMRI investigates brain's functional organization in absence of a task thus making the overall analysis challenging because of the absence of any differential behavioral performance and often needs sophisticated data processing and a large number of time samples to be recorded. However, absence of task makes rest-fMRI an attractive option for patients with severe psychiatric and neurological disorders, since they are likely to experience problems in following task instructions. In fact, rest-fMRI has generally been found to be useful in identifying group differences in multiple patient groups.

2.2 Functional Segregation, Integration and Connectivity

Functional segregation, integration and connectivity are three key concepts to understand the functional organization of the brain. Functional segregation refers to process of parcellating the brain into multiple regions according to their specific functions. Several atlas-based, seed-based, clustering/decomposition based (for example, spatial group ICA) and graph theory based parcellation schemes have been used in recent fMRI studies. Despite the unconstrained nature of the resting state experiments, these different parcellations have confirmed overwhelming evidence of reproducibility (both in context to anatomy and function) in the segregated brain networks at multiple spatial and temporal scales. Fundamental, network theory-based toy as well brain-space demonstrations of functional segregation adapted from Sporns (2013) are shown in Figure 2-2a and Figure 2-2c.

Functional Segregation **Functional Integration**
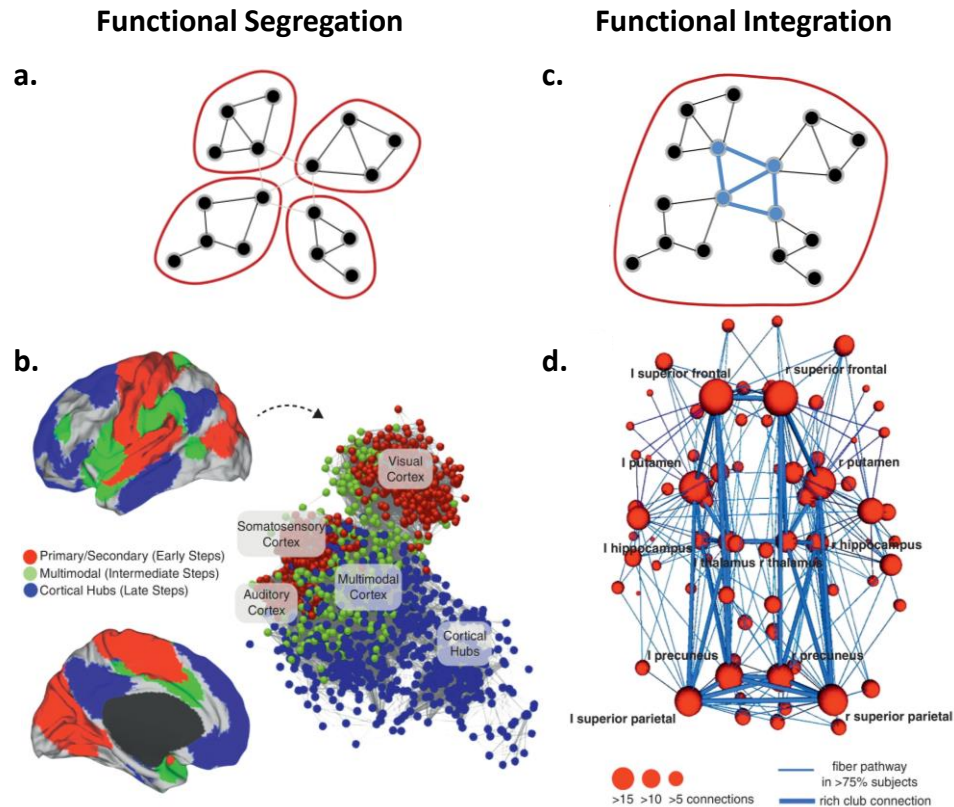
Figure 2-2: Network theory based schematic representation of functional segregation and integration. (a) Functional segregation is specified in this toy network by strong functional coupling within communities (in red boundaries) with little functional coupling across communities; (b) Visualization of parcellation (functional segregation) of the brain; (c) Functional integration is specified in this toy network by globally high levels of functional coupling between the hub connections, and (d) Visualization of the functional integration in the brain space with thick lines showing connections between hubs. Such connections are central to understand the higher order cognitive and behavioral functioning of the brain. This figure has been used from Sporns (2013) with permission.

On the other hand, functional integration refers to the process of estimating interactions between the segregated brain regions to understand higher order cognitive and behavioral functioning of the brain. Network theory-based demonstrations of functional integration adapted from Sporns (2013) are shown in Figure 2-2b and Figure 2-2d. Understanding the segregative and the integrative properties of the human brain that associate to healthy or impaired cognition is one of the critical goals of neuroscience.

BOLD-fMRI is a powerful modality to evaluate brain function, wherein functional integration of the brain is studied as patterns of functional connectivity (FC) between different brain regions. FC patterns are typically assessed as a measure of covariance between BOLD time series corresponding to the parcellated brain regions. FC studies are usually targeted at quantification of integrative relationships between the different brain regions amidst possible, multiple noise confounds. Studying FC allows us to identify how different brain regions couple to establish a specific function of the brain. Previous fMRI studies have used FC estimates as a tool to understand the functional organization of both the healthy and the diseased brain. Details of FC evaluations are discussed in more detail in a later section of this chapter.

2.3 Identification of Resting State Networks

Studies assessing FC primarily leverage seed-based correlation analysis (SCA) and spatial independent component analysis (ICA) to decompose brain signals into distributed networks exhibiting high temporal correlation in intrinsic activity. SCA decompositions feature computation of pairwise correlation in time-courses corresponding to the predefined brain regions of interest (Biswal, Yetkin et al. 1995, Fox, Snyder et al. 2005). Several pre-defined ROI atlases such as the automated anatomical labeling atlas (Tzourio-Mazoyer, Landeau et al. 2002), the Talairach and Tournoux atlas (Lancaster, Woldorff et al. 2000), the Eickhoff-Zilles atlas (Eickhoff, Stephan et al. 2005), the Harvard-Oxford atlas (Makris, Goldstein et al. 2006), and the Craddock atlas (Craddock, James et al. 2012) are leveraged to set up seeds for which pairwise functional connectivity is estimated. These seed-based approaches have been largely successful in revealing useful information on brain-wide FC. Another widely used method in estimating seeds is the spatial ICA

decomposition method (McKeown, Makeig et al. 1998, McKeown and Sejnowski 1998) that allows for measurement of network connectivity in multiple data-driven regions of interest. This method yields consistent spatially segregated and functionally homogeneous resting state networks (RSNs) by exploiting independence in the spatial domain as opposed to assessment of fixed brain voxels. Consequently, current multi-subject studies frequently make use of the group ICA (gICA) technique (Calhoun, Adali et al. 2001) for extracting brain networks while retaining individual subject variability (Erhardt, Rachakonda et al. 2011, Allen and Calhoun 2012, Allen, Erhardt et al. 2012).

Despite the unconstrained nature of the resting state experiments, the distributed networks or signal variations exhibiting temporal correlation in resting state fMRI decompositions, referred to as RSNs, have been proven to demonstrate high levels of reproducibility thus suggesting a common architecture for the functional connectome (Damoiseaux, Rombouts et al. 2006, Fox and Raichle 2007, Margulies, Kelly et al. 2007, Shehzad, Kelly et al. 2009, Smith, Fox et al. 2009, Van Dijk, Hedden et al. 2010, Zuo, Kelly et al. 2010, Dansereau, Benhajali et al. 2017). Additionally, consistency in the baseline functional activity of the brain (Damoiseaux, Rombouts et al. 2006) and reliability in some rest-fMRI measurements (Zuo and Xing 2014) has been suggested. Although there is a low degree of consensus on linkage of fMRI fluctuations with neural activity, there is rapidly growing literature providing evidence of association of the decomposed RSNs to underlying neuronal connectivity (Mantini, Perrucci et al. 2007, He, Snyder et al. 2008, Shmuel and Leopold 2008, Britz, Van De Ville et al. 2010, de Pasquale, Della Penna et al. 2010) which motivates investigations of spontaneous FC using rest-fMRI data with great optimism.

In this work, the group spatial ICA method has been used to parcellate the brain into functional networks. We discuss this method in detail in the following sub-section.

2.3.1 Group Spatial ICA on fMRI Data

ICA is a multivariate decomposition technique to separate additive but statistically independent sources. This promising blind source separation method is being increasingly applied to the fMRI data to identify independent data sources in space (spatial ICA) or time (temporal ICA). Spatial ICA on fMRI data determines a set of brain components (functional networks) that are maximally spatially independent of each other, each associated with a time-course. Group spatial ICA (Calhoun, Adali et al. 2001) allows for extraction of brain networks while retaining maximum individual subject variability and is being increasingly used in multi-subject studies. A schematic diagram of group ICA implementation is provided in Figure 2-3.

Group spatial ICA (GICA) as implemented in the GIFT toolbox has been used in several parts and stages of this work. The fMRI data for multiple subjects is stacked in the time dimension and reduced in two steps before the group-level (i.e. aggregate) independent components are estimated. In the first data reduction step, a subject-level principal component analysis (PCA) reduces the temporal dimension of fMRI data by selecting a subset the principal components that explain most of the variation for each subject. This is followed by the second data reduction step where a group-level PCA is implemented on the concatenated subject-specific principal components. This dual dimension reduction allows for maximal retention of subject-level variance. Following dimensionality reduction, the aggregate independent components are identified by

implementing the Infomax ICA method on the group-level reduced data and running ICCASO (Himberg, Hyvarinen et al. 2004) algorithm to stabilize the estimated components. The estimated independent components represent the group-level spatial maps of the resting state functional networks (i.e. the RSNs), whereas the associated mixing matrix represents the group-level activation time-courses for the identified RSNs. Finally, subject-specific estimates of the spatial maps and time-courses are obtained by GICA back-reconstruction algorithm that features spatiotemporal regression.
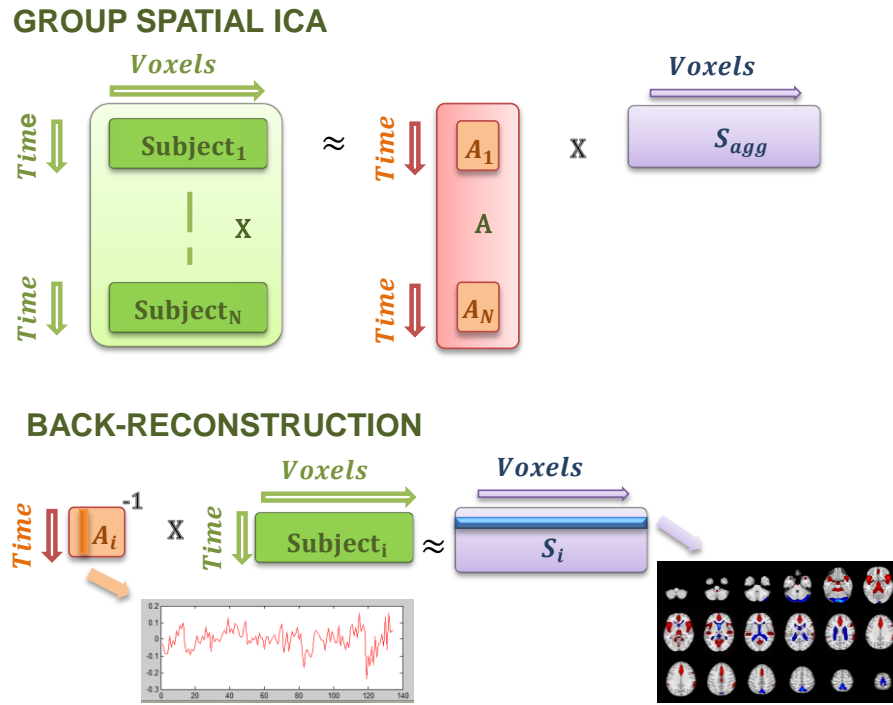
Figure 2-3: Schematic diagram of spatial group ICA including the back-reconstruction process as adapted from Calhoun, Liu et al. (2009). Spatial group ICA decomposes the fMRI data X (subjects stacked in the time dimension) into aggregate sources S_{agg} mixed by the mixing matrix A. In a following step, subject-specific spatial maps are back-reconstructed by projecting inverse of the subject-specific mixing matrix on the subject's fMRI data. The subject-specific time-courses are estimated from these subject-specific spatial maps in a following step.

In summary, group spatial ICA (GICA) allows decomposition of the preprocessed fMRI data into group-level RSN spatial maps and time-courses, following which GICA back-reconstruction or spatiotemporal regression allows for estimation of subject-specific RSN spatial maps and time-courses. Importantly, it is the estimated subject-specific RSN time-courses that are studied in whole-brain FC assessments.

2.4 Whole-brain Functional Connectivity

Whole-brain FC is often summarized as a set of FCs between all possible pairs of RSNs and can be estimated from the subject-specific RSN time-courses in a time-averaged or time-varying manner as discussed in the following sub-sections.
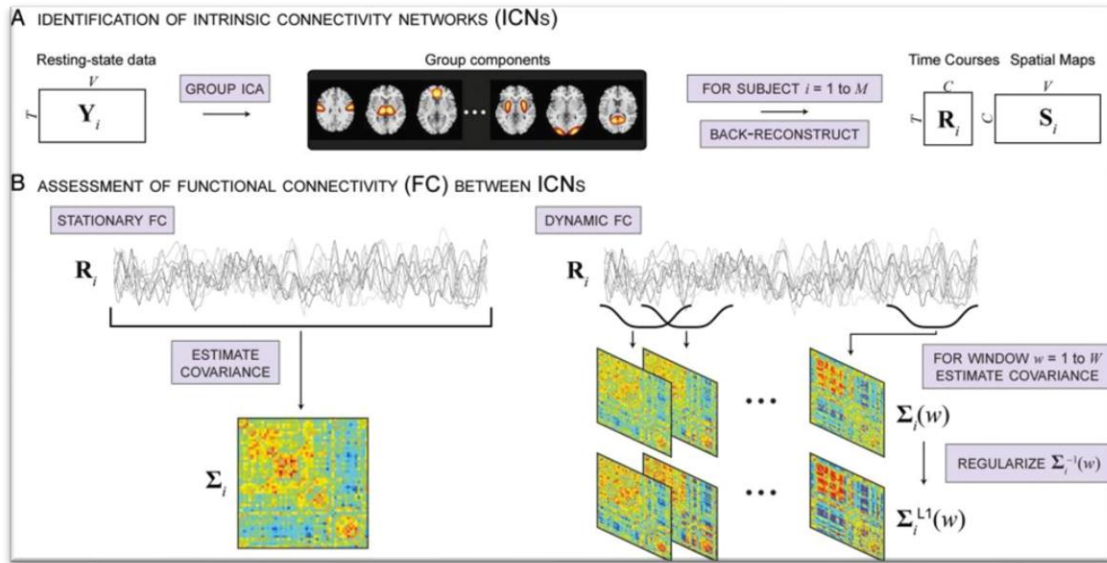
Figure 2-4: An illustration of time-averaged and time-varying FC analyses. (A) The rest-fMRI data is decomposed by group ICA into resting state networks (RSNs) and GICA back reconstruction is used to estimate the subject-specific spatial maps (S_i) and RSN time-courses (R_i) from the estimated aggregate RSN spatial maps in the first step. (B) A typical time-varying approach estimates the covariance of the RSN time-courses (R_i). On the other hand, a typical sliding-window based approach estimates time-varying connectivity as a series of regularized covariance matrices from windowed portions of (R_i). This figure has been reused from Allen, Damaraju et al. (2012).

2.4.1 Time-Averaged vs. Time-Varying FC

Time-averaged FC assessments assume that FC is relatively static in the resting brain. This assumption has been challenged by time-varying FC approaches which have shown the FC to evolve over few seconds. Similar to the static (i.e. time-averaged) resting state FC assessments, the ultimate objective of the time-varying resting state FC studies is to understand the driving mechanisms and cognitive implications of the observed fluctuations in FC of the brain regions. Studies (Chang, Liu et al. 2013, Tagliazucchi and Laufs 2014, Allen, Damaraju et al. 2017) have reported identification of potential electrophysiological correlates of fluctuations in BOLD FC thus suggesting the neurophysiological origin of FC and linkage to cognitive as well as vigilance states of the brain. Increasingly, information in the temporal variability of the correlation structure between RSNs is being leveraged to identify group differences between the diseased and healthy controls (Damaraju, Allen et al. 2014, Rashid, Damaraju et al. 2014, Miller, Yaesoubi et al. 2016). The most commonly used time-varying FC approaches including the ones used in this dissertation are discussed in the next sub-section.

2.4.2 Time-Varying FC Approaches

Analysis of the temporal dynamics of network time-courses, also referred to as time-varying FC, is generally carried out by applying a sliding window correlation (SWC), dynamic conditional correlation (DCC), phase synchronization (PS), co-activation patterns (CAPs) or a time-frequency coherence (TFC) approach.

The SWC method (Sakoglu, Pearlson et al. 2010, Allen, Damaraju et al. 2012) evaluates temporal FC by calculating the correlation between the time-courses of the

components of interest at all time-points within a chosen window, and repeating the process by gradually moving the window through the scan length. This generates a series of time-indexed windowed whole-brain correlation or covariance (FC) estimates. Recently introduced to the neuroimaging community, the DCC method (Lindquist, Xu et al. 2014, Choe, Nebel et al. 2017) is a multivariate volatility model that estimates model parameters through quasi-maximum likelihood methods and is widely used in the finance literature to estimate time-varying variances and correlations. The PS method (Glerean, Salmi et al. 2012) involves comparison of two signals by separating the amplitude and phase information parts, and has been reported to have maximal temporal resolution; however, its use is limited to narrow band signals. The focus of the CAPs method (Liu, Chang et al. 2013, Liu and Duyn 2013) is to identify and study instantaneously co-activating patterns. Lastly, the TFC approach is an extension of the coherence and time-domain approaches that features connectivity pattern estimation using the frequency and phase lag information, and has been successfully used in studying connectivity in a few brain regions of interest (Chang and Glover 2010) or whole-brain connectivity (Yaesoubi, Allen et al. 2015). In this work, we will focus on using the sliding window method as it applies minimal assumptions to estimate the windowed correlations and few data transformations.

2.4.3 Time-Varying FNC State Profiles

FC analysis using sliding window is often proceeded by a rigorous whole-brain FC "state" profile estimation and characterization process (originally proposed in Allen, Damaraju et al. (2012)) that identifies the frequency and structure of the estimated windowed correlations. Herein, the FC states are referred to the distinct discrete, transient patterns of FC, conceptually analogous to the quasi-stable EEG microstates. The estimated

state profiles represent transient patterns of functional connectivity that vary over time; it was found in Allen, Damaraju et al. (2012) that subjects tend to remain in the same state profile for long periods of time before transitioning to one of the other state profiles (after multiple TRs).
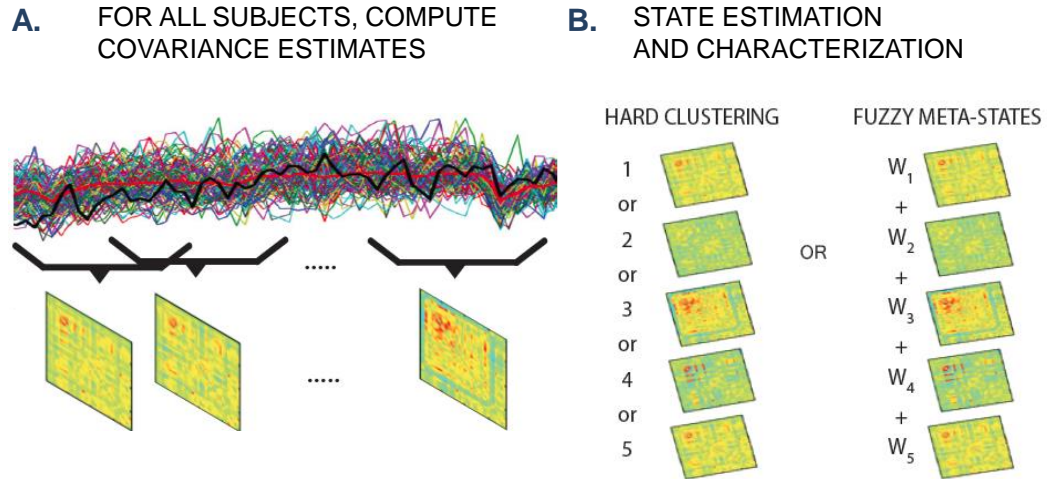
Figure 2-5: (A). For all subjects, covariance estimates are estimated using the SWC approach. (B). The frequency and structure of this windowed data (for all subjects) is assessed through a state estimation and characterization procedure using multiple approaches including, but not limited to, the hard clustering and fuzzy meta-state approaches. The hard-clustering approach assigns membership of each of the observed high dimensional samples (i.e. windowed correlation/covariance matrices) onto one of the clusters, whereas the meta-state approach allows a more flexible, fuzzy membership where each of these observations is expressed as a weighted sum of the identified group-level FC state profiles.

This hard-clustering approach (Allen, Damaraju et al. 2012) maps the high-dimensional windowed correlation patterns to one dimension i.e. they are allocated membership of one of the clusters. With existence of hard defined boundaries, distant windowed FC patterns may still be assigned the same centroid, whereas lesser dynamically different windowed FC patterns may be assigned two different clusters. Such an approach is complemented by a more flexible, fuzzy framework of expressing connectivity in the

state estimation and characterization process (Miller, Yaesoubi et al. 2016) . This second

approach is based on a meta-state framework proposed recently to allow a subject's state

to be represented by varying degrees of multiple states and is claimed to exhibit lesser

distortion in the windowed FC patterns and other features under investigation since

contributions of all overlapping states are recorded. In this work, we evaluate time-varying

FC state profiles as estimated by two frameworks - (1) the hard-clustering approach (Allen,

Damaraju et al. 2012), and (2) the fuzzy meta-state approach (Miller, Yaesoubi et al. 2016),

details of which are covered in the methods section of Chapter 3.
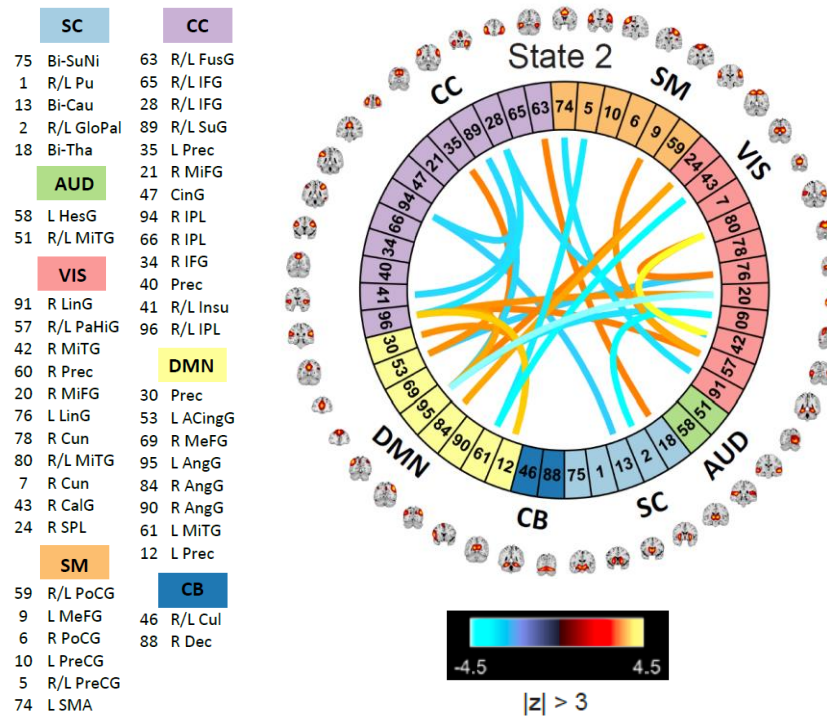
Figure 2-6: An example of a whole-brain FC state profile connectogram.

For ease of interpretation, the whole-brain FC connectivity patterns are commonly

represented in the form of matrices (as in Figure 2-5) where each element of the matrix

represents the FC strength in that brain connection (i.e. pair of brain regions). To avoid

redundancy due to symmetry, the "connectograms" (Figure 2-6) represent yet another favorable way to visualize the whole-brain FC patterns.

2.5 Multimodal Fusion

Different brain imaging modalities enable unique, filtered and complimentary insights of brain's activity and organization, thus intrinsically accomplishing a more comprehensive view (Calhoun, Adali et al. 2006, Calhoun and Adali 2009, Schultz, Fusar-Poli et al. 2012, Sui, Yu et al. 2012, Uludag and Roebroeck 2014, Calhoun and Sui 2016). Given the above benefits, multimodal neuroimaging data acquisition and analysis has become much more widely utilized in recent years. The multimodal data could be analyzed through separate or collective pipelines using a variety of univariate or multivariate algorithm through a model-based or data-driven approach (Calhoun and Sui 2016) as highlighted in Figure 2-7.

Previous multimodal work has typically analyzed data from different modalities separately and correlated the independent results from the unimodal analyses or used one of the modalities to constrain models corresponding to the other modality. The above mentioned types of multimodal studies have proven to be very useful, but make minimal or limited use of the cross-modality (i.e. joint) information, a resource that is now being increasingly availed by use of "symmetric" data fusion approaches (Calhoun and Sui 2016). "Feature-based" symmetric data fusion approaches inherently first estimate useful features from the different modalities independently and then evaluate relationships between these features, a practice that leverages the partial information available in each of the modalities to reveal data variations not exhibited through the independent analyses.

To date, there have been several interesting demonstrations of the potential of utilizing such cross-modality or joint information in understanding the human brain and its disorders, disease characterization or biomarker identification, and uncovering disrupted links in complex mental illness (reviewed in Calhoun and Sui (2016)).

Notably, multimodal studies with advanced modelling methods assume greater significance in diagnosis of a complex syndrome, for example schizophrenia, where striking pathological and etiological heterogeneity has been observed. Several previous studies (Olesen, Nagy et al. 2003, Bassett, Bullmore et al. 2008, Hagmann, Cammoun et al. 2008, Rykhlevskaia, Gratton et al. 2008, Honey, Sporns et al. 2009, van den Heuvel, Mandl et al. 2009, Camara, Rodriguez-Fornells et al. 2010, Michael, Baum et al. 2010, Skudlarski, Jagannathan et al. 2010, Yu, Sui et al. 2011, Segall, Allen et al. 2012, Alexander-Bloch, Giedd et al. 2013) clearly suggest interactions between structural and FC, and so it is reasonable to hypothesize covariation between "feature spaces" i.e. distilled (or lower dimensional or second/higher order) measures of brain structure and function in each modality. Importantly, reducing or projecting the very high dimensional data to feature spaces facilitates removal of redundant data while promoting identification of inter-modality relationships in a simpler, lower-dimensional space. Hence, in symmetric fusion approaches, it is the lower dimensional feature spaces that are fused to extract joint information some examples of which include contrast maps, amplitude of low frequency fluctuation maps (ALFF), etc. for fMRI data, segmented gray or white matter maps for sMRI data, fractional anisotropy (FA) or mean diffusivity (MD) maps for diffusion tensor imaging (DTI) data, SNP or methylation data for genetic data, etc.
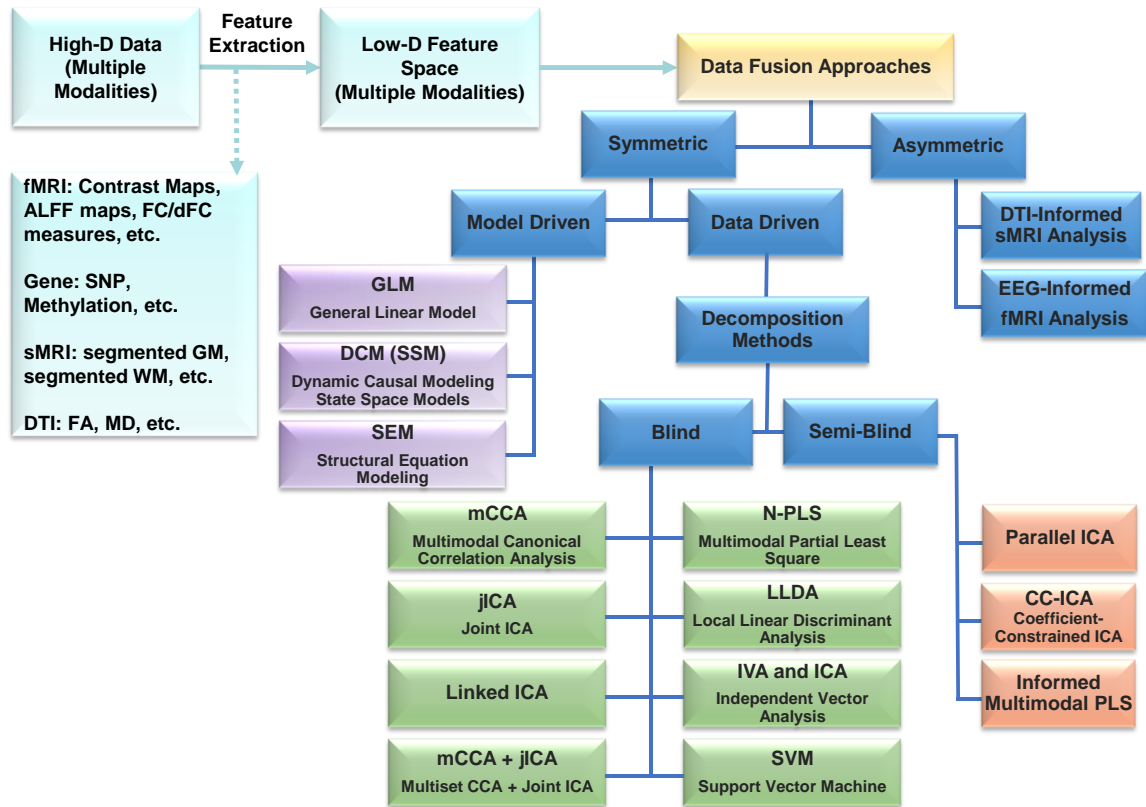
Figure 2-7: Multimodal Data Fusion Approaches. The relatively low-dimensional features extracted from the high dimensional multimodal data are fused including a range of symmetric or asymmetric data fusion approaches as illustrated in this figure. This figure has been modified adapted from Calhoun and Sui (2016).

While model-driven approaches have their own benefits in the form of enabling specific hypothesis testing of inter-regional interaction (provided there is enough prior information available on the problem being studied), data-driven approaches, in general, require specification of lesser assumptions about the data upfront thus making them more suitable for studying complex problems, for instance a complex syndrome such as schizophrenia, wherein little reliable prior knowledge is available. Data-driven approaches typically explore use of a blind or semi-blind multivariate approach to reveal hidden structure of inter-relationships between two (or more) data feature spaces. The use of

multivariate approaches enables estimation of multiple variables jointly and has some additional advantages over the use of univariate approaches. Multivariate approaches are relatively easy to interpret due to co-varying nature of the variables (i.e. regions of interest) and warrant additional robustness to noise as measures from patterns are explored rather than measures from paired relationships (Calhoun and Sui 2016). Recently used blind multivariate decomposition methods include, but are not limited to, joint independent component analysis (jICA) (Calhoun, Adali et al. 2006), multiset canonical correlation analysis (mCCA) (Correa, Adalı et al. 2007), partial least squares (PLS) (Martinez-Montes, Valdes-Sosa et al. 2004, Chen, Reiman et al. 2009), and linked ICA (Groves, Beckmann et al. 2011), while adaptive (semi-blind) approaches such as coefficient constrained ICA (CC-ICA) (Sui, Adali et al. 2009) and parallel ICA (Liu, Pearlson et al. 2009) also exist.

The above discussed multivariate approaches are all based on linear mixture models but differ considerably in the optimization strategies/priorities they evolve the data sources through as well as in their basic limitations. Additionally, combing multiple multivariate algorithms has also been recently suggested to allow flexibility in the estimations by reducing the limiting effects of the individual approaches (Sui, Pearlson et al. 2011) as discussed next. The joint sources estimated by the jICA (or the linked ICA) algorithm are optimally maximally independent but share a common mixing matrix, thus assuming a very strong correlation between the joint sources. Contrarily, the mCCA algorithm jointly maximizes the inter-subject covariations thus allowing for varying levels of connectivity strengths between the joint sources. In this method, each dataset is decomposed into a set of sources with corresponding mixing profiles, also termed as canonical variates (CVs), and their corresponding correlation values, also called canonical correlation coefficients

(CCCs). Despite allowing for varying activation levels of the joint sources, there remains the possibility that the spatial maps of the emergent joint sources in mCCA are highly similar in some cases where, for example, the CCC estimates are not sufficiently distinct (Correa, Adali et al. 2010, Sui, Adali et al. 2012, Sui, He et al. 2013). Sui, Pearlson et al. (2011) used the mCCA+jICA algorithm for fusing the fMRI contrast maps and DTI FA maps to investigate group differences in healthy controls, schizophrenia patients and bipolar patients, and concluded increased group classification accuracy with this algorithm as compared to its constituent algorithms tested alone. This model basically uses mCCA in the first step (Sui, Pearlson et al. 2011, Sui, He et al. 2013) wherein the different feature spaces are first linked with flexible linkages, thus adding to the investigator's confidence to perform joint ICA with an objective of identifying both highly and weakly correlated joint sources in the second step. Additionally, a recent paper has proposed a unifying framework to link together a wide variety of multimodal approaches including the ones mentioned above (Silva, Plis et al. 2016).

2.6 Disease Characterization Data and Methods

In Chapter 5, we characterize the complex brain syndrome of schizophrenia. Schizophrenia is a chronic mental disorder that affects how a person thinks, feels and behaves due to breakdown in relation between thought, emotion and behavior. To characterize schizophrenia, we compare a group of patients diagnosed with this disorder against an age and gender matched group of healthy controls from the fBIRN data repository (Keator, van Erp et al. 2016). To identify the complex inter-relationships as well as disrupted structure-function links in the brain, we pursue a multimodal data fusion approach. In this multimodal work, we use gray matter (GM) measures from sMRI data

and time-varying FC state profiles as measures from fMRI data as features for multimodal data fusion. We fuse these features using a data-driven, blind source separation approach of multiset canonical correlation analysis (mCCA) followed by joint ICA (jICA), also referred to as mCCA+jiCA in the previous literature.

2.7 Disease Progression Data and Methods

In Chapter 6, we predict the progression of patients with mild cognitive impairments (MCI) to Alzheimer's disease (AD). MCI features cognitive impairments that do not significantly impact fundamental functioning (instrumental activities) of daily living, while AD is a degenerative disease with irreversible structural deterioration in the brain leading to cognitive and behavioral disorders in normal functioning of the patients. Notably, MCI can progress to some form of dementia (not necessarily AD); however, in absence of a narrower prodrome for AD, MCI is often used as a prodromal stage of AD. Identifying patients who would likely progress to AD in near future early is highly important not only for improving the patient's health, but also for pharmaceutical companies to test effectiveness of their expensive drugs on the most relevant subjects.

To study progression of MCI to AD, we use the Alzheimer's disease neuroimaging initiative (ADNI) dataset (ADNI). The subset of subjects diagnosed as MCI at baseline time-points in this longitudinal study and who progressed to AD within the follow-up period of three years could be further stratified into the progressive MCI (pMCI) group, whereas the remaining MCI subjects (who did not progress to AD in the follow-up time of three years) could be assigned the stable MCI (sMCI) group. This implies that AD

progression could be (loosely, i.e. in a non-strict sense) understood as a series of transitions most likely to occur in the following specific order: CN-sMCI-pMCI-AD.

In this specific multimodal work in the dissertation, we use gray matter measures from sMRI data and time-varying FC state profiles-based summary measures from fMRI data as features for multimodal data fusion. The features are fused using canonical correlation analysis (CCA) and a linear support vector machine is used to classify sMCI and pMCI groups to quantify prediction of the progression of MCI to AD.

Chapter 3: Framework to Evaluate Replicability of Time-Varying Functional Connectivity State Profiles

3.1 Motivation

Recent studies on assessment of temporal variation in FC in the human brain have made use of time-varying FC approaches to characterize pathophysiology i.e. identification of disease states, thus corroborating the utility of the undertaken approaches (Damaraju, Allen et al. 2014, Rashid, Damaraju et al. 2014, Yu, Erhardt et al. 2015, Du, Pearlson et al. 2016, Miller, Yaesoubi et al. 2016). These studies found extensive additional information through use of these dynamic approaches as compared to that from static assessment of FC, hence advocating the use of dynamic analyses for better understanding of functional connectivity patterns in the brain. Furthermore, the estimated time-varying FC measures have been reported to relate to demographic characterization (Hutchison and Morton 2015, Yaesoubi, Miller et al. 2015, Preti, Bolton et al. 2016), consciousness levels (Hutchison, Womelsdorf et al. 2013, Amico, Gomez et al. 2014, Hudson, Calderon et al. 2014, Barttfeld, Uhrig et al. 2015, Yaesoubi, Allen et al. 2015, Wang, Ong et al. 2016) and cognition (Kucyi and Davis 2014, Schaefer, Margulies et al. 2014, Yang, Craddock et al. 2014, Madhyastha, Askren et al. 2015).

Despite fundamental evidence of availability of considerable, interesting spatiotemporal dynamic connectivity information through these time-varying FC approaches, no prior study has yet evaluated the canonical utility of the time-varying FC measures; in other words, are there certain connectivity patterns that tend to recur across different subjects, i.e. a chronnectome. The need to examine the reliability of the emergent

discrete FC patterns has indeed been mentioned in several leading reviews on this emerging field (Hutchison, Womelsdorf et al. 2013, Calhoun, Miller et al. 2014, Calhoun and Adali 2016). In this chapter, we resolve this previously unaddressed issue by examining robustness (i.e. replicability or reproducibility) in time-varying FC patterns as estimated by two frameworks that used (1) the hard-clustering approach (Allen, Damaraju et al. 2012), and (2) the fuzzy meta-state approach (Miller, Yaesoubi et al. 2016) respectively as we discuss in the coming sections.

3.2 Materials and Methods

3.2.1 fMRI Data Acquisition and Preprocessing

This study worked with resting state data that was previously collected, anonymized, and had informed consent received from subjects, both healthy and patients (aged between 13 to 75 years), as per the institutional guidelines practiced at the University of New Mexico (UNM) and the University of Colorado Boulder (UC, Boulder).

7500 resting state scans were used for this analysis all of which were acquired using 3-Tesla Siemens TIM Trio MRI scanners with 12 channel radio frequency coils at the Mind Research Network (MRN) in association with UNM, or using the same hardware scanner at UC, Boulder. Both scanners used the exact same acquisition parameters (except for the repetition time) for most of the subjects. T2*-weighted functional images were acquired using a gradient-echo EPI sequence with TE = 29 ms, TR = 2s (6992 scans) or 1.3s (8 scans), flip angle = 75°, slice thickness = 3.5 mm, slice gap = 1.05 mm, field of view = 240 mm, matrix size = 64 × 64, voxel size = 3.75 mm × 3.75 mm × 4.55 mm. The sampling rates of the scans were matched before the dFNC analysis. The scans had variable length

with the minimum scan length being 150 TRs; however, only the first 150 time-points of all scans were studied. This data was a de-identified convenience dataset for which we do not have access to the health and identifier information. While it would be useful to have that information and evaluate possible subgroups and additional variables of interest, our perspective was that having this additional variability should, if anything, make the possibility of replicating the state patterns even less likely.

The functional data were preprocessed using MRN's automated preprocessing pipeline based on the SPM software. The data pre-processing pipeline integrated removal of the first three images in the scans to avert T1 equilibration effects, realignment using INRIalign, timing correction of slices with the middle slice fixed as reference, spatial normalization of data into the Montreal Neurological Institute (MNI) space, re-slicing of data into cubic voxels of side 3mm, and data smoothing using a Gaussian Kernel with the full-width at half- maximum (FWHM) set to 10 mm.

Anomaly detection in the form of a correlation analysis on the five upper and lower slices of the functional images was performed on all 7500 scans to detect scans that failed the reorientation process or had any missing slices. This outlier detection removed 396 subjects, thus leaving behind a total number of 7104 subjects corresponding to approximately 95% of the available data.

3.2.2 Spatial Group ICA and Postprocessing

The built-in auto-masking function in the AFNI software was leveraged to create an average mask to be used as the template mask input while running group ICA on the data that passed the anomaly detection analysis. In a multistep procedure to identify the

RSNs, data was decomposed into maximally spatially independent components using functions from the Group ICA of fMRI Toolbox (GIFT). With a higher model of 100 (aiming at finer parcellation), this group decomposition used only the initial 150 time-points of all scans.

Choosing a higher number of principal components at the subject level stabilizes back-reconstruction and retains maximum variance in the data as shown in (Erhardt, Rachakonda et al. 2011). So, in the group ICA analysis, the entire dataset was transformed into 130 principal components using standard principal component analysis (PCA) at the subject level in the first data reduction step retaining maximum subject-level variance (greater than 99.99%), and further down to 100 components by implementing group level PCA in the second data reduction step. ICASSO (Himberg, Hyvarinen et al. 2004) was used to investigate reliability of the estimated independent components, and it was found that the estimates exhibited tight clustering, hence converging consistently amongst several runs. The spatial maps and time-courses of the individual subjects did not undergo backward reconstruction since it was not required for this specific analysis. Careful analysis on the emergent decomposition patterns confirmed 61 components having no correspondence to any known imaging, physiological, movement-related artifacts. Component map templates for these shortlisted components were assessed and distributed into the somatomotor, parietal, frontal, default mode, visual, temporal and cerebellar networks (Figure 3-1).

To set up the maximum possible number of independent samples each having a large partition size, the first 7000 of the 7104 scans were partitioned into 28 age matched groups each having 250 scans. These age-matched groups were a mix of subjects from both

sites (UNM: a total of 6472 subjects, with 231.1 +- 4.3 subjects per group, all subjects with a TR of 2 seconds; UC: a total of 528 subjects with 18.9 +- 4.2 subjects per group, 520 subjects with a TR of 2 seconds), and had an average age of 31.65 years with an average standard deviation of 13.8 years for subjects within the groups.

With a focus on evaluating repeatability of the dFNC metrics corresponding to the partitioned samples, all the samples underwent separate group ICA decompositions. Like the entire dataset group ICA decomposition, standard PCA was performed at subject level for reducing data down to 130 components in the first step, and further down to 100 components by using group level PCA in the second step. Again, alike the entire dataset decomposition, ICASSO (Himberg, Hyvarinen et al. 2004) was used to verify consistency of the estimated independent components in all 28 group decompositions. However, subject specific time-courses and spatial maps were also back reconstructed for these group decompositions since they were required for the inter-component correlation (i.e. FC) analysis.

The reconstructed component time-courses went through additional processing steps to remove any residual noise sources mostly including low frequency trends originating from the scanner drift, motion related variance emerging from spatial non-stationarity caused by movement, and other non-specific noise artifacts unsatisfactorily decomposed by the implemented linear mixed model. More specifically, the post-processing steps featured de-trending existing linear, quadratic and cubic trends, multiple linear regression of all realignment parameters together with their temporal derivatives, outlier detection using 3D spike removal, and low pass filtering with high-frequency cut-off being set to 0.15 Hz. Lastly, the time-courses were variance normalized which meant

the covariance structures from the sliding window approach were equivalent to the correlation structures.

3.2.3 Resting State Network Selection

An extensive evaluation of the spatial maps and spectral composition of the components resulting from the entire dataset gICA decomposition was carried on identifying physiological non-artifactual, previously established networks. Specifically, 61 template components with local peak activations in gray matter, time-courses dominated by low-frequency fluctuations, and high spatial overlap with known RSNs were selected for further analysis. For each of the 28 group decompositions, respective components were mapped to the identified 61 non-artifact template components from the entire dataset decomposition by finding best unique matches through a greedy correlation analysis. The 37 components with highest correlation values or more specifically above the first quartile correlation threshold value of 0.65 and global correlation threshold value of 0.4 for all sample decompositions were retained for the dynamic FNC analysis.

3.2.4 FC Estimation and Temporal Variability

Dynamic FNCs between all $^{37}_2C$ (666) RSN pairs in each of the twenty-eight group decompositions were estimated using a tapered sliding window featuring convolution of a rectangular window (width = 30 TRs = 60 seconds) with a Gaussian (σ = 3 TRs), and subsequently sliding this tapered window in gradual steps of 1 TR, finally resulting in as many as W = 120 windows. Hence, for each group, dFNC was estimated subject wise to get a series of correlation vectors corresponding to the series of windowed partitions of the subject specific time-courses.
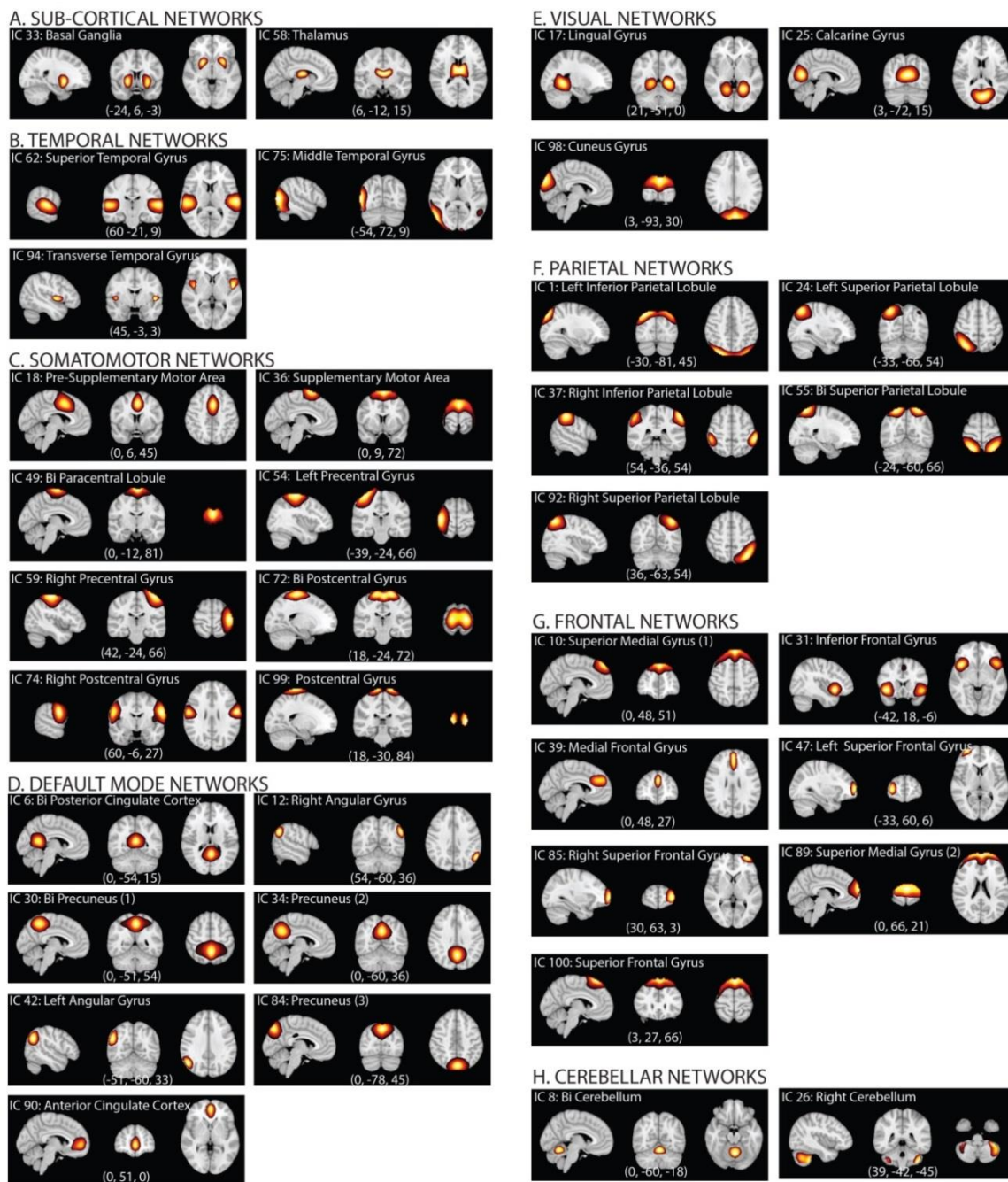
Figure 3-1: Resting State Networks (RSNs). Spatial maps of the thirty-seven retained RSNs at the most activated sagittal, coronal and axial slices.

3.2.4.1 Hard-Clustering Approach

In this approach, the frequency and structure of the reoccurring $^{37}_2C$ (666) dimensional dynamic windowed CPs emerging from all subjects in a specific group was modularized by implementation of the classical hard k-means clustering. The clustering algorithm was implemented using the Manhattan (cityblock) distance as the similarity measure since the L1 norm has been suggested to be a more effectual similarity measure than the L2 norm for high dimensional data.

The elbow criterion was used to derive the number of clusters input to the clustering algorithm. In this method, the central idea is to run k-means for different values of a specified number of clusters (k) and determine the case that maximizes within-cluster similarity and between-cluster dissimilarity concurrently. More specifically, we measured the ratio of within cluster sum of squared distances (dispersion in the cluster) to the sum of squared distances for all other observations (total variability outside that cluster). Finally, we evaluated this measure averaged over all clusters with respect to the number of clusters and validated the case after which the gain in explanation of variation in data made only a marginal difference.

Furthermore, a two-level clustering was implemented to reduce the clustering error where an initial point input to the second level clustering was estimated in the first level clustering, and all windowed FNC data was clustered in the second level clustering. The initial point input was found by estimating and clustering the subject exemplars (corresponding to subject FNC windows featuring highest variance in FNC). More specifically, for each subject time-point (window), the standard deviation in FNC was

computed, and windows at the time-points exhibiting local maxima were retained as subject exemplars and subsequently clustered. The centroid connectivity patterns resultant from this first level clustering were then set as the initial point input to the second level clustering of all FNC data. This two-level clustering process is similar to EEG microstate analysis (Pascual-Marqui, Michel et al. 1995), and was thoroughly tested for consistency for fMRI data in Allen, Damaraju et al. (2012). Repeating the initial as well as final clustering 150 times to increase the likelihood of escaping local minima, stable time-varying FC state profiles (SPs) were obtained for each of the groups.

Connectivity SPs emergent from the group-wise clustering analysis contain information on inter-RSN connectivity strength and variation in a group and can be thought of as states that the subjects repeatedly transit into through the course of the scan. To evaluate replicability of state measures across groups, all sets of SPs were first sorted across groups in a multiple step greedy similarity analysis using Manhattan distance as the similarity measure. In each step, a new group was fixed as a reference to which the remaining groups where evaluated for similarity and then sorted according to the similarity distance thus eventually resulting in 28 sets of sorting orders. In the last step, the statistical mode over this structure of best matches of SPs was validated as the final sorting order. The least frequency of any of the modes was observed to be 22 out of the 28 groups, and similar results were achieved by using other L1 and L2 (Euclidean, squared Euclidean, correlation distance) similarity measures in the clustering algorithm, thus confirming reliability in the sorting process. Summary measures as discussed in the results sections were computed and compared across the sorted SPs in this clustering approach.

Visualizing data is considered important for quality control in any field, and hence we made an attempt to visualize the projections of the high dimensional CPs onto a two dimensional space by using the tSNE algorithm (Maaten and Hinton 2008). In the tSNE projection analysis, Euclidean distance between points is computed, and modelled as conditional probabilities with which one point would pick another as its neighbor such that more similar points are located nearby. Data is preprocessed with PCA reducing dimensionality to an initial number of dimensions at the start of the learning. Perplexity of Gaussian distributions in higher dimensional space can be interpreted as the smoothing measure of number of effective neighbors. In this projection analysis, the initial number of dimensions was set to be 50, initial learning rate as 500, number of iterations as 1000, and the Gaussian perplexity was set to 50.

3.2.4.2 Fuzzy Meta-State Approach

Computation of meta-states involves derivation of the windowed connectivity correlation data in a similar fashion as in the hard-clustering approach. In this approach, the $^{37}_{2}C$ (666) dimensional windowed FNC covariance structures were decomposed into fewer dimensional (o) connectivity patterns (CPs) using one of the commonly used data-driven approaches viz. temporal ICA, spatial ICA, k-means and PCA. The lower dimensional CPs are maximally mutually independent time-courses with overlapping connectivity profiles in case of temporal ICA decomposition, maximally independent spatial patterns in case of spatial ICA decomposition, and orthogonal projections capturing maximal variance for the PCA decomposition. In case of the k-means clustering approach, cluster memberships are assigned to get low within cluster distances and high between cluster distances with the cluster centroids being treated as basis correlation patterns.

The windowed data decomposition was followed by assessment of contributions of the emergent, maximally independent patterns to the actual windowed correlation CPs. Finally, the real-valued weights associated with these states were estimated for every windowed FNC pattern, and the discretized version of this lower dimensional (o = 5 for main discussion, and o = 2 through o = 5 for comparison of results) characterization of the 666-dimensional CPs was achieved with a signed quartile transformation which resulted in meta-states. In our work, we compare results from the different decomposition methods, but mainly focus on the temporal ICA decomposition throughout the meta-state analysis discussion. The overall objective in this approach is again to calculate and compare group wise statistics from the meta-state profiles derived from all time windows of all the subjects in a given group.

3.3 Results

In this section, we first describe results from the feature (or component) selection process following the group level ICA decompositions, and subsequently discuss findings from both dFNC approaches used in this study.

3.3.1 Feature Selection

The spatial maps of the 37 retained RSNs were thresholded (t_c) by using mean (μ_c) and standard deviation (σ_c) parameters estimated using a normal-gamma-gamma (NGG) model ($t_c > \mu_c + 8\sigma_c$) to show regions contributing to the networks (Allen, Erhardt et al. 2011). The thresholded spatial maps of the RSNs at the most activated sagittal, coronal and axial slices are plotted in Figure 3-1. Co-ordinates of peak activations in MNI space, maximum activation level, activation region voxel volume, and associated Brodmann areas

for the retained 37 RSNs are summarized in Appendix A Table 1. It can be easily confirmed

that the retained RSNs demonstrate high similarity to RSNs from previous high-order

decomposition studies (Allen, Erhardt et al. 2011, Allen, Damaraju et al. 2012).

3.3.2 Hard Clustering Approach

3.3.2.1 Optimal Clustering Analysis

The elbow criterion suggested an optimal number of five clusters for all groups

(Figure 3-2A). For all groups and each k, the method was repeated 10 times as a consistency

check. The group-wise boxplots of the validated number of clusters over the different runs

are shown in Figure 3-2B.
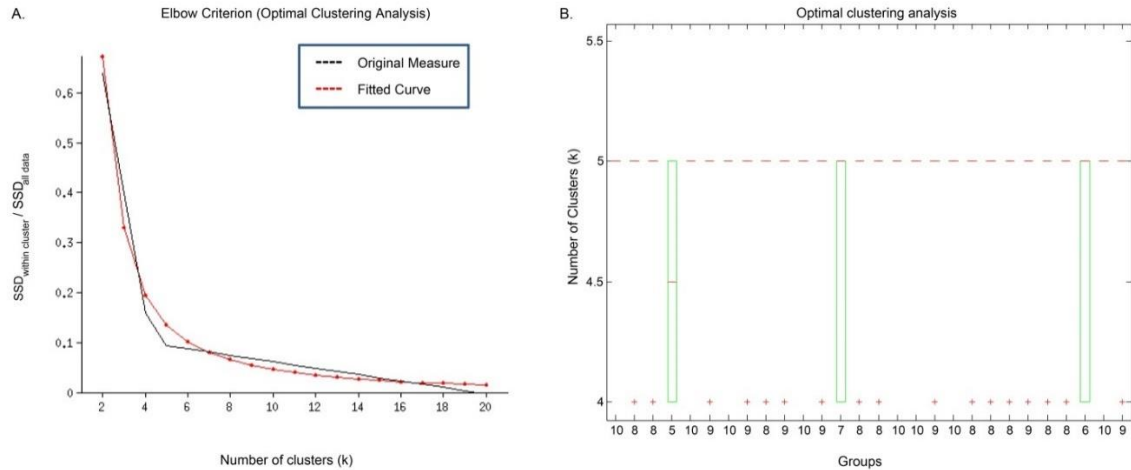
Figure 3-2: Optimal Clustering Analysis. (A) Elbow plot for a sample run; (B). Group-wise boxplots of the estimated optimal number of clusters over 10 independent runs. (B) The x-axis labels in Figure 3B illustrate the number of runs for that group (out of a total of 10 runs) that estimated the optimal value of k equal to 5. In all, 241 out of the 280 independent runs estimated the optimal value of k equal to 5; hence, this value of k was validated as the optimal clustering case for the rest of the study.
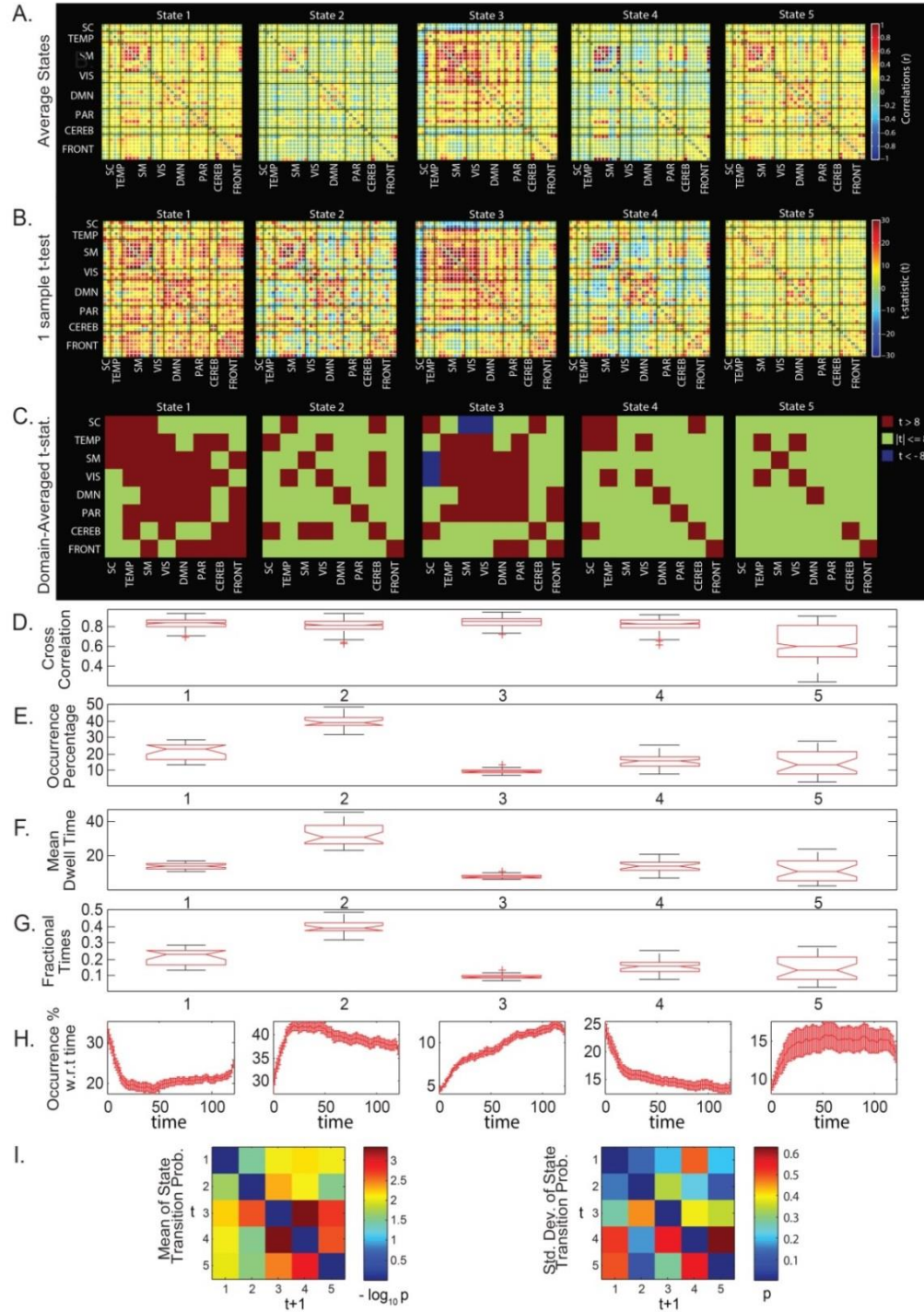
Figure 3-3: State summary measures in the clustering approach. (A) State profiles (SPs) averaged over all groups; (B) 1-sample t-test results on the SPs; (C) 1-sample t-test results averaged over the domains; (D) Boxplots of pairwise linear correlations of the SPs; (E) Boxplots of average occurrence % of the SPs; (F) Boxplots of the average mean dwell times of the SPs; (G) Boxplots of average fractional times of the SPs; (H) Occurrence percentages of the SPs modeled w.r.t. time; and (I) Mean and std. deviation of average state transition probabilities (modelled as a first order Markov chain).

3.3.2.2 State Summary Measures

Characterizing states and summarizing state metrics provides important and useful information e.g. the time spent in a particular state, the directional probability of transitions between two particular states, etc. that help us quantify replicability between the independent group decompositions. The state summary measures and similarity statistics evaluated in the hard-clustering approach are shown in Figure 3-3, and their relevance and contribution in eventually investigating replicability of the temporal dynamics is discussed subsequently.

The average state metric (Figure 3-3A) provides information on averaged connectivity and the percentage of occurrence considering all independent samples as one large sample, whereas the one-sample t-statistic metric (Figure 3-3) highlights regions with high mean and smaller standard deviations, and hence the connections in the region can be considered to be more reliable. The 1-sample t-test statistics averaged over pairs of network domains can be seen in Figure 3-3C to highlight the most reliable network domain pairs in a particular state. Figure 3-3D shows the pairwise linear correlations of the mapped SPs across all the groups. Evidently, states 1 to 4 have high correlation numbers (first quartiles greater than 0.8) suggesting these states are highly reproducible across the independent samples, whereas state 5 with higher spread is not as fully reproducible as the other states. The considerably larger spread of state 5 in the correlation boxplot is explained in the t-distributed Stochastic Neighbor Embedding (tSNE) projection analysis (Maaten and Hinton 2008) in the coming sub-section where state 5 is actually observed as mixture of states 1 and 2.

We also compare the state occurrence percentage, mean dwell time spent in each of the states, and fractional times for each of the states for all groups as shown in the boxplots in Figure 3-3E, 4F and 4G. For each of the boxplots, the group-wise state measures are well concentrated within their respective ranges with state 2 consistently observed as the most frequent (39.5 % average occurrence time), and hence with higher dwell and fractional times.

The number of occurrences of the states is next modeled as a function of time (Figure 3-3H) so as to observe how the state occurrence frequencies increase or decrease with time. Due to the unconstrained nature of resting state, it is unlikely to obtain consistent temporal trends in the cognitive states of the brain. However, we could investigate existence of any consistent temporal trends in occurrence of the FC state profiles to motivate theories on their relation to vigilance, sleep or arousal states. Similar to earlier work (Allen, Damaraju et al. 2012), we observe a state with increased thalamocortical anti-correlation probably related to drowsiness (State 3) for which frequency of occurrence increases with time spent in the scanner and that occurs about 10% of the time in all groups. This observation is consistent with Tagliazucchi and Laufs (2014) who report reliable drifts between wakefulness and sleep during typical waking rest fMRI scans. Furthermore, EEG correlates suggest that this state corresponds to increase in low frequency delta and theta power suggestive of reduced vigilance (Allen, Damaraju et al. 2017).

Finally, state transition behavior is captured by a first order Markov model which helps in understanding the propagation of probability transitions through the network i.e. probabilities associated with entering or exiting a given state. For readability of this model, the average values of probabilities (p) of group-averaged state transitions across all groups

have been transformed through a $-log_{10}p$ transformation. Hence, smaller values in the averaged state transition matrix (on the left in Figure 3-3I) correspond to high probabilities of transition from one state to another. The standard deviations in the averaged state transition matrices across all groups are shown to the right in Figure 3-3I. It can be observed that there is a high probability of being in the same state at the next time instant (high probability along the diagonals), as well as a high reliability of transition to and from state 2 as compared to other states as they tend to have higher mean transition probabilities and smaller standard deviations. However, transition probabilities, with high standard deviations in some cases, can also be highly variable.

3.3.2.3 Visualizing State Profiles

The tSNE algorithm is known to preserve the local structure of the data by projecting similar higher dimensional structures (with smaller pointwise distance) closer in the 2D space than the relatively distinct ones as the algorithm learns at a predefined learning rate while the data is being processed over a predefined number of iterations. In this analysis, we used tSNE to project the exemplar high-dimensional windowed FNC data from all of the 28 groups onto a two-dimensional space.

The final projection of the exemplar data can be visualized in Figure 3-4A which suggests states 1, 2, 3 and 4 to be clustering consistently, whereas state 5 showed high variance and appeared more similar to states 1 and 2. This observation suggests that the 5th state is not fully reproducible as the other states. Figure 3-4B shows the data for states 1 to 4 only (for all groups), and these 4 classes can be seen to be clustered in distinct but touching regions. An assessment of the class conditional density peaks for these states in 2

dimensions (Figure 3-4C) and 3 dimensions (Figure 3-4D) revealed distinct density peaks

for all 4 classes thus further supporting the existence of structure in the clustered data.
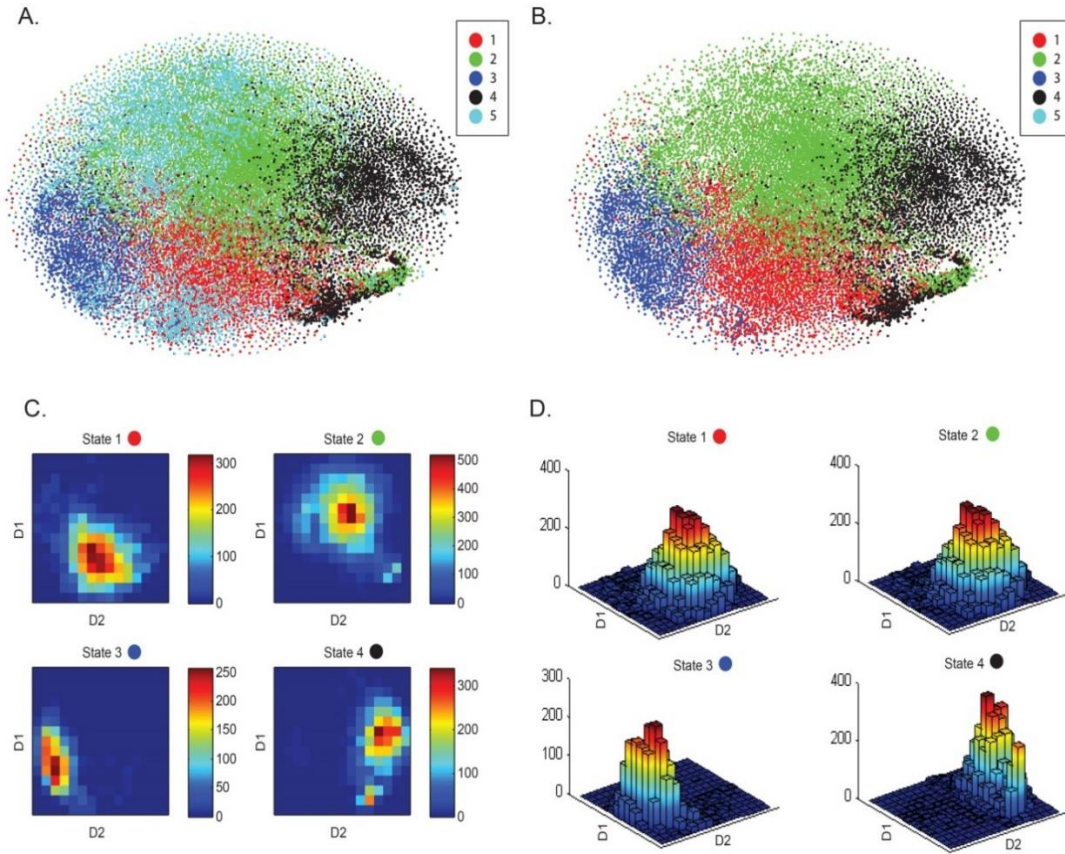
Figure 3-4: High-dimensional windowed FNC data projection onto a two-dimensional space using the t-distributed Stochastic Neighbor Embedding (tSNE) framework. (A) tSNE visualization of the windowed FNC data from all 28 groups suggests consistent clustering for states 1, 2, 3 and 4 for all groups, touching class boundaries and low degree of homogeneity for state 5. Additionally, from the state summary measures, State 5 was seen to be less reproducible as compared to the other 4 states. (B) tSNE visualization for states 1 to 4 for all groups confirms distinct (but touching) clustering regions for these different data classes. (C) and (D) Class conditional densities for the states 1 to 4 in 2 dimensions (Figure 5C) and 3 dimensions (Figure 5D) reveal distinct peaks for all 4 classes thus validating the structure in the data.

3.3.3 Fuzzy Meta-State Approach

3.3.3.1 State Summary Measures

For the fuzzy meta-state approach, to evaluate replicability in the group statistics, several meta-state metrics such as number of distinct meta-states occupied (n), number of switches in meta states (s), longest state span (r: largest L1 distance possible in occupied meta-state vectors) and finally the total distance covered by a subject (d: sum of L1 distances between meta-state vectors covered by a subject) are computed from the emergent meta-states. The group-wise histograms of subject meta-state metrics from the temporal ICA decomposition method as plotted in Figure 3-5A show similar spread and distribution across the groups. Figure 3-5B, the mean stem plots and standard deviation boxplots suggest low variation in the estimated group summary metrics (σ_s = 1.0015, σ_n = 1.0678, σ_r = 0.5373, σ_d = 4.5790).

Similar results from alternative decompositions such as spatial ICA, PCA, and k-means clustering (Figure 3-5C) confirm the low variation observed in temporal ICA decomposition metrics. It must be noted that k-means clustering uses only 4 discrete states (1 to 4), and hence has dis-similar numbers as compared to the other three decompositions with a maximum 8 possible states (-4 to -1, 1 to 4). Nonetheless, meta-state metrics from the k-means decomposition are similar across the different groups showing low variation for the estimated dynamic measures (σ_s = 1.3192, σ_n = 1.0840, σ_r = 0.5033, σ_d = 1.6242).
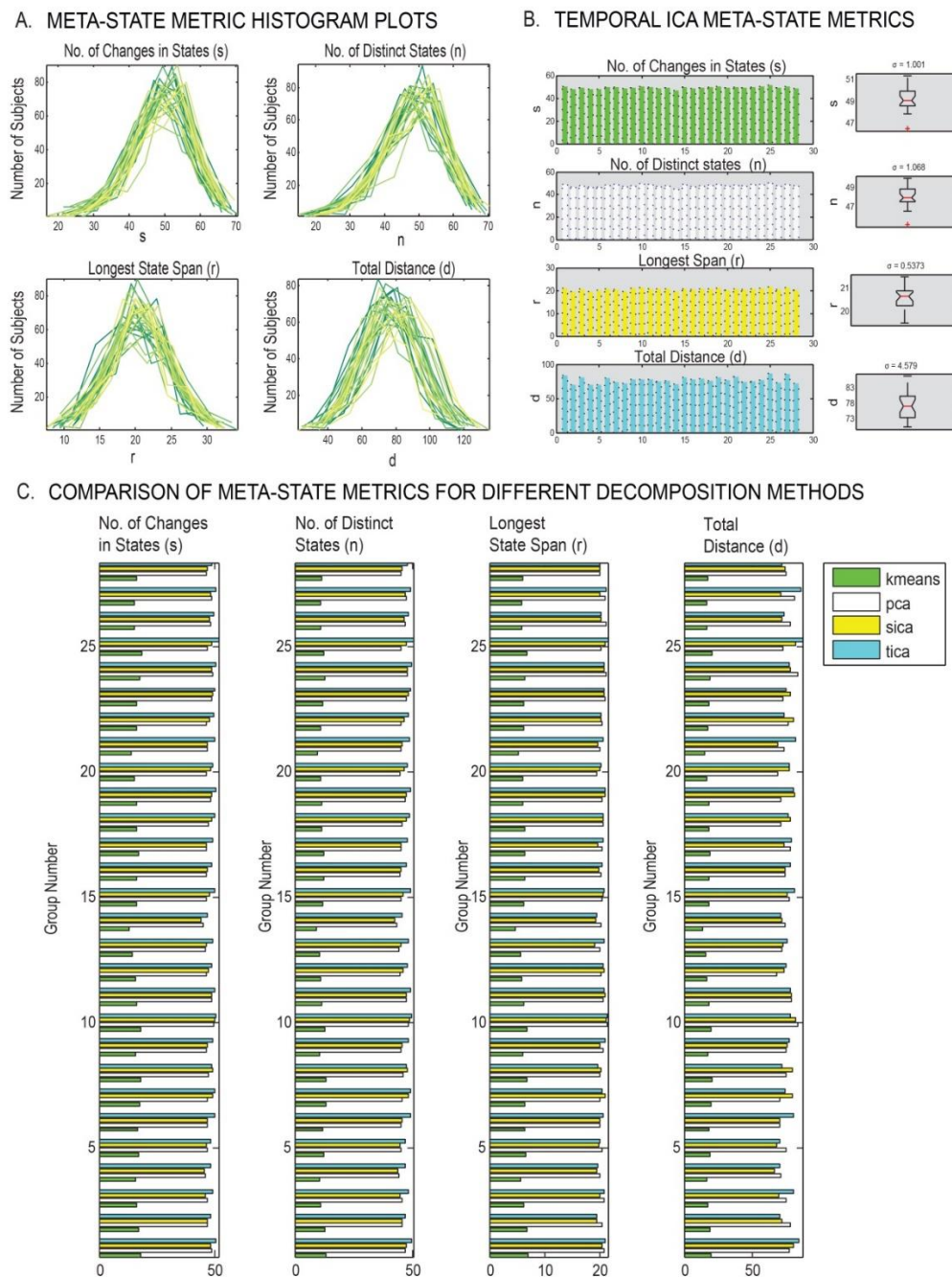
Figure 3-5: State summary measures in the meta-state approach. (A) Histogram plots of the estimated subject-specific temporal ICA meta-state metrics demonstrate similar distributions across all groups; (B) Boxplots of group-wise averages of temporal ICA meta-state metrics indicate low variation in group summary metrics; (C) Similarity of group summary metrics across separate groups within and across different decomposition methods. Notably, the metrics are consistent across groups in k-means, but different from other methods since k-means uses only 4 discrete states (1 to 4), as compared to other methods that use 8 states (-4 to -1 and 1 to 4).

3.4 Discussion

Robustness of time-varying FC profiles and summary measures as evaluated using two previously used chronnectomic frameworks were evaluated over multiple age-matched, large and independent resting state datasets. Current findings from our analyses provide a substantial and novel advancement on the debate of robustness of inferences on temporal dynamics through the undertaken methods.

From group analysis in the hard-clustering approach, we confirmed high correlation in sorted state profiles across the independent decompositions with the first quartiles (25th percentiles) of pairwise correlations greater than 0.8 for 4 out of 5 states. Using tSNE as a quality control measure, we successfully projected the high dimensional state profiles from all independent groups onto a two-dimensional space and could confirm existence of structure in the windowed FC data from all groups and infer results consistent with the metrics derived in this approach. However, this visualization also suggested possible improvements in the chosen clustering algorithm since one of the states appeared as a mixture of two other primary states.

Using the fuzzy meta-state approach as a second pass analysis, we evaluated multiple decomposition methods to explore generic replicability from a distinct perspective. As expected, we found low values of standard deviation for all derived average group-wise meta-state metrics through the temporal ICA decomposition method. This early identification was found to be consistent with similar evidence from replicability analysis using the k-means, spatial ICA and PCA decomposition techniques.

Taken together, results from our analyses provide several lines of evidence of substantial reproducibility in the basic connectivity patterns amidst an ensemble of inter-regional connections. We test the statistical significance of the time-varying FC state profiles and validate our replicability findings through extensive internal and external validation procedures on real and surrogate fMRI datasets in Chapter 4.

Chapter 4: Validation and Statistical Significance Testing of Time-Varying Functional Connectivity State Profiles

This chapter focuses on the validation and statistical significance testing of the estimated time-varying FC state profiles and associated state summary measures respectively.

4.1 Motivation

Delimiting validation, robustness and generalization of the research results through specific preset statistical criterion is an important quality control process in research. We seek these boundaries by conducting rigorous tests for correspondence across different model orders on the real fMRI data (internal validation) and permutation tests are conducted using artificially synthesized surrogate data (external validation) in both the implemented time-varying FC frameworks tested in the previous chapter.

Internal validation i.e. testing correspondence across inferences for a range of model orders in both tested approaches is rather straightforward, and general correspondence in the structure of state profiles and range of meta-state metrics across the range of model orders in both frameworks could be expected. However, external validation i.e. testing for statistical significance of the observed measures (on real fMRI data) through a given framework is not as straightforward. This requires generation of a null distribution of the observed measure in absence of the phenomenon of interest (i.e. windowed correlations and higher order measures based on this metric). The value of the statistical measure of interest estimated from real data is then compared against the null distribution of that measure as generated from surrogate data. As such, a rejection of the null hypothesis

would evince statistical significance of the captured measures, and hence the statistical framework that was used to capture the phenomenon of interest in the first place. On the other hand, a failure to reject the null hypothesis would simply imply lack of evidence that the statistical framework indeed captured the phenomenon of interest. The real problem, however, lies in the generation of "appropriate" surrogate data to estimate a valid and useful null distribution (Miller, Abrol et al. 2018).

To generate null data from surrogate data, undoubtedly, it would be highly useful to replicate the behavior of "noiseless" BOLD data by "appropriate" simulations; however, an absence of a baseline, i.e. ground truth for resting state, makes this very step extremely challenging. Null models must therefore be approximated using the available fMRI data. Previous research has used the phase randomization (PR) and vector auto-regressive (VAR) models for this purpose. These models allow testing for the hypothesis that the observed data is generated by a linear, stationary Gaussian process. In this work, we conduct statistical significance testing through use of the PR model to generate surrogate data. We discuss details of the surrogate data generation and phenomenon of interest we test for both approaches in the methods section, present outcome of the analysis in the results section, and discuss inferences and limitations on these inferences in the discussion section.

4.2 Methods

4.2.1 Surrogate Data Modeling

Statistical significance testing was conducted to verify the driving factor of the emergent discrete FC state profiles (SPs). Surrogate data generation was conducted by

phase randomization (Prichard and Theiler 1994) of the RSN time-courses. Similar to the phase randomization procedure used in few recent fMRI studies (Handwerker, Roopchansingh et al. 2012, Damaraju, Allen et al. 2014, Hindriks, Adhikari et al. 2016), the surrogate RSN time-courses were generated by Fourier transforming the RSN time-courses estimated from real fMRI data, adding a uniformly distributed random phase to each frequency in this frequency domain data, and finally inverse Fourier transforming the frequency domain data back to the time-domain.

Adding the same random phase to the same frequency components of the RSNs preserves the static FNC and the lagged cross-covariance structure in the surrogate datasets. This class of surrogates, hereinafter referred to as "consistent" phase randomized (CPR) surrogates, correspond to the null hypothesis that the real RSN time-courses are explained by a linear, stationary Gaussian process (Schreiber and Schmitz 2000, Borgnat, Flandrin et al. 2010, Richard, Ferrari et al. 2010, Liegeois, Laumann et al. 2017). Alternatively, adding different random phases to the same frequency components of the RSNs disrupts the static FNC and the lagged cross-covariance structure in the surrogates. This alternate class of surrogates, hereinafter referred to as "inconsistent" phase randomized (IPR) surrogates, instead correspond to the null hypothesis that the real RSN time-courses are explained by a linear Gaussian process with static FNC approximately equal to zero (Hindriks, Adhikari et al. 2016).

4.2.2 External Validation: Significance Testing of States and Summary Measures

In the hard-clustering approach, the FC state profiles estimated from CPR and IPR surrogate data were compared to those generated from the original data. In this specific

analysis, the IPR surrogates were used only to seek explanation to clustering as the null generated from this class is not appropriate to make inferences about stationarity of the observed data since lesser than required properties of the observed data are preserved by construction. It must also be noted that by construction of surrogate RSN time-courses, the mean, variance and power spectrum of both surrogate classes are identical to that of the real RSN time-courses, and subsequently using an extension of the Weiner-Khintchine theorem (Prichard and Theiler 1994), both surrogate classes will have the same temporal autocorrelation as the real RSN time-courses. In the second part of this analysis, the observed sum of pair-wise inter-state distances from real fMRI data was tested against the corresponding null distribution from the CPR surrogates datasets to confirm statistical significance of the framework used to capture the state profiles.

Similarly, null distributions for the four different measures estimated in the fuzzy meta-state approach (i.e. number of changes in states, number of distinct states, longest state span, and the total distance between the states) were generated using the CPR surrogate datasets. Following that, the measures of these metrics from real fMRI data were assessed against the generated metric-specific null distributions.

4.3 Results

4.3.1 Hard Clustering Approach

4.3.1.1 Clustering for a Range of Model Orders

With an objective of using the same dataset to internally validate results from the hard-clustering approach, time-varying FC state profiles were estimated for a range of

number of clusters (k = 2 to 10) and compared to each other. Figure 4-1 plots the state profiles over this range for the first group.

It must be noted that within every group, the state connectivity profiles had to be sorted since the order of the centroids or clusters emergent from the k-means algorithm is not unique. After sorting through a greedy algorithm, it can be clearly seen in Figure 4-1 that clustering results for different clustering indices (i.e. model orders 2 to 10) are consistent.
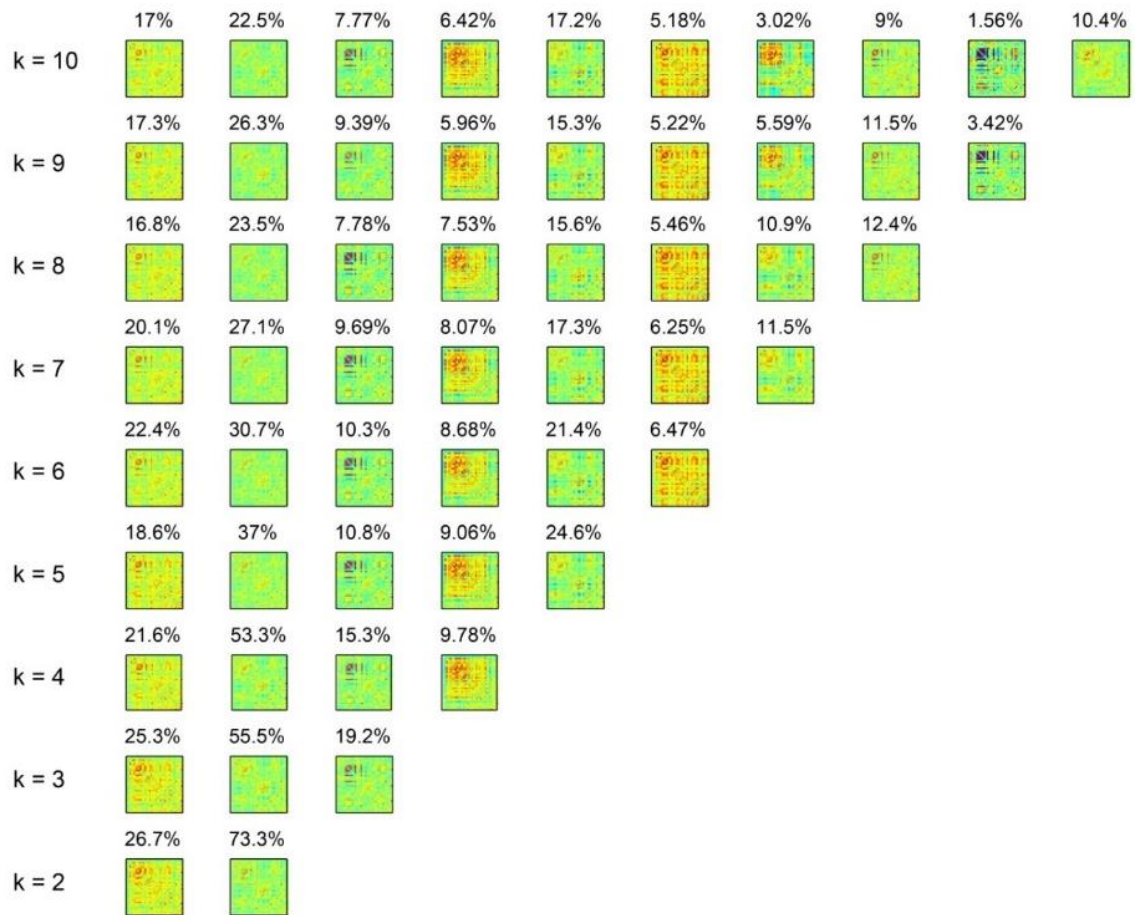
Figure 4-1: Internal validation in the hard-clustering approach. Clustering results for a range of number of clusters (k = 2 to 10) demonstrate high similarity of the emergent state profiles across this tested range of model orders. The occurrence percentage of each state is given in the title of the state image plot.
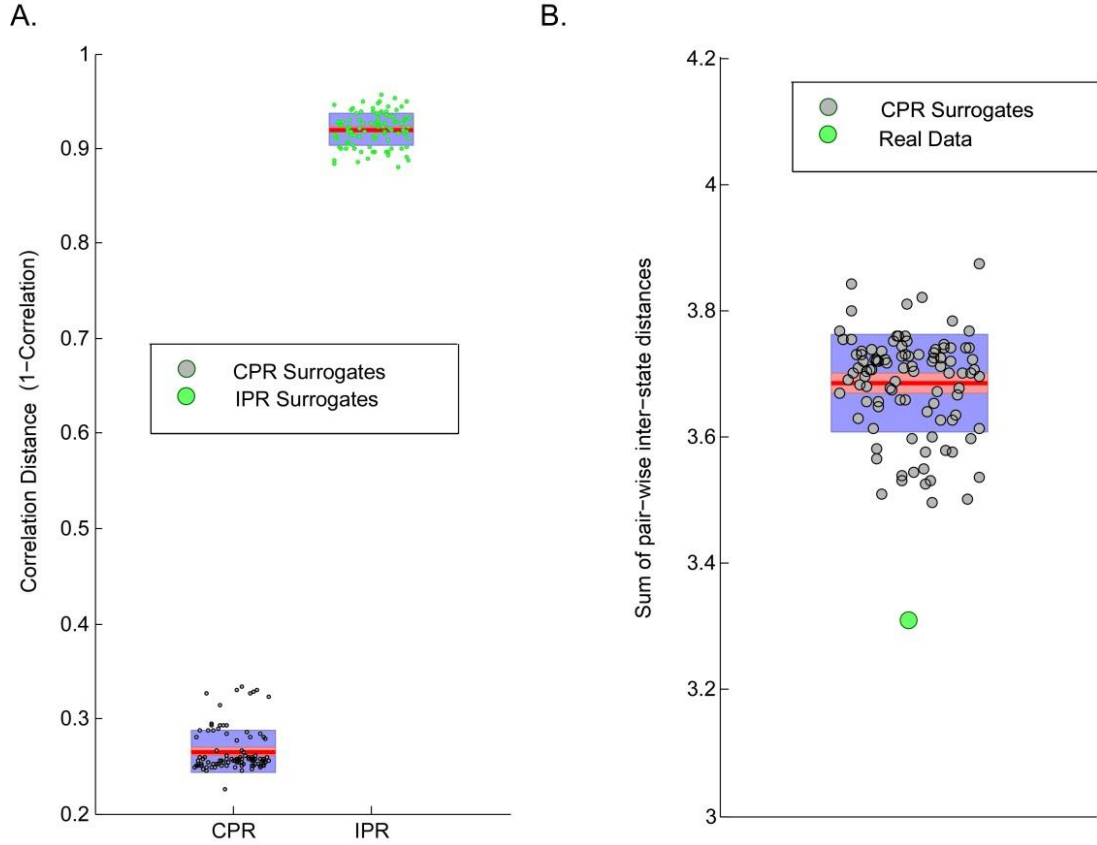
Figure 4-2: External Validation in the hard-clustering approach. (A). SPs emergent from clustering windowed FNC data corresponding to real fMRI data exhibit high correlation with SPs from similar analysis on 100 synthesized surrogate datasets of RSN time-courses with consistent phase randomization (CPR) and low correlation in case of inconsistent phase randomization (IPR); and (B) Observed sum of pair-wise inter-state distances in real data in comparison to the null distribution of this test statistic approximated from 100 CPR surrogate datasets.

4.3.1.2 Clustering Surrogate Data

100 CPR and 100 IPR surrogate datasets for the real RSN time-courses were generated each of which underwent dFNC analysis and subsequent clustering individually. The SPs emergent from the different surrogate datasets were mapped to the SPs in the real fMRI dataset, and finally a scalar correlation distance (averaged across the SPs) was computed for each surrogate dataset. Figure 4-2A illustrates the distributions

corresponding to the two surrogate classes where it can be seen that the CPR surrogates show a very small correlation distance (very high correlation), and the IPR surrogates show very large correlation distance (very low correlation) as compared to the real data SPs. This observation suggests that clustering is substantially driven by the lagged cross-covariance structure of the RSN time-courses and not solely by the linear autocorrelation structure of the RSN time-courses or dissimilarities in mean and variance across subjects.

Additionally, the presence of any significant differences in the statistical measures from the real and CPR surrogate data was explored by approximating the null distribution for a test statistic, namely sum of pair-wise inter-state distances, from the multiple CPR datasets, and subsequently comparing the observed value of this statistic for real data against the generated null (Figure 4-2B). The CPR null was rejected for this test statistic in all groups which suggests presence of non-Gaussianity, non-linearity or non-stationarity, or a combination of these properties in the observed time-courses. Unfortunately, further non-trivial testing is required to narrow down on the cause of the rejection of the CPR null, a topic out of scope of the focus of this study and worth exploring in the future. Nonetheless, the two results in Figure 4-2 jointly suggest that clustering was substantially, but not completely, explained by the lagged cross-covariance structure of the RSN time-courses.

4.3.2 Fuzzy Meta-State Approach

4.3.2.1 Decomposing for a Range of Model Orders

On the other hand, for the fuzzy meta-state approach, sensitivity of the replicability results to the number of dimensions (model order) in the meta-state approach is tested by

performing the meta-state analysis for a range of model orders (o = 2 to 5). Sensitivity of the replicability results to the number of dimensions (model order o) in the meta-state approach is tested by performing the meta-state analysis with this parameter ranging from 2 to 5. As evident from the bar graphs and low standard deviations in Figure 4-3, there is great similarity in all meta-state summary metrics in all model orders, which further substantiates evidence of the replicability of the meta-state approach summary metrics across the independent samples. Notably, the averaged meta-state statistics for the entire dataset increase with the number of dimensions since the range of possible meta-states in the state space increases with the model order; however, within a given model order, high group-wise similarity in the dynamic measures is observed.

4.3.2.2 Decomposing Surrogate Data

Correspondence of the meta-state summary metrics to the RSN time-courses corresponding to real fMRI data was tested by meta-state permutation testing on a set of 100 CPR surrogate datasets of RSN time-courses. For all meta-state metrics, the outcome from the real dataset was determined and compared against the null distribution for the respective meta-state metrics generated from the different surrogate datasets. Figure 4-4 shows that all summary metrics for the real dataset are located completely outside the synthesized null distribution for the temporal ICA, spatial ICA and PCA decomposition methods. Equivalent results were observed for the k-means decomposition method as well. This rejection of the CPR null model for the studied meta-state metrics for different decomposition methods adds further evidence to presence of non-Gaussianity or non-linearity or non-stationarity, or any combination of these three properties in the observed

RSN time-courses. Spotting the specific cause of rejection of the CPR null hereon is non-trivial and an interesting topic for future.
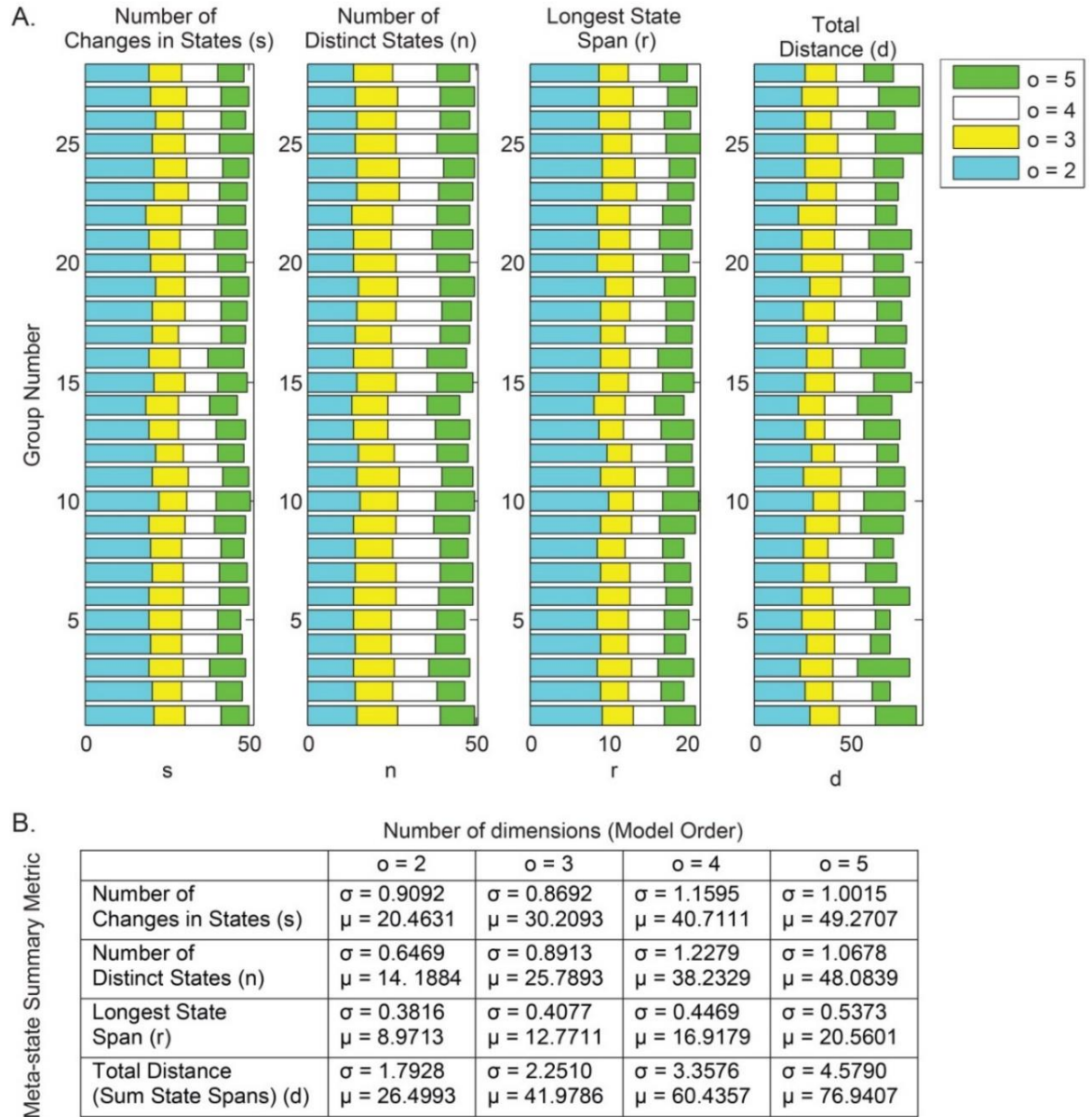
Figure 4-3: Internal Validation in the meta-states approach. (A) Sensitivity test of number of dimensions (o = 2 to 5) to the meta-states framework validates similarity in group summary measures; (B) Averaged metrics are consistent across groups but increase with model order as range of meta-states is proportional to model order.
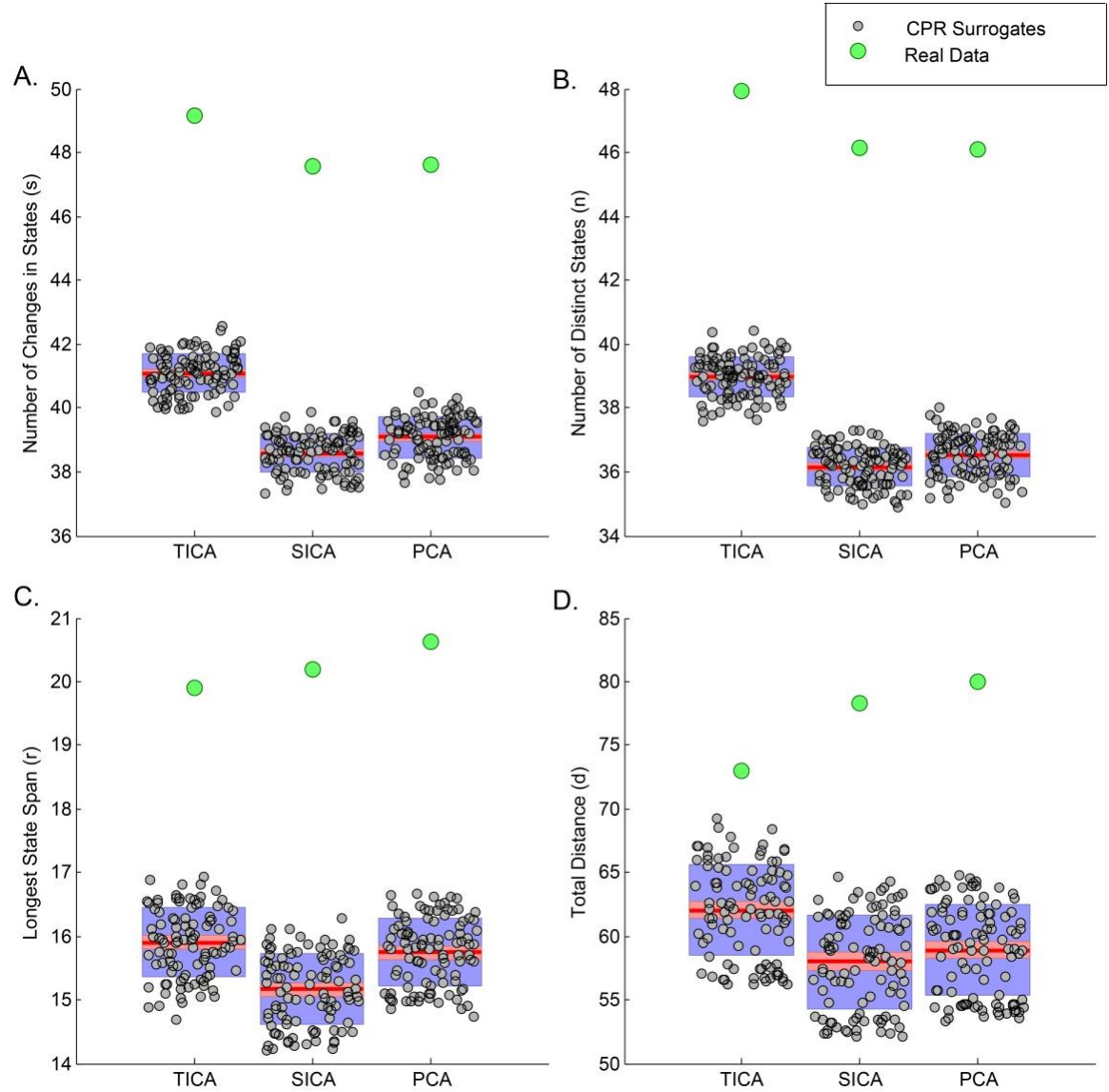
Figure 4-4: External validation in the meta-states approach. Meta-state metrics corresponding to real fMRI data were observed to fall outside the respective null distributions generated from meta-state metrics corresponding to 100 CPR surrogate datasets of RSN time-courses. Results for the temporal ICA, spatial ICA and PCA methods are shown; similar result was observed for k-means method.

4.4 Discussion

Surrogate data analysis for this approach confirmed clustering to be substantially (but not completely) explained by the lagged cross-covariance structure of the RSN time-

courses, while also suggesting the presence of non-linearity or non-stationarity, or both non-linearity and non-stationarity in this observed data. In the fuzzy meta-state approach, validation analysis through permutation testing on the synthesized surrogate datasets confirmed evidence of presence of non-Gaussianty, non-linearity or non-stationarity (or any combination of these properties) in the observed RSN time-courses. In this study, we saw the CPR null model being rejected for one test statistic in the hard-clustering approach and four test statistics in the meta-state approach. Overall, these observations confirm statistical significance of the tested metrics and also suggested that the fMRI data is not fully explained by the linear Gaussian data model.

A major drawback of the used null hypothesis is that it too general, and if rejected, it is not possible to conclude the specific cause of rejection to be non-Gaussianity, non-linearity, non-stationarity or some combination of these properties, and hence there is need for additional analysis. In case of rejection of these null models, it would make sense to test for Gaussianity of the observed data as it is more straightforward, and if the data is concluded to be Gaussian, subsequent advanced statistical testing, for example testing the degrees of non-stationarity and non-linearity, could be explored to further comment on the specific property causing the rejection of the null model. Other recently used alternatives to the CPR and VAR null models include the amplitude-adjusted phase randomization (AAPR) null (Betzel, Fukushima et al. 2016) and the null as used in Laumann, Snyder et al. (2016). The null hypothesis in AAPR model associates to the observed data being a monotonic non-linear transformation of a linear Gaussian process (Theiler, Eubank et al. 1992, Schreiber and Schmitz 2000) and generates data that preserves the amplitude distribution exactly but the power spectrum approximately. Finally, the null used in

Laumann, Snyder et al. (2016) is matched to the covariance structure exactly i.e. preserves the static FC exactly, but to the power spectrum on average i.e. does not preserve the cross-lagged covariance structure exactly as in the CPR and VAR models. Since these different models correspond to different null hypothesis and preserve different properties of the observed data, exploring and utilizing additional knowledge on the nature of the observed data is recommended to appropriately choose the null hypothesis in a given study. In nutshell, there is need for additional work in the field of null model development for statistical validation by surrogate testing, and hopefully more specific null models and/or frameworks to test existing null models in literature will emerge and eventually allow for more specific inferences.

Besides, some innovative ways of using null data to draw conclusions about time-varying nature and consistency of the FC fluctuations have also been recently explored (Zalesky, Fornito et al. 2014, Betzel, Fukushima et al. 2016, Hindriks, Adhikari et al. 2016). Zalesky, Fornito et al. (2014) used a novel framework to provide evidence of a consistent set of "dynamic" inter-RSN connections that exhibited pronounced fluctuations in strength over time. This framework records a non-linear "excursion" test statistic quantifying the extent of time-varying fluctuations in the windowed FNC data for both original data as well as a set of VAR surrogate datasets. In the next step, connections that reject the null distributions of this test statistic are retained for further analysis wherein binary graphs are constructed for each subject using only the top-few most "dynamic" connections and degree of each region in these binary graphs is evaluated. Finally, this degree is summed across the subjects to frame an "index of consistency" of these dynamic connections (i.e. how consistently the regions were dynamic across the subjects). Next,

Hindriks, Adhikari et al. (2016) reported absence of evidence for dFNC in real fMRI data for individual sessions and concluded that using the CPR null model it is difficult to distinguish two test statistics, namely the standard deviation of the windowed data and the non-linear test statistic as originally explored in Zalesky, Fornito et al. (2014). Our analysis with the CPR surrogate datasets generated from fMRI data used in our study suggests the presence of significant "dynamic" inter-regional connections which we also evaluated for consistency through the "index of consistency" metric for both the standard deviation of windowed FNC data and the excursion test statistics (Appendix A - Figure 1). Evaluating consistency of these significantly "dynamic" inter-regional connections across numerous independent samples similar to this study is definitely an interesting work for future.

Recently, Laumann, Snyder et al. (2016) suggested stability of the FC structure observed in resting state BOLD fMRI data over tens of seconds. The authors clearly mention in their work that this demonstrated stability of the FC structure, computed by integrating over time, did not cross paths with time-varying studies analyzing shorter time-scales. Furthermore, recent collaborative work from the same authors has formally demonstrated that even statistically stationary data does not imply absence of brain states (Liegeois, Laumann et al. 2017). The authors also suggested the emergence of the observed states mostly due to sampling variability and physiological confounds in the fMRI data. Our perspective on sampling variability is that such variability (between subjects) is certainly possible but does not by itself argue for or against the presence of dynamic states any more than sampling variability visible in an analysis of GLM maps enables us to detect the presence of the widely studied resting networks in second level task-based fMRI data (Smith, Fox et al. 2009, Allen and Calhoun 2012) argues against the presence of resting

fMRI networks. In addition, there does appear to be agreement that the FC fluctuations in the data 'indistinguishable' from statistically stationary null data could demonstrate behavioral relevance (Shine and Poldrack) and electrophysiological correlates as discussed in the concluding paragraph.

A straightforward implication of rejection of the CPR null model by the summary metrics as seen in this work would be the inability of the CPR null model to fit all of the statistical properties of the resting state fMRI data. This provides support for time-varying connectivity models to study FC; however, the best model of FC data (i.e. by "states" or "meta-states" as used in this paper or with other proposed dynamic models in the time-varying FC literature) is still a matter of debate. It must also be noted that there could be several diverse ways of capturing the temporal dynamics in fMRI data and in turn illuminating the brain function; the methods studied in this paper do not claim a specific number of states in the fMRI data any more than a specific number of resting state networks in fMRI data could be claimed. Rather, the focus is on illustrating that such a decomposition may be useful for studying the brain, and this necessitates the ability to identify stable connectivity patterns from the data that can replicate, and which show similar temporal dynamic properties. There is already evidence for usefulness of the dynamic state models explored in this work as previous work has demonstrated that such patterns are better than static connectivity at predicting patient groups which suggests that such decompositions as explored may be useful for helping differentiate patients and controls (Damaraju, Allen et al. 2014, Rashid, Damaraju et al. 2014, Yu, Erhardt et al. 2015, Du, Pearlson et al. 2016, Miller, Yaesoubi et al. 2016).

Chapter 5: Characterizing Diseased Brain Conditions by Multimodal Fusion of Time-Varying Functional Connectivity State Profiles and Gray-Matter Feature Spaces

This chapter demonstrates a disease characterization framework based on multimodal fusion of the sMRI and fMRI modalities. This framework proposes use of the time-varying FC state profiles as features from the fMRI modality with an ultimate objective of revealing and understanding disrupted links in brain structure and function in the diseased brain. The motivation section introduces the benefits and different approaches of multimodal fusion followed by a discussion of the selected feature spaces for fusion in scope of this work.

5.1 Motivation

Studies leveraging the above mentioned multivariate approaches have revealed significant information on clinical aspects of schizophrenia as discussed in several recent reviews on multimodal fusion (Bießmann, Plis et al. 2011, Schultz, Fusar-Poli et al. 2012, Sui, Adali et al. 2012, Lahat, Adali et al. 2015, Calhoun and Sui 2016). Simultaneous analysis of anatomical and functional connectivity in Skudlarski, Jagannathan et al. (2010) suggested that fusion allowed identification of deficits in white matter anatomy, and complex alterations in FC. In another multivariate, multimodal analysis, Michael, Baum et al. (2010) fused structural and functional brain images to reveal decreased overall structure-function linkage in schizophrenia as compared to healthy controls both in a working memory and an auditory sensorimotor task. Camchong, MacDonald et al. (2011) revealed convergent findings in multiple modalities (DTI and fMRI) consistent with the disconnection hypothesis in medial frontal regions in subjects with schizophrenia. Joint

ICA was used in Sugranyes, Kyriakopoulos et al. (2012) to characterize linked functional and white-matter changes related to working memory dysfunction, and in Stephen, Coffman et al. (2013) to identify structure-function relationships using MEG and DTI modalities. The latter study concluded impairments in a posterior visual network in schizophrenia, with reduced FA and MEG amplitude, and overall weaker cognitive performance. Furthermore, Xu, Pearlson et al. (2009) used joint source based morphometry (joint SBM) to identify linked white and gray matter (GM) differences in regions comprising temporal-corpus callosum, occipital/frontal-inferior fronto-occipital fasciculus, parietal/frontal-thalamus and frontal/parietal/temporal-superior longitudinal fasciculus.

Using the mCCA multivariate algorithm, Sui, Pearlson et al. (2015) identified linked structural and functional deficits in distributed cortico-striato-thalamic circuits and their association with cognitive impairments as measured through the Measurement And Treatment Research to Improve Cognition in Schizophrenia (MATRICS) consensus cognitive battery (MCCB). Finally, several classification studies have made use of multivariate, multimodal approaches to demonstrate improved classification with use of multiple modalities as compared to the use of a single modality in classifying patients from controls (Yang, Liu et al. 2010, Ulaş, Castellani et al. 2011, Nieuwenhuis, van Haren et al. 2012, Sui, He et al. 2013, Peruzzo, Castellani et al. 2015, Cabral, Kambeitz-Ilankovic et al. 2016, Cetin, Houck et al. 2016).

As discussed earlier, recent work assessing dynamic (i.e. time-varying) functional network connectivity (dFNC) suggests availability of substantial information beyond time-averaged FC estimates in both resting state and task based (Hutchison, Womelsdorf et al.

2013, Calhoun, Miller et al. 2014, Preti, Bolton et al. 2016). Several studies have shown the above discussed time-varying FC states to be functionally and behaviorally relevant by demonstrating direct links with signatures of consciousness (Hutchison, Womelsdorf et al. 2013, Amico, Gomez et al. 2014, Hudson, Calderon et al. 2014, Barttfeld, Uhrig et al. 2015, Wang, Ong et al. 2016), tracking day-dreaming/mind-wandering (Kucyi and Davis 2014, Kucyi 2017), sleep and awake states (Tagliazucchi and Laufs 2014), ongoing cognitive function and performance (Craddock, James et al. 2012, Schaefer, Margulies et al. 2014, Gonzalez-Castillo, Hoy et al. 2015, Madhyastha, Askren et al. 2015, Shine, Bissett et al. 2016, Shine, Koyejo et al. 2016).

Furthermore, evidence of potential electrophysiological signatures of dynamic BOLD FC also hints the fluctuations in the BOLD FC (as captured in the states) to be interesting i.e. having a neurophysiological origin (Tagliazucchi, von Wegner et al. 2012, Chang, Liu et al. 2013, Allen, Damaraju et al. 2017), although further confirmation is still needed. Besides, several studies have also used time-varying connectivity measures to characterize pathophysiology i.e. identification of disease states (Damaraju, Allen et al. 2014, Rashid, Damaraju et al. 2014, Yu, Erhardt et al. 2015, Du, Pearlson et al. 2016, Miller, Yaesoubi et al. 2016). The proven replicability and statistical significance of these fMRI features, and the above listed utilities make a compelling case for their use as features for the fMRI modality in a multimodal study.

In this work, we focus on feature based fusion analysis of brain structural (sMRI) and functional (fMRI) images hypothesizing correspondence between brain structure and function, or more specifically, the feature spaces of the two studied modalities. We propose exploring where and how gray matter (GM) corresponds to time-varying functional

connections will improve our understanding of both structural and functional connectivity. We estimate the feature space for the functional data as subject-specific states that are revealed from the wFC data using a novel framework featuring temporal ICA and dual regression (Figure 5-1A). More specifically, aggregate states are estimated by decomposing the wFC data using temporal ICA in the first step, followed by a dual regression analysis to estimate the subject-specific states in the second step. This derived feature space from fMRI data, referred to as "functional data feature space" hereon, is simultaneously analyzed with the corresponding "structural data feature space", i.e. GM maps from sMRI data, using the mCCA+jICA data fusion algorithm.

The fusion analysis in this work could be explained in a four-stage process (Figure 5-1B). In the first stage, mCCA reveals links between the modalities by maximizing the correlations between their mixing matrices i.e. CVs. In the second step, the associated maps to the CVs, i.e. the CCCs, are concatenated and decomposed using joint ICA to estimate the joint sources. In the third step, the (effective) modality-specific mixing matrices are estimated for the combined framework and analyzed for group differences for each joint source. In the last step, we focus on qualitative analysis of the joint sources that feature linked, highly correlated and significant group difference showing structural and functional component maps from the jICA decomposition.

Our exploratory investigation on data from 151 Schizophrenia patients and 163 healthy controls shows general correspondence between GM and time-varying FC and also reveals few missing links in Schizophrenia, details of which are presented in the following sections of this chapter.
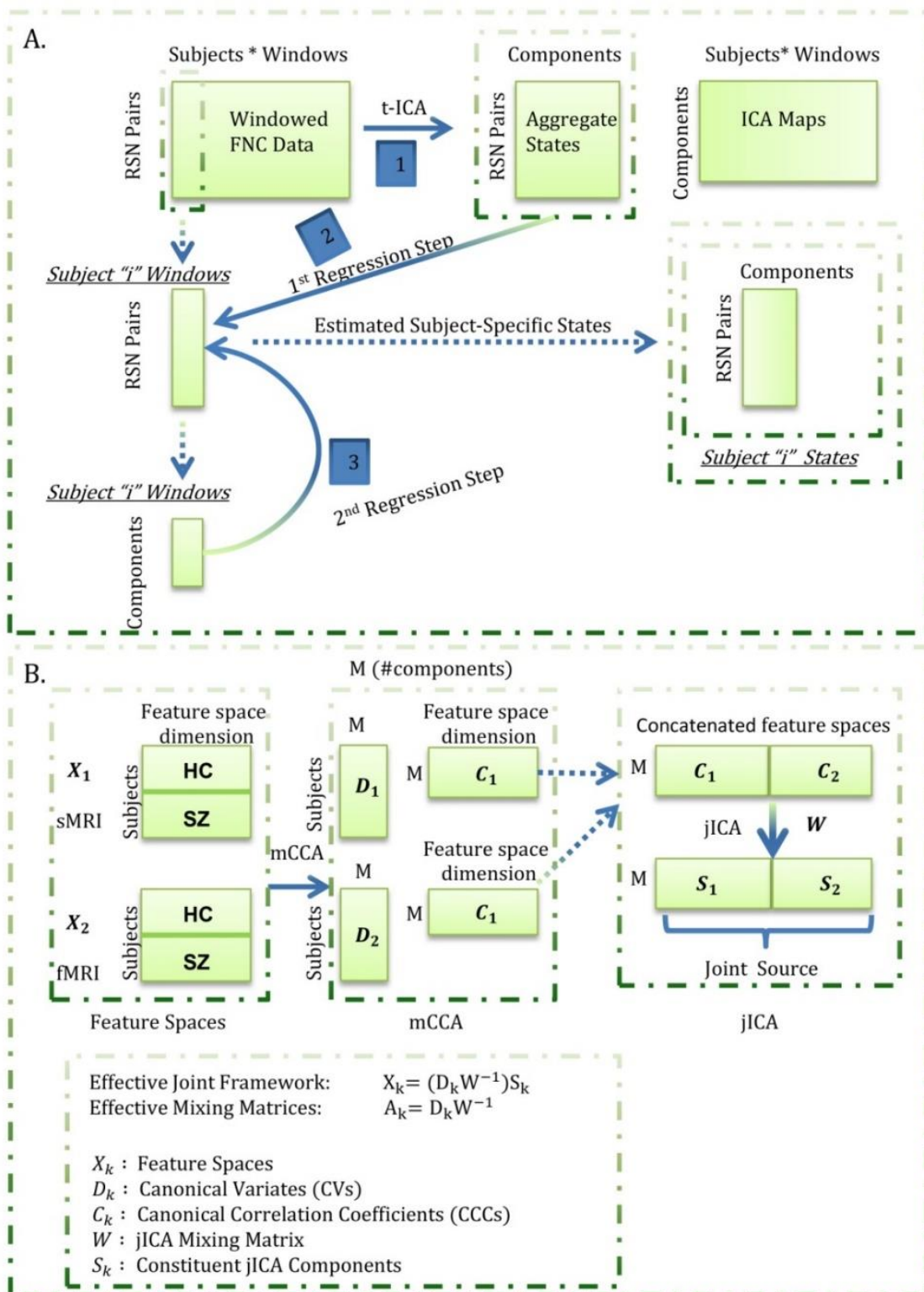
Figure 5-1(A) Estimation of the functional (fMRI) data feature space. Aggregate states were estimated by decomposing the windowed correlations by temporal ICA. Subject-

specific states were next estimated through a spatio-temporal (dual) regression procedure wherein, for each subject, the aggregate states were regressed into the subject's windowed FNC data to estimate subject-specific component time-courses in the first regression step, and the estimated time-courses were regressed into the subject's windowed FNC to derive the subject-specific states in the second regression step; (B) Summary of the mCCA + jICA framework. For each subject, the functional data feature space as estimated in (A) was concatenated with the smoothed, modulated and warped gray matter maps (as the structural data feature space) and fused using the joint "mCCA+jICA" framework. This framework combines the mCCA and jICA algorithms to decompose the observed data into a linear combination of sources mixed through "effective" modality-specific mixing matrices as illustrated above.

5.2 Materials and Methods

5.2.1 Multimodal Data Acquisition and Preprocessing

This study worked with T1-weighted structural and T2*-weighted resting state (eyes-closed) functional images from 151 Schizophrenia patients (114 males, 37 females; average age 37.8), and age and gender matched 163 healthy controls (117 males, 46 females; average age 36.9). This data was collected at seven different sites across the United States as a part of the fBIRN data repository (Keator, van Erp et al. 2016). Informed consent was received from the participants as per institutional guidelines practiced at the 7 collection sites.

Six sites used the 3T Siemens Tim Trio System while one site used the 3T General Electric Discovery MR750 scanner. A total number of 162 volumes of standard gradient echo planar imaging (EPI) BOLD fMRI data were captured with a repetition time (TR) of 2 seconds, echo time (TE) of 30 seconds, field of view (FOV) of 220×220 mm (64×64 matrix), flip angle (FA) of 770 and 32 sequential ascending axial slices of 4 mm thickness and 1 mm skip.

The sMRI data were spatial normalized, bias corrected, and segmented using the SPM unified segmentation model in an automated analysis pipeline developed at MRN (Bockholt, Scully et al. 2010) to obtain the smoothed (using a full width half maximum Gaussian kernel of 10mm), modulated and warped gray matter images for all subjects. The GM maps were then used as the input feature space to the fusion algorithm with an objective of estimating the patterns of brain structure that exhibit co-variations across subjects.

The fMRI data were pre-processed using the SPM, AFNI and GIFT toolboxes as well as custom code written in Matlab in a similar fashion as implemented in Damaraju, Allen et al. (2014). Briefly, rigid body motion correction was performed using the INRIAlign SPM toolbox for subject head motion correction. This was followed by slice-timing correction step to account for any timing differences in scan acquisition following which the data were de-spiked using AFNI's "3dDespike" algorithm so as to reduce the impact of outliers.

Next, the data were warped to a MNI template and resampled to 3 mm cubic isotropic voxels. Since the fBIRN data came from multiple sites, the site or scanner variability needed to be smoothed equivalently. This was done using AFNI's "BlurToFWHM" algorithm, an approach that has been shown to decrease scanner-specific variability in smoothness and provide "smoothness equivalence" to the multi-site data (Friedman, Hastie et al. 2008). Finally, the voxel time-courses were variance normalized before running the group independent component analysis (gICA).

5.2.2 Feature Space Estimation

5.2.2.1 Spatial Group ICA, Resting State Network Selection, and Postprocessing

The pre-processed fMRI data were decomposed using spatial group ICA to reveal spatially independent components each with a unique time-course profile (Calhoun, Adali et al. 2001, Calhoun and Adalı 2012). The pre-processed datasets were first reduced to 130 principal components in the time-point dimension at the subject level. Using a (relatively) higher number of principal components at the subject level has been shown to stabilize back-reconstruction and retain maximum variance in the data, and if this is the case the specific number does not substantially impact the results (Erhardt, Rachakonda et al. 2011). Accordingly, the entire dataset was transformed into 130 principal components using standard principal component analysis (PCA) at the subject level in the first data reduction step of the group ICA analysis (similar to Damaraju, Allen et al. (2014) on the same fBIRN phase 3 dataset).

Using a relatively high number of principal components in this step retained a very high percentage of subject level variance (greater than 99.99%). In the second data reduction step, the PCA reduced subject data were then concatenated along the time dimension and further reduced to 100 components by implementing group level PCA. A higher model order for group ICA was chosen to enable a more refined (i.e. finer) RSN parcellation (Kiviniemi, Starck et al. 2009, Abou-Elseoud, Starck et al. 2010), thus allowing evaluation of sub-nodes within network domains (Allen, Damaraju et al. 2012, Sockeel, Schwartz et al. 2016, Abrol, Damaraju et al. 2017, Fu, Tu et al. 2017, Li, Zhang et al. 2017). The reliability of the estimated independent components from this step was

evaluated using ICASSO (Himberg, Hyvarinen et al. 2004), and it was found that the estimates exhibited tight clustering and converged consistently amongst several (twenty) runs. Finally, subject-specific component spatial maps (SMs) and time-courses (TCs) were estimated using the GICA back-reconstruction methods as implemented in the GIFT toolbox (Erhardt, Rachakonda et al. 2011).

The back-reconstructed subject-specific SMs and TMs for the 100 independent components were extensively analyzed to identify the physiological non-artefactual, previously established resting state networks (RSNs). More specifically, 47 components whose spatial maps showed peak activations in gray matter and low overlap with any known imaging, physiological or movement-related artifacts, and mean power spectra exhibited higher low frequency content were established as RSNs for further analysis. The RSNs were assessed and distributed into the sub-cortical (SC), auditory (AUD), visual (VIS), sensorimotor (SM), attention/cognitive control (CC), default-mode (DMN) and cerebellar (CB) network domains (Figure 5-2).

Subject-specific TCs corresponding to the retained RSNs underwent additional post-processing steps. The TCs were de-trended to remove any existing linear, quadratic or cubic low frequency trends originating from scanner drift, orthogonalized with respect to estimated subject motion and realignment parameters, and de-spiking using AFNI's 3dDespike function to replace outlier points with values estimated from third order spline fit to neighboring portions of the TCs.
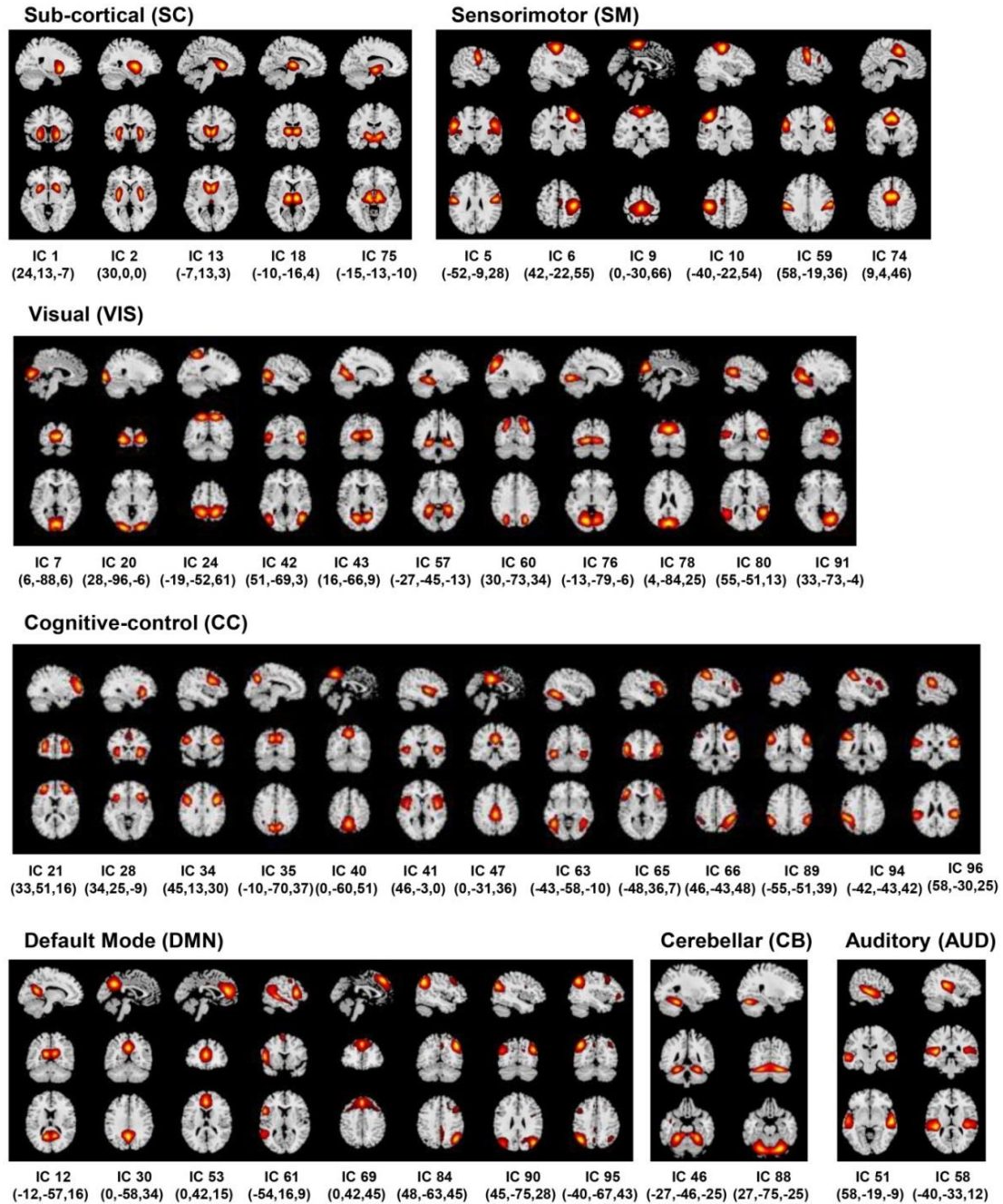
Figure 5-2: Resting State Networks (RSNs). Spatial maps of the forty-seven retained RSNs at the most activated sagittal, coronal and axial slices.

5.2.2.2 Functional Connectivity Estimation and Temporal Variability

Similar to previous works (Allen, Damaraju et al. 2012, Damaraju, Allen et al. 2014), time-varying FC was estimated by sliding a window of length 22 TRs (44 s) in steps of 1 TR (2 s). This sliding window analysis used a tapered window generated by convolving a rectangular window of length 22 TRs (44 s) with a Gaussian window of standard deviation equal to 3 TRs. The window length parameter has a significant impact on the observed dynamics, however our choice of 44 seconds (similar to window duration as used in Damaraju, Allen et al. (2014) on the same fBIRN phase 3 dataset) falls within recommended ranges in multiple works.

In background, Leonardi and Van De Ville (2015) proposed a lower limit for window length using the (inverse of minimum frequency) thumb rule, which Zalesky and Breakspear (2015) formally demonstrated to be overly conservative especially in moderate SNR conditions (i.e. relatively shorter windows than as suggested by the thumb rule can be used to capture the fluctuations in time-varying connectivity).

Moreover, recent studies have reported peak maximum detection probability of time-varying fluctuations (Hindriks, Adhikari et al. 2016) and peaks of significance of window lengths (Liégeois, Ziegler et al. 2016) in a similar (40 to 60 seconds) range. Furthermore, there are several studies that corroborate that varying the window length parameter over a range beyond a certain "safety limit" did not change the overall observed dynamics (Allen, Damaraju et al. 2012, Li, Zhu et al. 2014, Yaesoubi, Miller et al. 2015, Deng, Sun et al. 2016, Preti, Bolton et al. 2016). Hence, we use our previously use window parameters for estimation of time-varying FC.

5.2.2.3 Feature Spaces for Multimodal Fusion

The wFNC data were decomposed using temporal ICA to reveal a set of "n" aggregate connectivity patterns (or aggregate states) shared amongst subjects and a set of "n" temporally independent connectivity patterns. Notably, the "n" temporally independent connectivity patterns are a concatenation of "n" individual subject time-courses which are not independent subject-wise. We estimate the feature space for the functional data as subject-specific "versions" of the aggregate states through a modified form of spatio-temporal (dual) regression (Filippini, MacIntosh et al. 2009, Erhardt, Rachakonda et al. 2011). In this analysis, the aggregate states are regressed into each subject's wFNC data to obtain a set of subject-specific time-courses in the first regression step which are then regressed into each subject's wFNC data to get the subject-specific states in the second regression step. The estimated functional data feature space is next simultaneously analyzed with the GM maps estimated from structural data using the mCCA+jICA data fusion algorithm.

5.2.3 Multimodal Fusion through mCCA + jICA Framework

As a framework to evaluate fusion of feature spaces from two imaging modalities, this method reveals flexible, i.e. both highly and weakly correlated, joint sources from both the modalities. The framework (Figure 5-1B) assumes the multimodal dataset (X_k) to be a linear mixture of a (M) number of sources (S_k) mixed with non-singular matrices (A_k), where k is the modality index. Following (Sui, Pearlson et al. 2011, Sui, He et al. 2013), we used the minimum description length (MDL) criterion to estimate the number of

independent components to be nine. Hence, we evaluate the feature spaces for a total number of nine components ($M = 9$) for both the fMRI and sMRI modalities.

In the first phase of the joint framework, the mCCA algorithm commences with dimensionality reduction of the feature spaces of each of the modalities using principal component analysis. In this work, we reduce the input data to a high (number of subjects - one) number of principal components so as to capture maximum subject level variance. Next, the canonical variates (D_k) are estimated by maximizing the sum of squared correlations (SSQCOR) cost (Kettenring 1971) in the "M" columns of canonical variates. In the last step of the first phase, the canonical correlation coefficients (CCCs) are estimated as associated maps (C_k) by inverting the $X_k = D_k C_k$ model (i.e. $C_k = pinv(D_k)X_k$).

In the second phase of the joint framework, the estimated CCCs are concatenated ($[C_1 .. C_k]$) and input to the jICA algorithm which enables transformation of these CCCs to an orthogonal space. This decomposition reveals "M" maximally independent joint sources (S) each of which can be interpreted as a stacked form of co-varying modality-specific components i.e. $S = [S_1 \ldots S_k]$. The stacked components for the different modalities share a common mixing matrix (W) with the jICA linear mixing model evaluated as $[C_1 .. C_k] = W [S_1 .. S_k]$. Hence, the effective mCCA+jICA can be summarized as $X_k = (D_k W^{-1})S_k$, where the effective modality-specific mixing matrices are estimated as $A_k = D_k W^{-1}$. The combined framework is illustrated in Figure 5-1B and further details on the parametrical and methodological choices in the algorithm can be found in the referenced original works (Sui, Pearlson et al. 2011, Sui, He et al. 2013).

5.3 Results

The mCCA+jICA framework identified two sMRI-fMRI joint sources with (1) significant correlations between their constituent structural and functional components; and (2) significant group differences in each of these constituent structural and functional components. Figure 5-3 and Figure 5-4 show the spatial maps for the constituent structural component, the connectivity strengths for the co-varying functional component's inter-regional connections and other associated results for the first and the second joint source respectively. It must be noted that the constituent structural components in the joint sources estimated here are patterns of brain structure (i.e. clusters of brain voxels) that exhibit co-variations across subjects. These could be interpreted analogous to sources as identified with source based morphometry (SBM) (Xu, Groth et al. 2009, Caprihan, Abbott et al. 2011, Turner, Calhoun et al. 2012, Castro, Gupta et al. 2014, Gupta, Calhoun et al. 2015), an approach that can be essentially considered as a multivariate extension of a voxel based approach, for example, voxel based morphometry (VBM). For display purposes, only the high (and low) activation regions for the structural component and only the edges or connections with high (and low) connectivity strengths for the functional component are shown. More specifically, the structural component maps are lower thresholded at 25% of the maximum absolute activation value, whereas for the functional component, the inter-regional connectivity strengths, after converting to z-scores are thresholded at $|z| > 3$. For the functional component, we will hereon refer to the (post-thresholding) retained inter-regional connections as "significant links".

5.3.1 Resting State Networks

The retained 47 RSNs were assessed and distributed into the sub-cortical (SC), auditory (AUD), visual (VIS), sensorimotor (SM), attention/cognitive control (CC), default-mode (DMN) and cerebellar (CB) network domains (Figure 5-2).

5.3.2 Joint Source 1

As illustrated in Figure 5-3A, the structural component for the first joint source consists of peak activations in the superior parietal lobule (major constituent), precuneus, postcentral gyrus and inferior parietal lobule. The number of significant connections in the linked functional component were high for the default mode, cognitive control and visual network domains in state 2, whereas the other states had a lot fewer total number of significant connections (five in state 4, one each in states 1 and 5, and none in state 3) as seen in Figure 5-3B. For this joint source, these constituent co-varying structural and functional components were found to be significantly correlated (r = -0.28, p = 1.08 x 10^{-6}) as also evident from the scatterplot of their loading parameters in Figure 5-3C. Since negative correlation was observed, participants showing lower gray matter loadings generally exhibited higher connectivity strength in the functional connections. Finally, the structural component showed significant group difference (p = 0.0032) with a significantly lower group mean of the loadings for patients with SZ (Figure 5-3D), whereas its linked i.e. co-varying functional correlate also showed significant group difference (p = 0.0072) with a significantly lower group mean for controls.

5.3.3 Joint Source 2

The structural component for the second joint source depicted in Figure 5-4A consisted of two major positively activated regions. The first major activation comprised regions from the medial frontal gyrus and superior frontal gyrus, whereas the second major activation comprised regions from the superior temporal gyrus, inferior temporal gyrus, insula, fusiform gyrus and middle temporal gyrus. The number of significant connections in the linked functional component were high particularly for the default mode, cognitive control and visual network domains in state 1 (an observation similar to state 2 of the functional component corresponding to the first joint source) and moderate for the cognitive control, sensorimotor, and visual domains in state 2, whereas the other states had a lot fewer total number of significant connections (one each in states 4 and 5, and none in state 3) as seen in Figure 5-3B. For this joint source, these constituent co-varying structural and functional components were found to be significantly correlated ($r = -0.40$, $p = 3.91$ x 10^{-13}) and the corresponding scatterplot of their loading parameters can be seen in Figure 5-4C. Similar to the first joint source, since negative correlation was observed, participants showing lower gray matter loadings had higher connectivity strength in the functional connections. Finally, the structural component showed significant group difference ($p = 0.0022$) with a significantly reduced group mean for the SZ patients, whereas its linked i.e. co-varying functional correlative also showed significant group difference ($p = 0.0438$) reflecting a significantly lower group mean for controls.
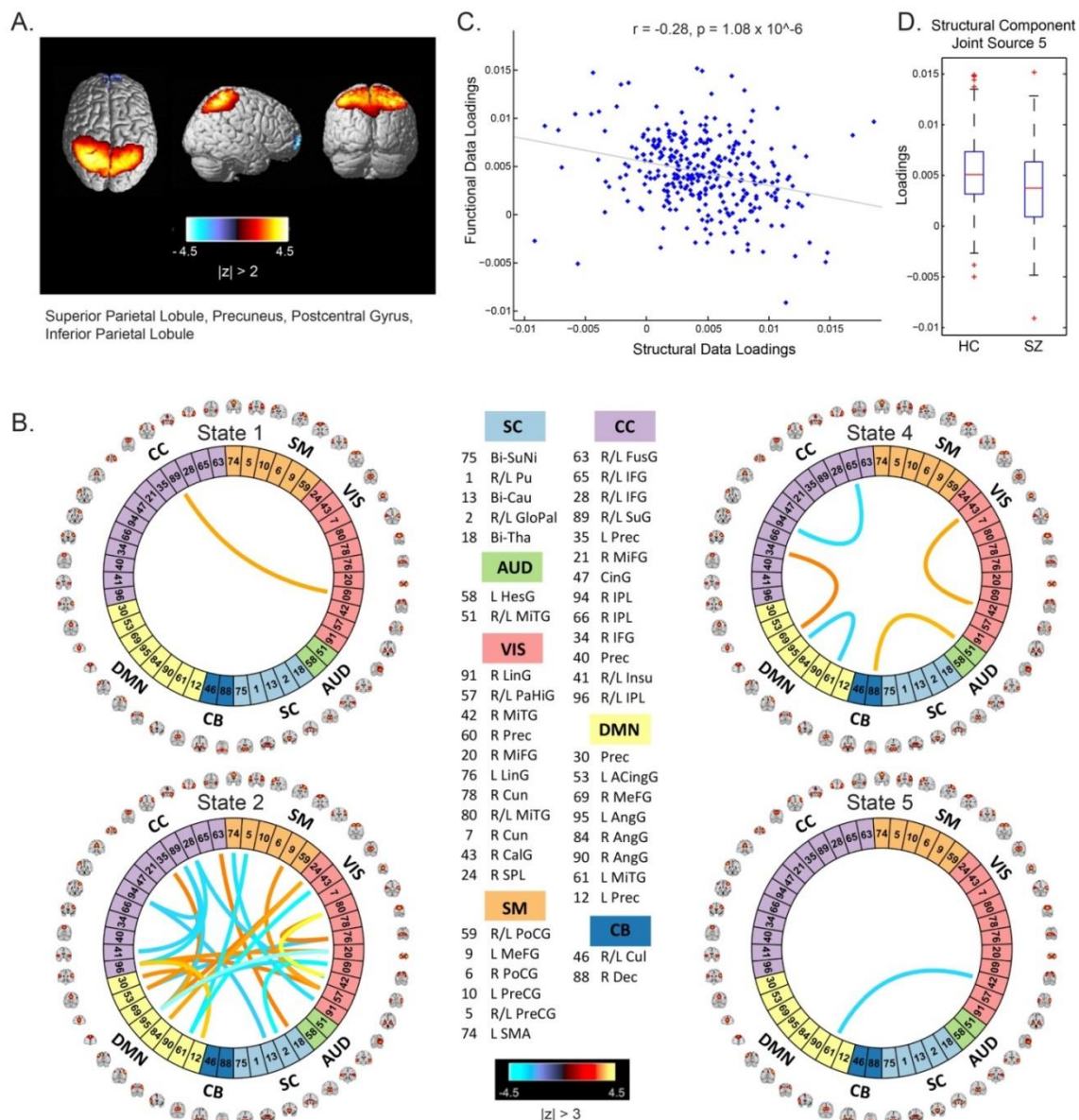
Figure 5-3: Joint Source 1. (A) Spatial maps of the most activated regions for the structural component in the first joint source; (B) A visualization of significant links (functional connections with highest connectivity strengths i.e. with z-scores of connectivity strengths: |z| >3) and their connectivity strengths for the functional component in the first joint source; (C) Scatterplot of the functional data loadings with the structural data loadings revealed a significant correlation (r = -0.28, p = 1.08 x 10-6); and (D) The group mean for the loading parameters was significantly lower for participants with SZ, thus suggesting significant reductions in gray matter volume for this structural component.

Figure 5-4: Joint Source 2. (A) Spatial maps of the most activated regions for the structural component in the second joint source; (B) A visualization of significant links (functional connections with highest connectivity strengths i.e. with z-scores of connectivity strengths: |z| >3) and their connectivity strengths for the functional component in the second joint source; (C) Scatterplot of the functional data loadings with the structural data loadings revealed a significant correlation (r = -0.40, p = 3.91 x 10-13); and (D) The group mean for the loading parameters was significantly lower for participants with SZ, thus suggesting significant reductions in gray matter volume for this structural component.

5.4 Discussion

In this study, we investigated whether a relationship between gray matter and time-varying FC measures exists and if that relationship could be used to study characteristic brain aberrations in SZ. Using a novel, unified framework, we estimated distilled, (relatively) lower-dimensional feature spaces from the high-dimensional fMRI and sMRI data, and then performed joint analysis on the estimated feature spaces leveraging a symmetric fusion approach, mCCA+jICA, to extract jointly co-varying structural and functional components and characterize interactions between these components. In this specific section, we will discuss our results specifically addressing few important questions, such as how the co-variation in the inter-modality components could be interpreted and how the underlying associations are meaningful etc., and finally highlight some critical facets and limitations that could be explored in immediate future work.

Specifically, our results revealed two mCCA+jICA joint sources that featured significant correlation between their constituent modality–specific components and highlighted group difference in both of their modality-specific components. Both the joint sources showed significant negative correlations between their modality-specific constituent components (joint source 1: $r = -0.28$, $p = 1.08 \times 10^{-6}$; joint source 2: $r = -0.40$, $p = 3.91 \times 10^{-13}$), as seen in Figure 5-3C and Figure 5-4C. This implies that from joint source 1, for a given subject, if the gray matter volumes in the positively activated regions in the structural component (superior parietal lobule, precuneus, postcentral gyrus and inferior parietal lobule) are estimated to be higher, it will exhibit significantly decreased connectivity strength in the inter-regional links in the functional component (i.e. the absolute magnitude of inter-regional links with positive connectivity strengths in the

functional component will show significant decrease, and the absolute magnitude of inter-regional links with negative connectivity strengths in the functional component will show significant increase). Alternatively, decreased observed gray matter volumes in the positively activated regions would imply higher connectivity strengths in the significant functional links for that given subject. Similar inferences can be deduced for source 2 wherein changes in gray matter volumes in both of the positively activated distinct regions in the structural component (i.e. medial frontal gyrus and superior frontal gyrus; and superior temporal gyrus, inferior temporal gyrus, insula, fusiform gyrus and middle temporal gyrus) would drive the estimated significant inter-regional links accordingly.

An introspection of the modality-specific components of the joint sources revealed several lines of evidence of conformance with previously reported findings in the literature as discussed next. To begin with, the structural components in both joint sources showed significant group differences in the loading parameters (joint source 1: $p = 0.0032$; joint source 2: $p = 0.0022$), with significantly lower group mean for the SZ group, thus suggesting a significant decrease in gray matter volume in the brain regions depicted by these components in participants with SZ. Our results are consistent with several previous studies (as discussed in detail next), where reduced gray matter volume in SZ has been reported in the similar brain regions as identified in our structural components. The first joint source highlighted peak activations in the superior parietal lobule (major constituent), precuneus, postcentral gyrus and inferior parietal lobule brain regions as the structural modality component (as illustrated in Figure 5-3A). Interestingly, a recent study on source-based morphometry (SBM) and voxel-based morphometry (VBM) evaluating gray matter abnormalities in SZ patients also found a similar structural component showing positive

activation patterns and that captured group differences between SZ and healthy controls (Gupta, Calhoun et al. 2015). Besides, previous studies have also concluded reduced gray matter volume in superior parietal regions (Buchanan, Francis et al. 2004), precuneus (Hulshoff Pol, Schnack et al. 2001) and postcentral gyrus (Glahn, Laird et al. 2008); thus our work adds further evidence that abnormal patterns of gray matter volume in these regions play an important role as SZ biomarkers. Similar evidence could be established for the significant structural component in the second joint source captured by our framework (as illustrated in Figure 5-4A). This structural component included two major positively activated brain regions, where one of them consisted of regions from the medial frontal gyrus, anterior cingulate and superior frontal gyrus, and the other included regions from the superior temporal gyrus, inferior temporal gyrus, insula, fusiform gyrus and middle temporal gyrus. Particularly, the anterior cingulate has been recognized as a vital structure for social cognitive processing and has been previously identified as one of the major sources of social dysfunction in SZ patients (Fujiwara, Hirao et al. 2007). Additionally, very-similar fronto-temporal gray matter changes capturing group difference between SZ and healthy participants were also found in Gupta, Calhoun et al. (2015). In fact, there are several other studies/reviews on gray matter differences in SZ patients that have suggested significant reduction in gray matter volume in the temporal and frontal cortices (Shenton, Dickey et al. 2001, Thompson, Vidal et al. 2001, Giuliani, Calhoun et al. 2005).

Significant correspondence with previously reported studies in literature could also be drawn for few evaluated significant inter-regional (i.e. inter-RSN) links in the estimated functional components. Firstly, the functional components for both of the retained joint sources showed significant connectivity links in time-varying connectivity states 1, 2, 4

and 5. For the first functional component (joint source 1), most of the significant inter-RSN links are captured in state 2, where both positive and negative connectivity strengths across various network domains can be observed (Figure 5-3B). In this state, RSNs in the DMN domain showed significant connectivity within themselves and with RSNs from CC, SM and VIS domains as well. Interestingly, one of the DMN RSNs, IC95, highlighted by the brain regions in left angular gyrus, showed positive connectivity weight with a RSN from the CC domain, IC35, left precuneus. This is in line with a previous study that has shown aberrant connectivity patterns between angular gyrus and precuneus in SZ patients (Rashid, Damaraju et al. 2014). Indeed, studies have widely reported the involvement of angular gyrus in language processing, memory and social cognition (Hall, Fussell et al. 2005, Binder, Desai et al. 2009, Price 2010, Clos, Langner et al. 2014), and abnormal connectivity patterns in SZ in the precuneus, which is involved in episodic memory (Rugg and Henson 2002), mental imagery recall (Fletcher, Shallice et al. 1996) and self-processing operations (Cavanna and Trimble 2006). Furthermore, several studies have shown strong evidence of disrupted DMN connectivity in SZ patients (Garrity, Pearlson et al. 2007, Ongur, Lundy et al. 2010), and so it would be interesting to explore significant links involving the DMN RSNs. As an example, in state 2 of this functional component (joint source 1), we observed negative connectivity strength between another DMN component (IC61: left middle temporal gyrus) and a VIS RSN (IC43: right calcarine gyrus), while the same DMN RSN (IC61) showed negative connectivity strength with a SM RSN (IC5; bi-lateral precentral gyrus) as well. For this functional component (joint source 1), we also note that the other states in this functional component (i.e. states 1,4 and 5) showed significant inter-RSN links between VIS and CC domains (state 1), between DMN and CC, between AUD and

CB domains, within DMN, CC and VIS domains (state 4), and between DMN and VIS domains (state 5). Furthermore, an examination of the functional component from joint source 2 revealed some interesting significant links in state 1, the most densely connected state (Figure 5-4B). In this state, a DMN RSN (IC95; left angular gyrus) showed significant positive connectivity strength with a CC RSN (IC35; left precuneus), an observation also found in state 2 emergent in the first joint source. Again, similar to state 2 from the first joint source, another DMN RSN (IC61; left middle temporal gyrus) showed significantly positive connectivity strength with the same CC RSN (IC35; left precuneus). In fact, dysfunctional temporal lobe connectivity has been reported in several SZ connectivity studies (Shenton, Kikinis et al. 1992, Ford, Mathalon et al. 2002), suggesting that networks from the temporal regions play a significant role in SZ etiology. Finally, for this functional component (joint source 2) the other states (i.e. states 2, 4 and 5) showed significant inter-RSN links from the DMN, CC and SM and CB domains.

While we closely evaluate a few interesting connections in scope of this work, there is much more that could be done to evaluate these results to further enhance our understanding of the structure-function relationships and further contribute to characterizing schizophrenia. In the specific context of findings from our mCCA+jICA based framework as studied in this work, it would be most appropriate to first extensively validate the significant findings in a future analysis evaluating multiple multimodal datasets featuring SZ participants. We also note that while different combinations of cost functions and model orders can yield equivalent results, they can also introduce decompositions different to a degree; hence, comparing performance of the mCCA+jICA approach for a range of these parameters would be another interesting future work. Further

investigations could also benefit from evaluating associations between SZ risk factors and the structural and functional component patterns.

In conclusion, multimodal data fusion through symmetric approaches provides an opportunity to understand brain complexities. Using a multivariate symmetric fusion approach, we were able to identify co-varying GM and time-varying FC components that revealed disrupted links in Schizophrenia. This highlights the utility of time-varying FC based features for disease characterization. We suggest that studying such interactions can provide a useful way of evaluating structure-function relationships and characterizing SZ or other brain conditions.

Chapter 6: Predicting Diseased Brain Conditions by Deep Multimodal Fusion of Time-Varying Functional Connectivity State Profiles and Gray-Matter Feature Spaces

This chapter demonstrates development and application of a multimodal data fusion framework that uses a deep learning framework to extract non-linear features from the gray matter maps and fuses these sMRI features with the time-varying FC state profiles (fMRI features) to predict progression to diseased brain conditions. In the first part of this chapter, we explore the predictive power of the tested deep-learning-based non-linear feature extraction framework using sMRI modality alone to substantiate its utility in the multimodal (sMRI-fMRI) fusion framework developed to predict progression to Alzheimer's disease (AD) in the later part of this chapter. Additionally, while, in this study, we test this framework to study and predict progression to AD, application of this framework to study other diseases would be straightforward.

In the motivation section, we discuss the importance of detecting AD early, previous applications of machine learning methods on sMRI data to study AD and a brief outline of the analyses conducted in this chapter.

6.1 Motivation

Dementia is vastly underdiagnosed in most health systems mainly due to lack of educational/awareness programs and accessibility to dementia diagnostic, treatment and care services (Wilkins, Wilkins et al. 2007, Bradford, Kunik et al. 2009, Connolly, Gaehl et al. 2011). Diagnosis typically occurs at relatively late stages, following which the prognosis is poor in most cases since even the state of the art (FDA-approved)

medications in these stages are, at best, only modestly effective in alleviating cognitive and behavioral symptoms of the disease. As such, early therapeutic interventions can not only help to improve the cognitive and behavioral function of the elderly patients, but also empower them to take important decisions about their health care while they can, and significantly improve their overall quality of life.

The most widely reported form of dementia in the elderly population is Alzheimer's disease (AD) that features progressive, irreversible deterioration in memory, cognition and behavioral function. Mild cognitive impairment (MCI) has been identified as an intermediate condition between typical age-related cognitive deterioration and dementia (Markesbery 2010). This condition often leads to some form of dementia (not necessarily AD) and hence is often referred to as the prodromal stage of dementia. However, in absence of an exact (i.e. narrower) prodrome for AD, this broader population of MCI is currently an attractive target for testing preventive treatments of AD. As mentioned before, the currently approved preventive medications are effective only over a limited (early) time period (Casey, Antimisiaris et al. 2010); as such, the modest effectiveness and extremely high costs of these drugs has been a matter of constant debate especially in terms of cost to benefit balance. Hence patients showing MCI symptoms must ideally be diagnosed at early stages and be followed up on a regular basis to identify potential risks of progression to AD (or other types of dementia). Several studies are currently focused in this direction with an impressively increasing collection and study of multimodal neuroimaging, genetic, and clinical data. As a straightforward example, there are as many as thirty-four different live datasets that can be accessed from the Global Alzheimer's Association Interactive Network (GAAIN)

funded by the Alzheimer's Association (GAAIN 2017). Today, out of these impressive data collection efforts, it is especially the longitudinal studies that act as a bridge in between clinical and neuropathological models (Markesbery 2010).

The sMRI neuroimaging modality enables tracing of brain damage (atrophy, tumors and lesions) and assists in ruling out any possible causes of dementia other than AD. This modality has additional advantages for its non-invasive test nature, high spatial resolution, and ease of procedure availability. Over the last two decades, several studies have contributed to the identification of potential AD biomarkers and prediction of progression to AD using sMRI data independently or in a multimodal pipeline (Falahati, Westman et al. 2014, Arbabshirani, Plis et al. 2017, Rathore, Habes et al. 2017, Weiner, Veitch et al. 2017). At the same time, the neuroimaging community has increasingly started to witness successful application of standard (i.e. classical) and advanced (i.e. deep or hierarchical) machine learning (ML) approaches to extract discriminative and diagnostic information from the high dimensional neuroimaging data (Plis, Hjelm et al. 2014, Litjens, Kooi et al. 2017, Shen, Wu et al. 2017, Vieira, Pinaya et al. 2017). ML approaches are being increasingly preferred also because they allow for information extraction at the level of the individual thus making them capable of assisting the investigator in diagnostic and prognostic decision-making of the patients. The ML methods could range from standard classification frameworks (for example, logistic regression or support vector machines) that usually require manual feature engineering as a preliminary step to deep learning architectures that automatically learn optimal data representations through a series of non-linear transformations on the input data space. The last few years have seen an emergence of deep structured or hierarchical computational learning architectures to learn data

representations that enable classification of brain disorders as well as predicting cognitive decline. These architectures hierarchically learn multiple levels of abstract data representations at the multiple cascaded layers, making them more suitable to learn subtle differences in the data. Some popular deep learning architectures including multilayer perceptron, autoencoders, deep belief nets, and convolutional neural networks have indeed been applied for AD classification and predicting progression of MCI patients to AD (Suk and Shen 2013, Falahati, Westman et al. 2014, Liu, Zhang et al. 2014, Chen, Shi et al. 2015, Li, Tran et al. 2015, Liu, Liu et al. 2015, Suk, Lee et al. 2015).

Convolutional neural networks (CNNs) are a class of feed-forward artificial neural networks that have absolutely dominated the field of computer vision over the last few years with the success of strikingly superior image classification models based on models including AlexNet (Krizhevsky, Sutskever et al. 2012), ZF Net (Zeiler and Fergus 2014), VGG (Simonyan and Zisserman 2015), GoogleNet (Szegedy, Liu et al. 2015), and ResNet (He, Zhang et al. 2016). Deep CNN models typically stack combinations of convolutional, batch normalization, pooling and rectifier linear (ReLU) operations as a mechanism to reduce number of connections/parameters in the model while retaining the relevant invariants, and this entire network is typically preceded by a fully connected layer at the end that supports inter-node reasoning. The deep residual neural network (ResNet) learning framework as proposed by He, Zhang et al. (2016) has a similar baseline architecture as the deep CNNs but additionally features parameter-free identity mappings/shortcuts that simplifies gradient flow to lower layers during the training phase. Additionally, each block of layers learns not only from the activations of the preceding block but also from the input to that preceding block. Additionally, in the original work (He, Zhang et al. 2016), these

models have been shown to enable ease and simplification of neural network architecture training, thus allowing them to use deeper networks and effectively enhance the overall learning performance. These networks essentially improve optimization of the "residual" mappings as compared to the collective and unreferenced original mappings (He, Zhang et al. 2016) as we will discuss next in more detail in the methods section.

Enhanced performance of this advanced version of CNNs i.e. the ResNet architecture in the broader imaging community motivated us to explore their prognostic/diagnostic suitability using sMRI data in this work. In a systematic approach, we first comprehensively evaluate the diagnostic and prognostic performance of the ResNet architecture based on an open-source Pytorch GPU implementation (Pytorch 2017) on a large dataset (n = 828; see Figure 6-1 for detailed demographics) featuring cognitively normal (CN), MCI and AD classes.

Following this, we focus on prediction of progression to AD within the MCI class (i.e. predicting which MCI subjects would progress to AD within 3 years) to test the predictive performance of our learning architecture and test robustness of our final predictive model (generated by fine-tuning on all available data) by comparing surrogate models (i.e. models for each cross-validation fold) with the final predictive model, and after that focus on the human brain regions maximally contributing to the prediction of MCI subjects progressing to AD as suggested by the implemented framework. We also present a qualitative analysis of these results discussing the degree of success (in comparison to previously tested machine learning approaches).

After evaluating the performance of the deep learning framework on sMRI data in the first part of this work, the second part of this work conducts a multimodal data fusion analysis using the subset of ADNI subjects that had data for both modalities (sMRI and fMRI) and adequate progression information available. On this smaller multimodal dataset, we conduct unimodal prediction for each modality separately as well as a multimodal prediction analysis by fusing the estimated features from the unimodal analyses. For ease of interpretation, we refer to the prediction analysis in the first part of the work as "SMRI Prediction on Dataset 1", and the three different analyses in the second part of this work as "SMRI Prediction on Dataset 2", "FMRI Prediction on Dataset 2", and "Multimodal Prediction on Dataset 2" respectively. Next, we present the details of the data and methods used in the above analyses followed up by a discussion of the results and limitations of the study.

6.2 Materials and Methods

6.2.1 MRI Data

Data used in this study were obtained from the Alzheimer's Disease Neuroimaging Initiative (ADNI) database (adni.loni.usc.edu). The ADNI was launched in 2003 as a public-private partnership, led by Principal Investigator Michael W. Weiner, MD. The primary goal of ADNI has been to test whether serial magnetic resonance imaging (MRI), positron emission tomography (PET), other biological markers, and clinical and neuropsychological assessment can be combined to measure the progression of mild cognitive impairment (MCI) and early Alzheimer's disease (AD). For up-to-date information, see www.adni-info.org.

6.2.1.1 Dataset 1

The first part of this study worked with all sMRI scans available in the ADNI 1/2/GO/3 phases (as of November 6, 2017) that passed specific class selection criterion and the image preprocessing pipeline quality check. Normal aging controls with no conversions in a minimum of 3 years of follow-up from their baseline scans were retained in the cognitively normal (CN) class. Subjects diagnosed as MCI with no conversions/reversions in a minimum of 3 years of follow-up from their baseline visit were grouped into the stable MCI (sMCI) class, while those converting to AD (multiple conversions excluded) within 3 years were grouped into the progressive MCI (pMCI) class. Subjects diagnosed as AD at baseline and showing no reversions in a minimum of 2 years of follow-up were retained in the AD class. Only the baseline scan for each subject was used in all analyses.

Detailed scanning parameters could be accessed from the ADNI data resource webpage (ADNI). A total number of 830 subjects passed this criterion with further elimination of only 2 subjects that failed the image preprocessing pipeline quality analysis thus resulting in a total sample size of 828 subjects for this work. Figure 6-1 shows the clinical and demographic characterization of these studied CN, sMCI, pMCI and AD classes.

6.2.1.2 Dataset 2

In the second part of this work, the sample size for the subset of subjects with both (sMRI and fMRI) modalities and adequate progression information available, post-quality control, was reduced to 132 (CN: 34, sMCI: 36, pMCI: 24 and AD: 38). Since

very few subjects satisfied the above discussed inclusion criterion for this specific study, the minimum follow-up time criterion was relaxed for the AD subjects from two years to having at least one additional follow-up session (in another visit) in addition to the baseline scanning sessions. Next, we discuss the data preprocessing details for both parts of this work.
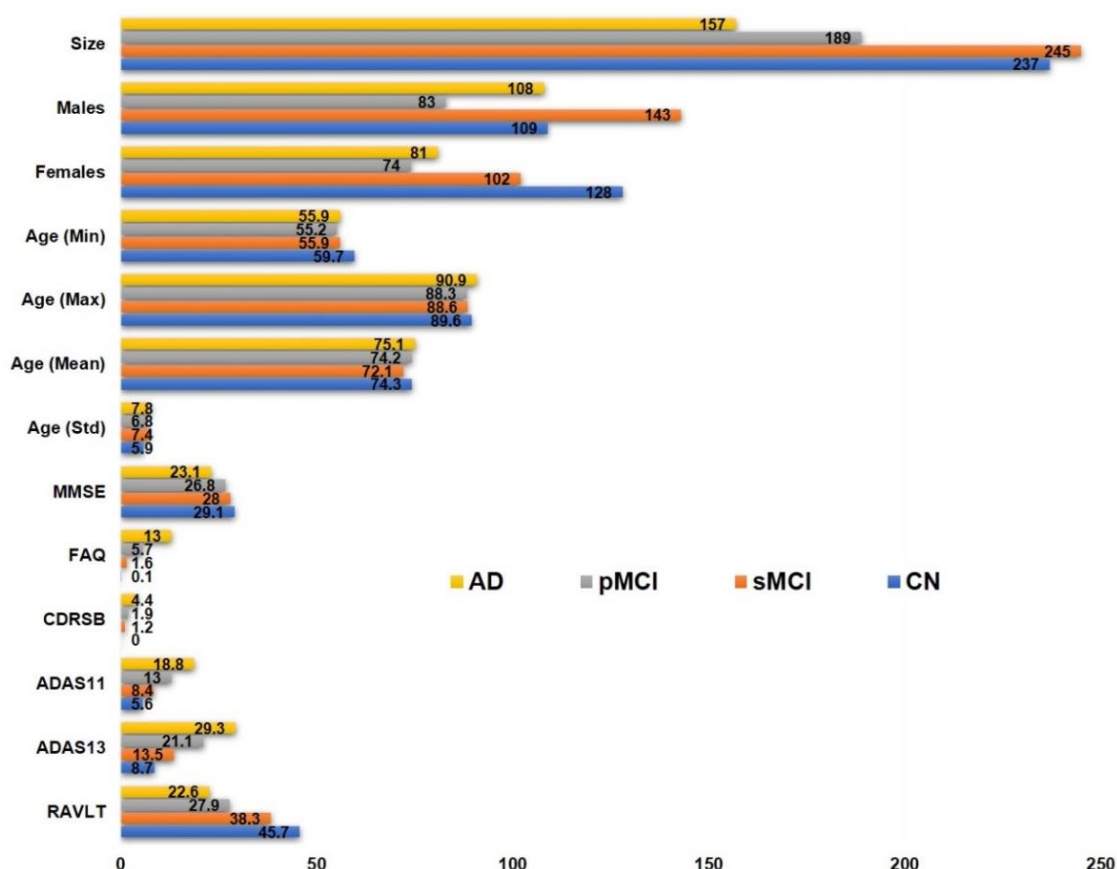
Figure 6-1: A comparison of data demographics and average clinical scores for the studied classes. This study included all subjects in the ADNI repository that passed the minimum selection criterion (minimum follow-up time, conversion or reversion rules) and pre-processing qualitative analysis. Only the baseline scan for each subject was used for all analyses in this study. Clinical scores for diagnosis: MMSE: Mini-Mental State Exam; FAQ: Functional Activities Questionnaire; CDRSB: Clinical Dementia Rating Sum of Boxes; ADAS: Alzheimer's Disease Assessment Scale; RAVLT: Rey Auditory Verbal Learning Test.

6.2.2 Data Preprocessing

6.2.2.1 Dataset 1

For the first part of this work, the sMRI images were pre-processed via the statistical parametric mapping 12 (SPM12) toolbox. The sMRI images were segmented to identify the gray matter brain areas which were spatially normalized and finally smoothed using a 3D Gaussian kernel to 6 mm full width at half maximum (FWHM). The smoothed 3D gray matter images were fed into the deep learning model for diagnostic/prognostic classification.

A quality analysis correlation check was conducted with the population mean thresholded image to eliminate outlier (poorly registered) scans. This quality check discarded only 2 subjects thus retaining 828 out of the 830 subjects that satisfied the selection criterion which we use for the different diagnostic/prognostic classification tasks conducted in the first part of this work.

6.2.2.2 Dataset 2

For the second part of this work, the sMRI scans in the second dataset were preprocessed using a similar pipeline as discussed for dataset 1. As for the fMRI data in the second dataset, Matlab scripts based on statistical parametric mapping (SPM12) software were used. The data pre-processing pipeline integrated removal of the first five images in the scans to avert T1 equilibration effects, rigid body motion correction to correct subject head motion, slice-timing correction to account for timing difference in slice acquisition, warping into the standard Montreal Neurological Institute (MNI) space using

an echo planar imaging (EPI) template, resampling to $3 \times 3 \times 3$ mm^3 isotropic voxels and smoothing using a Gaussian kernel with a full width at half maximum (FWHM) = 6 mm.

For quality control, an average mask using the first time-points of the fMRI images was generated. A correlation analysis was conducted to eliminate outlier subjects whose first fMRI time-point showed a correlation value of less than 0.9 with the estimated average mask. All 134 scans that satisfied the inclusion criterion for the multimodal analysis passed this criterion. Following this, subjects with fMRI scans with excessive head motion (a translation parameter > 3mm or a rotation parameter > 3 degrees) were identified and discarded since repetitions of fMRI scans were not available for these subjects. This quality control procedure discarded 2 subjects, leaving behind a total number of 132 subjects (CN: 34, sMCI: 36, pMCI: 24, and AD: 38) for the unimodal and multimodal prediction analyses on the second dataset.

6.2.3 Deep Residual Learning to Estimate Structural Feature Space

A non-linear, deep residual neural network (ResNet) learning framework (He, Zhang et al. 2016) was used to extract a series of relatively lower dimensional feature spaces from the very high dimensional smoothed 3D images to enhance diagnostic classification as well as identify brain regions affecting progression from MCI to AD. Similar to the deep CNNs, the deep ResNets are small blocks of multiple convolutional and batch normalization layers followed by a non-linear activation function (typically a rectified linear unit). While traditional neural networks (NNs) learn to estimate a layer's or a small stack of layers' output activation (y) as a function (f) of the input image or activation (x) such that $y = f(x)$, ResNets, on the other hand, feature shortcut identity

mappings of input space so as to enable layers to learn incrementally, or in residual representations, with the activations approximated as $y = f(x) + I(x) = f(x) + x,$ where $I(*)$ is the identity function (He, Zhang et al. 2016, He, Zhang et al. 2016). As such, the latter layers in the ResNets learn not only from the output of the previous layer but also from the input to the preceding residual block, thus gaining extra information at each block in comparison to the traditional NNs. The shortcut connection approach in these networks is similar to that suggested in the "highway networks" (Srivastava, Greff et al. 2015), but differs in being parameter-free (i.e. shortcut connections are identity) as compared to highway networks where shortcut connections are data dependent and parameterized. It has been recently shown (Xie, Girshick et al. 2017) that the aggregated transformations in this framework allow for substantially stronger representation powers in a homogenous, multiple branched architecture that strikingly requires setting a very small number of hyperparameters.

6.2.3.1 Dataset 1: ResNet Framework

In the first part of this work (that uses dataset 1), we adapt the ResNet model to evaluate the architecture's performance in pair-wise (binary), mixed-class (binary but using all data by fusing more similar classes hence using more data for training) and multi-class (4-way) diagnostic classifications as shown in Table 6-1. While we focus on the progression of the MCI class to the AD class, all other binary classification tasks were undertaken to confirm appropriateness of learning trends (in terms of classification performance and class separability) in the diagnostic classification of the several disease stages.

Table 6-1: Diagnostic/prognostic classification tasks evaluated through the deep ResNet architecture. Standardized 10-repeat, 5-fold (stratified) cross-validation (CV) framework was employed on each of the mentioned tasks except for the mixed-class task (Task TB below) that varied in that the AD and CN classes were also used for training but only the MCI population was used for testing. Classification task TC corresponds to the multi-class classification task where a four-way classification was performed using the same standardized cross-validation procedure.

Task	Class 1	Class 2	Class 3	Class 4	5-fold stratified CV (10 repeats)
TA1	CN	AD	-	-	Standard Binary
TA2	CN	pMCI	-	-	Standard Binary
TA3	sMCI	AD	-	-	Standard Binary
TA4	sMCI	pMCI	-	-	Standard Binary
TA5	CN	sMCI	-	-	Standard Binary
TA6	pMCI	AD	-	-	Standard Binary
TB	CN, sMCI	pMCI, AD	-	-	Modified Binary; Split MCI subjects only
TC	CN	sMCI	pMCI	AD	Standard 4-way

For this specific part, we use a modified form of an open-source Pytorch implementation of this learning framework (Pytorch 2017) evaluated for different depths, and reducing the final fully-connected layer to class probabilities to verify classification performance and appropriateness for the studied neuroimaging data. The 3D input data (smoothed gray matter maps) are fed into the deep learning ResNet framework (Figure 6-2) which has a series of 3D convolutional units (CUs), 3D batch-normalization units (BNUs) and non-linear activation units (Rectifier Linear Units or ReLUs) followed by a max-pooling unit (MPU) from where features are fed to the following residual blocks (RBs). Each RB has two small stacks of layers, also termed building blocks (BBs), with each BB having two CUs, two BNUs and 1 ReLU in the same specific order (CU-BNU-ReLU-CU-

BNU). Following the original recommendation (Ioffe and Szegedy 2015), BNUs were adopted following every CU and before any activation functions. The activation at the output of the final residual block adder is fed into an average pooling (AP) unit for dimension reduction, and then flattened (from 3D to 1D) to feed a fully connected (FC) layer featuring 512 output nodes. The relatively lower dimensional flattened feature space at the output of the first FC layer (FC1) is fed into a second FC layer (FC2) to estimate the diagnostic class probabilities/scores.

Training and testing routines were implemented on an NVIDIA CUDA parallel computing platform (accessing 3 independent servers each with 4 GeForce GTX 1080 11 GB GPUs) using GPU-accelerated CUDA toolkit/compilation and Pytorch python package tensor libraries. The Adam stochastic optimization algorithm (Kingma and Ba 2015) was preferred for its computational efficiency, relatively little memory requirements, and suitability for problems with large data/parameters size. A batch size of 16, fixed learning rate parameter of 0.001 and L2 weight decay parameter of 0.01 were chosen for the final model selection, and all further classifier performance and feature estimation routines based on a preliminary analysis that suggested (1) insignificant effect of batch-size on learner performance, and (2) the above values of learning rate and L2 weight decay parameter through a grid-search cross-validation analysis.

Due to computational (GPU) memory constraints, we tested only for batch sizes 2, 4, 8 and 16 and since batch-size did not affect performance, the maximum batch-size of 16 was chosen to speed up computations (as compared to batch sizes 2, 4 and 8). Followingly, learner performance for different model depths (number of residual blocks) was compared

to choose the appropriate model depth for consistent comparison across several classification tasks as demonstrated in Table 6-1.
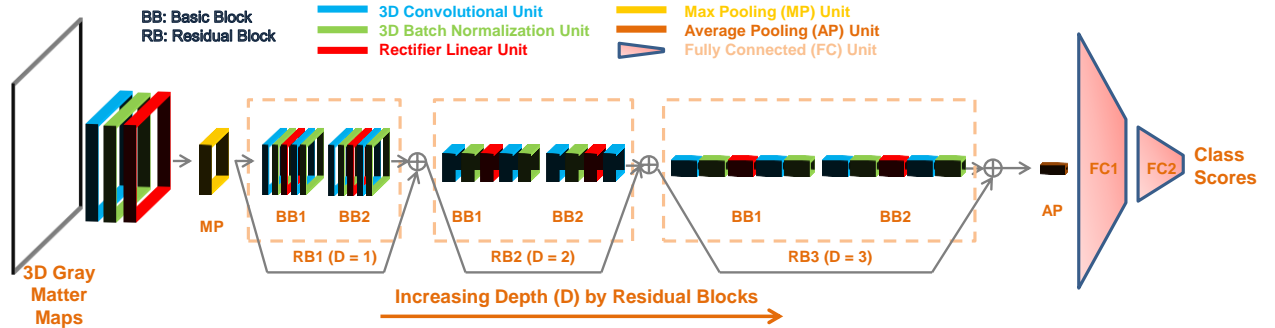
Figure 6-2: A deep residual neural network learning framework is composed of multiple residual blocks that are small stacks of convolutional and batch normalization layers followed by non-linear activation functions such as rectified linear units. In this study, as suggested by the data (Figure 6-5), we use a model with 3 residual layers for evaluating diagnostic classification performance and progression to AD.

6.2.3.2 Dataset 1: Architecture Depth Selection, Regularization and Validation

The ResNet architecture with different depths (*D = 1, 2, 3, 4*; where *D* is number of residual blocks) was tested for diagnostic/prognostic classification performance for the CN vs. AD classification task. We retained the architecture depth with the best performance as suggested in this analysis *(D = 3)* for all other classification tasks for consistent comparison. Figure 6-2 illustrates the modular structure of the selected framework, whereas Figure 6-5 shows a comparison of the model performances at different depths. As shown in Figure 6-2, following the MPU, this architecture featured three RBs followed by two FCUs; hence, in all, thirteen convolutional and two fully connected layers were used in this fifteen-layer model.

Use of BNUs, default L2 weight decay (regularization) in the Adam Optimizer, repeated stratified k-fold cross-validation for the diagnostic/prognostic classification tasks and early stopping were measures undertaken to prevent any overfitting and reduce classification performance bias. This chosen architecture was then used to extract the features and class probability scores for the different binary/mixed-class/multi-class classification tasks as discussed in the following section.

6.2.3.3 Dataset 1: Diagnostic/Prognostic Classification Tasks

Classification performance for the different binary diagnostic/prognostic classification tasks (CN vs. AD, CN vs. pMCI, sMCI vs. AD, sMCI vs. pMCI, CN vs. sMCI, and pMCI vs. AD) for the 4 studied groups was evaluated (Tasks TA1 through TA6 in Table 6-1). Additionally, mixed-class inter-MCI (Task TB: CN+sMCI vs. pMCI+AD; training on all CN and AD data plus 80% of sMCI and pMCI data; testing on 20% sMCI and pMCI data) and multi-class (Task TC: 4-way) classification tasks were performed to enhance classification performance and extract additional information than that conveyed by the binary classifiers respectively. The mixed inter-MCI class classification task was evaluated to explore any additional benefits of domain transfer learning (Cheng, Liu et al. 2015) i.e. if training the classifier with more data samples (i.e. all CN and AD datasets) resulted in an improvement in the classification performance.

While all other classification tasks were conducted to evaluate the framework performance as compared to frameworks used in similar studies in the recent literature, only the mixed/modified inter-MCI classification task that assumes the highest clinical relevance (in terms of learning about progression to AD) was focused on to seek evidence

of the most affected brain areas while progressing to AD. All classification tasks were conducted using repeated (n = 10), stratified 5-fold cross-validation procedures. Classification performance metrics including accuracy, sensitivity, specificity, and balanced accuracy were computed, and additionally complimented by conducting the receiver operating characteristic (ROC) curve analysis to estimate the area under the curve (AUC) performance metric for the various classification tasks.

6.2.3.4 Dataset 1: Model Verification: Testing Filter Weights and Activations

Following the preceding performance analysis of the several diagnostic/prognostic classification tasks, we focused only on the modified inter-MCI (i.e. mixed class; Table 6-1, Task TB) prognostic classification task for identification of the most discriminative brain regions in progression to AD. We hereon refer to the models trained for each cross-validation fold as surrogate models and finetune the final predictive model on all data. In this iterative learning approach, the surrogate models were additionally regularized by use of a validation-error-based early stopping mechanism to avoid overfitting and impose control over the increase in generalization error. As such, the model training phase was simply terminated at a point (iteration number) whereon there was no significant increase in the model performance (in terms of validation accuracy). The number of epochs parameter suggested by the early stopping method was averaged over the cross-validation folds, and the final predictive model was run for this averaged parameter value to allow learning of the final prediction model in a totally unsupervised way. Once the final predictive model was generated, additional tests were performed on filter weights and output activations at the first convolutional layer for each of the surrogate models as well as the final predictive model to ensure proper training which we discuss next.

During the training phase, the network iteratively learns the data and updates the filter weights in the multiple channels of convolutional layers to minimize the training error. Likewise, as in case of any CNN architecture, resembling (i.e. highly correlated) filters almost certainly indicate over-parameterization, or incorrect updating of the loss function and thus inappropriate learning directionality. Hence, we performed a similarity analysis on the weights of the 64 (size 3 x 3 x 3) filters learnt at the first convolution layer as a simple sanity check.

Next, while inference on discriminative brain regions was done from the features from the final predictive models that trained on all data, projections estimated from the surrogate models must ideally confirm similar learning trends i.e. robustness of the extracted features. To inspect this, we compared the activations at the output of the first convolutional layer (post batch-normalization and non-linear activation) for the multiple surrogate models with the final predictive model. Finally, the brain regions most discriminative of likely progression to AD were localized by projecting the sub-sampled mean activations at the output of the first convolutional layer (batch-normalized and post non-linear activation) back to the brain space.

6.2.3.5 Dataset 2: ResNet Framework

For the second part of this work (that uses dataset 2 for unimodal and multimodal prediction), the non-linear sMRI features were estimated using a slightly modified form of the ResNet framework used in the first part. The modified framework for the analyses in this part (on dataset 2) made use of an additional fully connected layer at the end of the network. Hence, in the modified architecture, three fully connected (FC) layers were used

in the ResNet architecture. The first FC layer reduced the preceding input data dimensionality to 512, the second FC layer mapped this 512-dimensional data further down to 5 dimensions and the final FC layer reduced this 5-dimensional data to a 2-dimensional space that represented scores for each of the two classes. For sMRI only prediction using the second dataset, a SoftMax classifier was used to estimate the classification accuracy from the 2-dimensional output of the ResNet; however, the multimodal prediction on the second dataset instead used the 5-dimensional sMRI features estimated at the output of the second FC layer in the modified ResNet architecture. This architecture tweak was enabled specifically to match the output dimension of the sMRI features to the state model order of the fMRI features ($k = 5$) which is discussed in the next section.

6.2.3.6 Dataset 2: Cross-Validation Procedure

All data from the CN and AD groups was used for training; however, stratified, repeated ($n = 10$) k-fold ($k = 3$) cross-validation folds were generated for the MCI data. Notably, as the number of subjects was only 132, fewer folds ($k = 3$) were used in each repetition of cross-validation to keep a large test sample size for reliable cross-validation. For each of the 30 cross-validation folds, early stopping was implemented to select the models that were used to make predictions. This estimated a distribution of the prediction accuracy metric for prediction from the sMRI features (dataset 2) that was later compared to distributions of similar metrics generated from the fMRI and multimodal prediction analyses on the same dataset.

6.2.4 Time-varying FC based Extraction of Functional Feature Space

6.2.4.1 Group ICA

To extract the subject-specific functional networks from the preprocessed fMRI data (dataset 2; n = 132), group information guided ICA (GIG-ICA) as implemented in the GIFT toolbox was used (Du and Fan 2013). For this GIG-ICA decomposition, we used the guiding networks estimated in a prior study (Du, Fu et al. 2018) that used two large, independent datasets of healthy controls to find the most reliable (n = 54) networks common to both used datasets. The retained functional networks were grouped into the sub-cortical (5), auditory (2), sensorimotor (10), visual (9), cognitive control (16), default mode (7), and cerebellar (5) network domains.

6.2.4.2 Time-varying FC

The time-courses estimated from the GIG-ICA decomposition were post-processed by z-scoring, regressing motion, detrending, despiking, and band-filtering (0.01-0.15HZ). The windowed correlation data for each of the $^{54}_{2}C$ (1431) brain connections was then estimated from the post-processed network time-courses using the SWC method. A tapered sliding window featuring convolution of a rectangular window (width = 20 TRs i.e. approximately 60 seconds) with a Gaussian (standard deviation of 3 TRs) was used, and subsequently moved in gradual steps of 1 TR, resulting in 115 windows. Hence, for each subject, a total number of 115 1431-dimensional windows were estimated. The optimal value of number of clusters was estimated to be 5 for this windowed data. However, instead of the standard hard-clustering approach on the entire data, a fold-and-diagnostic-group-specific clustering procedure (as outlined in Figure 6-3) was implemented within the cross-

validation procedure to estimate the prediction accuracy from time-varying FC based fMRI features as discussed in detail in the next section.
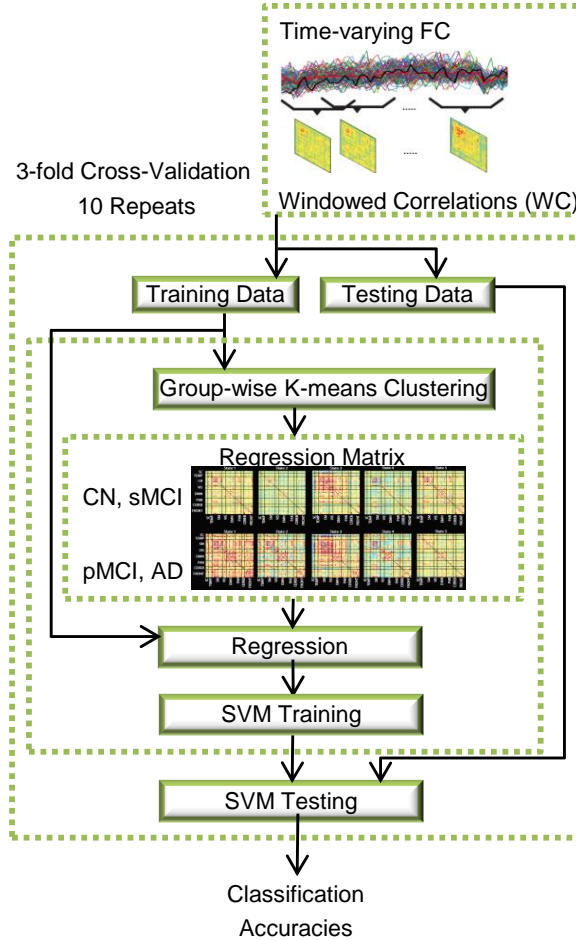
Figure 6-3: Unimodal (fMRI) prediction framework based on fMRI feature estimation from time-varying FC based fMRI feature extraction (Rashid, Arbabshirani et al. 2016).

6.2.4.3 Cross-Validation Procedure

A rigorous, nested cross-validation procedure was implemented to estimate the prediction accuracy of progression from MCI to AD. For a consistent comparison, the exact same folds as used in the sMRI prediction analysis on this dataset (dataset 2) were used. This procedure featured a linear support vector machine (SVM) to measure the disease

prediction performance of the time-varying FC based fMRI features. Furthermore, a FC state regression pipeline, as described next and as previously deployed in Rashid, Arbabshirani et al. (2016), was leveraged to find the subject-specific, lower-dimensional fMRI features to be used to train the linear SVM. The schematic diagram of the employed framework is shown in Figure 6-3.

The FC state regression pipeline involved a fold-and-diagnostic-group-specific clustering to estimate the FC state profiles. In other words, for each fold, the windowed correlation data of training subjects of each diagnostic group were clustered separately to identify the set of diagnostic-group-specific FC state profiles for that fold. Thus, for each fold, for a model order k = 5, and two diagnostic groups, a set of 2*k i.e. 10 FC state profiles were estimated. This set of states was used as a regression matrix to test the contribution of each of the centroids in each of the windowed correlation observations. Hence, each of the windowed correlation observations (for training subjects of both diagnostic groups) for a given fold was regressed onto the estimated regression matrix for that fold, and their contribution weights (i.e. beta coefficients) were computed. The estimated beta coefficients were averaged across all observations (i.e. windows) for each subject, thus resulting in 10-dimensional features for each subject. These features were then used to train the linear SVM in a nested cross-validated setup, where the regularization parameter was optimized in the inner loop and the SVM trained using this optimal hyper-parameter value was used to test the testing samples in the outer loop. Hyper-parameter tuning in the previous step used 50 values from a logarithmic parameter sweep in the range [1e-03, 1e+01]. The entire procedure was repeated for each of the 30 cross-validation folds, thus generating a distribution of the prediction accuracy metric for the time-varying FC

based fMRI features that was later compared to distributions of similar metrics from the sMRI and multimodal prediction analyses.

6.2.5 Multimodal Prediction

The fMRI and sMRI feature spaces estimated from the previous discussed analyses on dataset 2 were fused using canonical correlation analysis (CCA). CCA infers information from the cross-covariance matrix of the features by finding linear combinations of the two feature spaces that maximize their correlations (Sun, Zeng et al. 2005, Haghighat, Abdel-Mottaleb et al. 2016). This method was preferred as it enables generation of a fused feature space that is more discriminative than the individual feature spaces or a simple concatenation of the feature spaces.

Similar to the fMRI and sMRI prediction analyses, a stratified, repeated (n = 10) k-fold (k = 3) nested cross-validation was performed to measure the multimodal prediction performance. For a consistent comparison, the same training and testing folds as in the previous unimodal analyses on dataset 2 were used. For each fold, the fused training features estimated by the CCA algorithm were input to train a linear SVM. To estimate the optimal value of the regularization parameter, a parameter sweep was conducted using fifty logarithmically spaced values of this parameter in the range [1e-03, 1e+01]. The linear SVM was trained on the optimal hyper-parameter value and prediction accuracies on the fused test features were computed. This generated a distribution of the prediction accuracy metric for the multimodal prediction case which was compared to distributions of similar metrics from the fMRI and sMRI prediction analyses. A summary of this three-way comparison is illustrated in Figure 6-4.
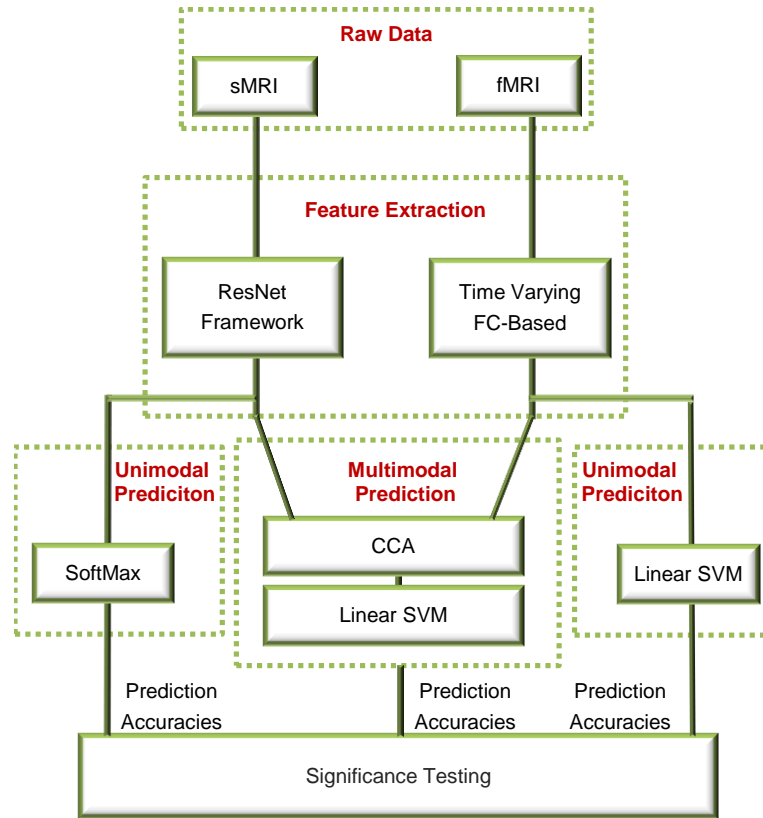
Figure 6-4: An overview of the unimodal and multimodal analyses comparison conducted in this work.

6.3 Results

6.3.1 Dataset 1: Deep Learning Architecture Depth Selection

In a repeated (n=10), stratified 5-fold cross-validation framework, the CN and AD datasets were evaluated for 100 epochs. The stratified cross-validation procedure was performed on the pooled CN and AD classes to study the effect of adding depth to the implemented architecture (i.e. further convolutional layers or residual blocks). This analysis reported significant improvement in validation accuracy by a model that used 3 residual blocks (D3: depth = 3) as compared to a model that used 2 residual blocks (D2:

depth = 2; p = 1.6996e-07) and a model that used 1 residual block (D1: depth = 1; p = 4.5633e-13). Adding another residual block (i.e. depth = 4) did not result in significant improvement in performance; hence, we have settled on the D3 model and validated it in the several classification/prediction tasks, as will be shown in the forthcoming sub-sections. In this particular analysis, the models were run for 100 epochs for each depth and used the exact same training and test datasets in each of the cross-validation folds for consistency in performance comparison. A comparison of training error, training loss and validation error for the different depths is shown in Figure 6-5A. Additionally, the 512-dimensional feature space at the output of the first fully connected layer in the ResNet model was projected onto a two-dimensional space using the t-distributed stochastic neighbor embedding (tSNE) algorithm (Maaten and Hinton 2008) to visualize class separation differences with model order. We show projections from a surrogate model (from a sample cross-validation fold) for a sample epoch around which the D3 model clearly exhibits significant differences in validation accuracy (Figure 6-5B); projections from other surrogate model (from other cross-validation folds) and other epochs beyond the significant difference showing epoch could be expected to exhibit a similar pattern because of evidence from results in Figure 6-5A.
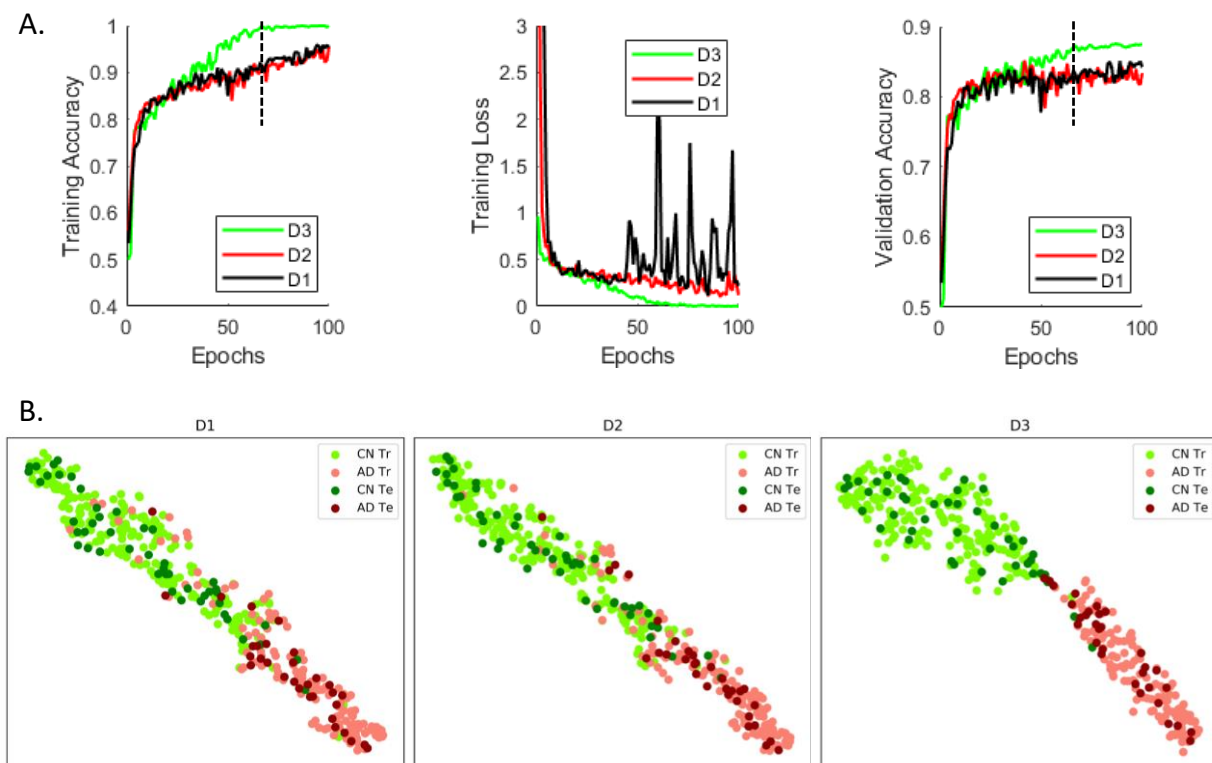
Figure 6-5: (A) Repeated (n=10) stratified k-fold (k = 5) cross-validation was performed on the pooled cognitively normal (CN) and Alzheimer's Disease (AD) classes to study the effect of adding depth (i.e. adding further convolutional layers or residual blocks) in the implemented framework. Significant improvement in validation accuracy was reported by a model that used 3 residual blocks (D3: depth = 3) as compared to a model that used 2 residual blocks (D2: depth = 2; $p = 1.6996e\text{-}07$) and a model that used 1 residual block (D1: depth = 1; $p = 4.5633e\text{-}13$). Adding another residual block (i.e. depth = 4) did not result in a significant improvement in performance; hence, we've settled on the D3 model and validated it in the several classification/prediction tasks for a consistent comparison. For this specific analysis, all models were run for 100 epochs and used the exact same training and test datasets in each of the cross-validation folds for consistency in performance comparison. (B) The feature spaces at output of the first fully connected layer in the three surrogate models (for a sample cross-validation fold at the epoch demonstrated by the vertical black line in Figure 6-5A) were projected onto a two-dimensional space demonstrate additional separation enabled by addition of residual blocks in the 'D3' model as compared to the 'D2' and 'D1' models. The 'Tr' abbreviation corresponds to the training samples whereas 'Te' corresponds to the samples used to test the learnt model.

6.3.2 Dataset 1: Diagnostic and Prognostic Classification Tasks

6.3.2.1 Binary Diagnostic/Prognostic Classification

The performance of the validated (depth = 3) deep learning framework on pair-wise (binary) classification tasks was compared to identify how well the pMCI and AD populations separated from the CN and sMCI populations. The different binary classification tasks were conducted using repeated (n = 10), stratified 5-fold cross-validation procedures and model training was conducted with an early stopping with a patience level of 20 epochs (20% of the set maximum number of epochs) to prevent overtraining the model. The results in Figure 6-6 reflect a clear tend with the average (cross-validated over 50 folds) classification metrics for the classification of CN or sMCI classes from pMCI or AD classes distinctly higher than the average metrics for the CN vs. sMCI and pMCI vs. AD classification tasks. Specifically, for the first four classification tasks (CN vs. AD, CN vs. pMCI, sMCI vs. AD, and sMCI vs. pMCI), we report a cross-validated median accuracy of 91%, 86%, 86% and 77% respectively. The reported sensitivity for these tasks is 85%, 79%, 81% and 71% respectively, whereas the reported specificity is 95%, 92%, 90% and 82% respectively. The learner's appropriate separability trend across the different classes and genuinely high classification metrics as compared to previous findings in literature (reviewed recently in Moradi, Pepe et al. (2015) and Vieira, Pinaya et al. (2017)) in such a large heterogenous sample clearly highlight the usefulness of the deep learning model.
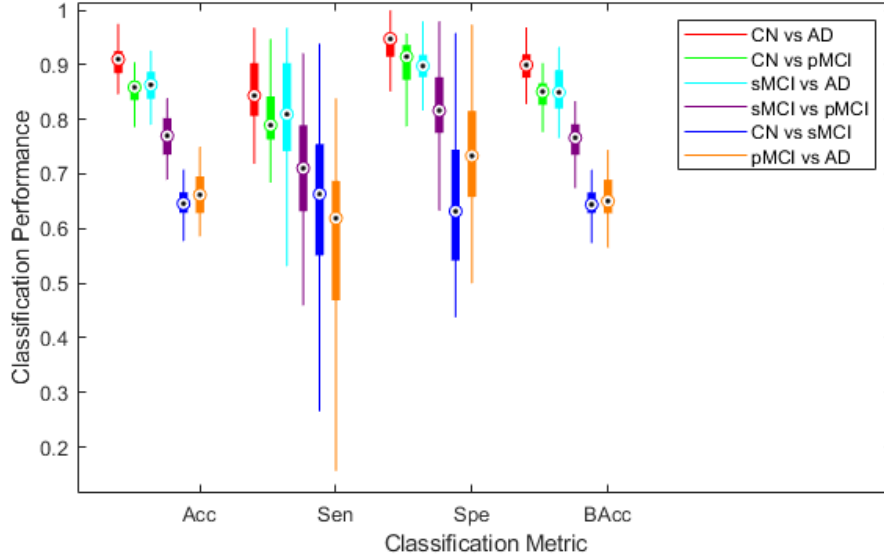
Figure 6-6: Six possible binary diagnostic and prognostic classification tasks from the four studied classes were considered. A repeated (n = 10), stratified 5-fold cross-validation procedure was conducted for each of these classification tasks. The ResNet framework was trained independently for each classification task for a maximum of 100 epochs but with an early stopping with a patience level of 20 epochs (20% of the set maximum number of epochs) to prevent overtraining the model. Classification performance was quantified using the accuracy, sensitivity, specificity, and balanced accuracy metrics. Each boxplot shows a spread of the specific reported metric over the 50 cross-validation folds. The first four classification tasks in specific order as in the legend (CN vs. AD, CN vs. pMCI, sMCI vs. AD, and sMCI vs. pMCI) could be considered more clinically relevant and reported a cross-validated median accuracy of 91%, 86%, 86% and 77% respectively, sensitivity of 85%, 79%, 81% and 71% respectively, and specificity of 95%, 92%, 90% and 82% respectively. The performance in the binary classification tasks is comparable or better than previously assessed machine learning architectures while the number of samples is much higher in this specific study. We further explore possible improvements in prediction of progression to AD in the 'Mixed-class Prognostic Classification' section.

For further introspection into the diagnostic ability of the binary classifiers, we estimated the classification-task-specific receiver operating characteristic (ROC) curves. A comparison of the area under the ROC curve (AUC) metric confirmed a similar trend as suggested in the previous analysis (Figure 6-6) as illustrated in Figure 6-7. We report a cross-validated AUC of 0.93 for CN vs. AD, 0.87 for CN vs. pMCI, 0.89 for sMCI vs. AD and 0.81 for the sMCI vs. pMCI classification tasks. These initial results indicate high

suitability of the evaluated framework for our desired objective; further possible improvements in prediction of progression to AD was explored with the mixed-class prognostic classification analysis as discussed in the next section. This is followed by a thorough, in-depth comparison of our prediction performance with previous literature.
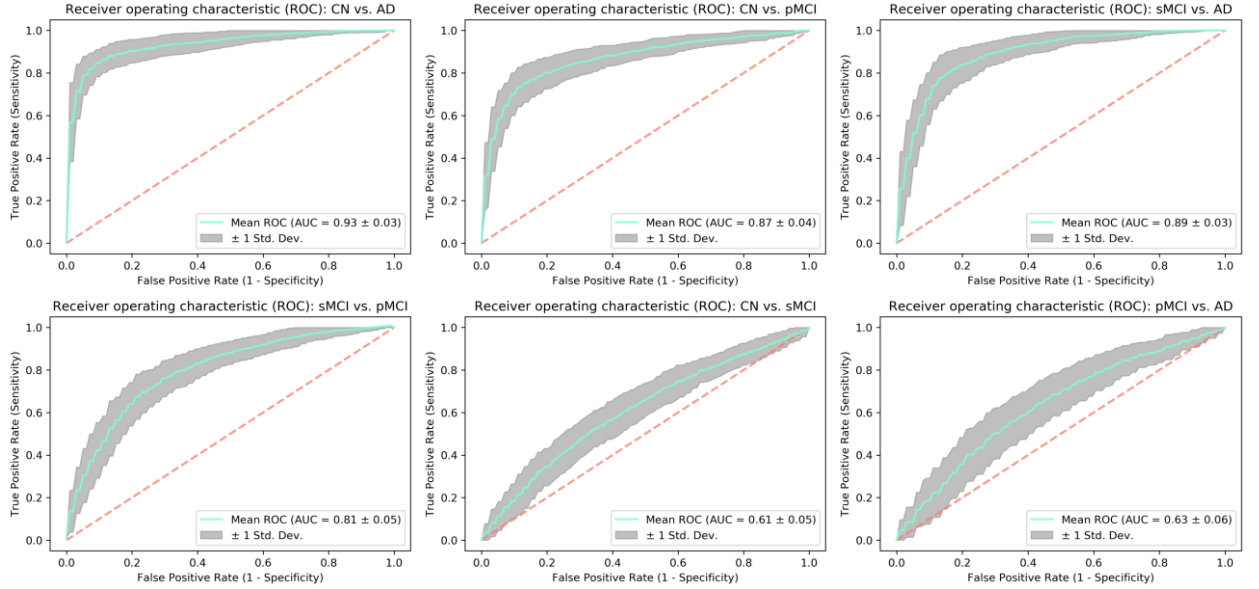
Figure 6-7: Receiver operating characteristic (ROC) curves were estimated for each of the classification tasks to further evaluate the diagnostic ability of the trained ResNet framework. As expected, the reported area under the curve (AUC) metric follows a similar trend as in Figure 6-6 thus further adding evidence to the superior performance of the tested architecture for the undertaken analysis.

6.3.2.2 Mixed-class Prognostic Classification

The sMCI vs. pMCI classification task could be considered as the most clinically relevant task amongst the several binary classification tasks since identifying MCI subjects who are highly likely to progress to AD is very crucial; hence, in this specific analysis we focus on exploring ways to improve separability between these two classes. A recent study (Cheng, Liu et al. 2015) explored advantages of domain transfer learning to enhance MCI

conversion predictability rates which is similar to what we pursue in the section. In general, training the learner with more data is highly likely to improve its classification/prediction performance on unseen data since the learner assimilates the additional variability provided by the previously unseen datasets and adjusts its weights accordingly for more generalized training (i.e. decrease in generalization error). In a scenario where availability of MCI data is severely limited, we hypothesized that training the learner with all data from the CN and AD classes (or domains) together with some part of the two MCI classes (or domains), and then testing with the remaining part of the MCI classes (or domains) could enhance classification performance. For this analysis, we conducted the above discussed modified form of repeated (n=10) stratified 5-fold cross-validation and report significantly improved cross-validated median accuracy of 83%, sensitivity of 78%, and specificity of 87% (Figure 6-8A), and a cross-validated mean AUC of 0.88 (Figure 6-8B). The results clearly reflect substantial improvement (6% in accuracy, 7% in sensitivity, 5% in specificity and 7% in AUC) with the addition of domain transfer learning in the training phase. Finally, the performance of this modified inter-MCI case was confirmed as a significant improvement over a standard machine learning approach such as the classical support vector machine (SVM) classifier (p = 2.5762 x 10-8) applied on the same training/testing cross-validation folds. In this specific analysis, for estimating the performance of the SVM classifier, the classical univariate feature selection procedure using F-test (ANOVA) was implemented for dimension reduction following which the optimal value of the penalty (cost) parameter in the linear SVM was estimated. The boxplots for the accuracies for the different cross-validation folds using the Resnet and SVM models are shown in Figure 6-8C.
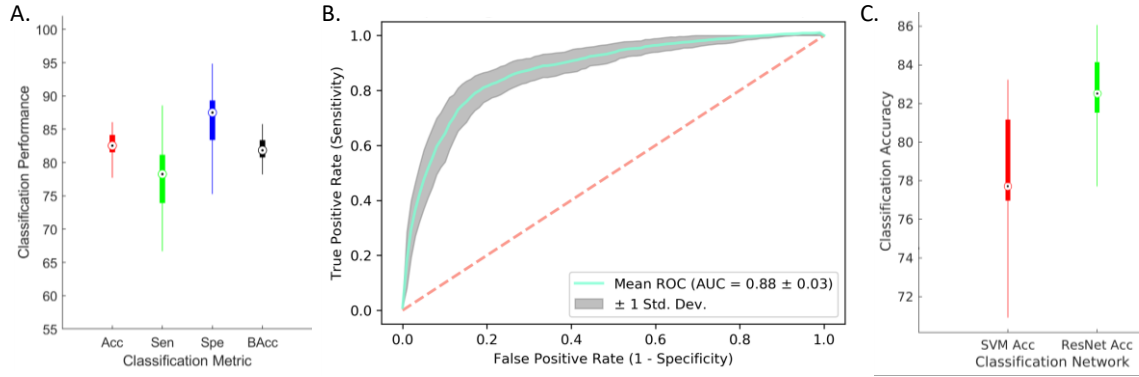
Figure 6-8: Mixed-Class Prognosis Classification. A modified form of repeated (n = 10), stratified 5-fold cross-validation procedure was conducted to evaluate the separability of the two MCI sub-classes. Hypothesizing an improvement with an increase in amount of training data provided by other classes (analogous to domain transfer learning), the learner was trained with all datasets from the CN and AD classes (or domains) in addition to the cross-validation-fold-respective training sMCI/pMCI datasets followed by testing on the cross-validation-fold-respective testing sMCI/pMCI datasets. (A) and (B) A significant improvement for all studied classification metrics (6% in accuracy, 7% in sensitivity, 5% in specificity and 7% in AUC) was observed for this mixed-class classification task as compared to the standard inter-MCI class classification task (i.e. sMCI vs. pMCI classification task as shown in Figure 6-6 and bottom left panel in Figure 6-7). (C) The mixed-class classification task reported a significant performance improvement over the classical SVM model with a p-value of 2.5762e-8.

6.3.2.3 Comparison with previous literature

In this section, we compare the prediction performance of AD progression in our study (modified inter-MCI task) to previous deep learning work in recent literature (Table 6-2). In order to identify previous studies that used deep learning on neuroimaging data to study psychiatric or neurological disorders, we conducted a search on PubMed (May 25, 2018) using search terms very similar to a recent review (Vieira, Pinaya et al. 2017). Specifically, the following search terms were used: ("deep learning" OR "deep architecture" OR "artificial neural network" OR "autoencoder" OR "convolutional neural network" OR "deep belief network") AND (neurology OR neurological OR psychiatry OR

psychiatric OR diagnosis OR prediction OR prognosis OR outcome) AND (neuroimaging OR MRI OR "magnetic resonance imaging" OR "fMRI" OR "functional magnetic resonance imaging" OR PET OR "positron emission tomography"). Following this, we manually screened these articles to identify the relevant subset of studies that applied deep learning to study MCI to AD progression.

A comparison of prediction using MRI data only confirms the superior performance of our method as compared to other undertaken approaches. Using just MRI data, the prediction accuracy obtained in our study (82.7%) is more than 7% greater than the second best performer (using MRI data only) that used a multiscale deep NN in a very recent study (Lu, Popuri et al. 2018). Considering use of multiple modalities, only Suk, Lee et al. (2015) (83.3% using MRI, PET and CSF modalities) and Lu, Popuri et al. (2018) (82.93% using MRI and PET) report slightly higher performance as compared to our study.

Interestingly, despite using multiple modalities, the methods used in these two particular studies report only marginal improvements (0.6% and 0.2% respectively) over our unimodal analysis. Working with multiple modalities generally enhances the prediction performance (variably from 3% to greater than 20% in studies included in Table 6-2), so it would be reasonable to expect further improvement in prediction performance through our method if complimentary information from an additional modality is leveraged. Table 6-2 lists the details of the comparison of sample sizes, machine learning architecture, MCI to AD conversion period, cross-validation parameters, studied modalities and performance of MCI to AD prediction accuracy for these studies.

Table 6-2: Comparison of MCI to AD prediction accuracy using ADNI dataset.

Study	Sample Size	Conversion Period	Architecture	Cross-validation	Accuracy (%)
This work	CN = 237 sMCI = 245 pMCI = 189 AD = 157	36 months	Residual Neural Network	Repeated (n = 10) Stratified 5-Fold	82.7 (MRI)
Suk, Lee et al. (2015)	CN = 52 sMCI = 56 pMCI = 43 AD = 51	18 Months	Stacked Auto-Encoder	Repeated (n = 10) 10-Fold	69.3 (MRI) 83.3 (MRI+PET+CSF)
Suk, Lee et al. (2015)	CN = 52 sMCI = 56 pMCI = 43 AD = 51	18 Months	Deep sparse multi-task learning	Repeated (n = 10) 10-Fold	69.8 (MRI) 74.2 (MRI+PET)
	CN = 229 sMCI = 236 pMCI = 167 AD = 198	18 Months	Deep sparse multi-task learning	Repeated (n = 10) 10-Fold	73.9 (MRI)
Li, Tran et al. (2015)	CN = 52 sMCI = 56 pMCI = 43 AD = 51	18 Months	Multi-layer perceptron	Repeated (n = 10) 10-Fold	57.4 (MRI+PET+CSF)
Suk and Shen (2013)	CN = 52 sMCI = 56 pMCI = 43 AD = 51	18 Months	Stacked Auto-Encoder + Multi-task learning	Repeated (n = 10) 10-Fold	55 (MRI) 75.8 (MRI+PET+CSF +SCORES)
Suk, Lee et al. (2017)	CN = 186 sMCI = 167 pMCI = 226 AD = 226	18 Months	Multi-Output Linear Regression + Deep Convolution Neural Network (CNN)	Repeated (n = 10) 10-Fold	73.28 (MRI+SCORES)
	-- Same --		Joint Linear and Logistic Regression + Deep CNN	Repeated (n = 10) 10-Fold	74.82 (MRI+SCORES)
Shi, Zheng et al. (2018)	CN = 52 sMCI = 56 pMCI = 43 AD = 51	18 Months	Stacked Deep Polynomial Network	Repeated (n = 5) 10-Fold	78.88 (MRI+PET)
Suk, Lee et al. (2014)	CN = 101 sMCI = 128 pMCI = 76 AD = 93	Unmentioned	Deep Boltzmann Machine	10-Fold	72.42 (MRI) 75.92 (MRI+PET)
Lu, Popuri et al. (2018)	CN = 360 sMCI = 409 pMCI = 217 AD = 238	0 to 36 Months	Multiscale Deep Neural Network	10-Fold	75.44 (MRI) 82.93 (MRI+PET)

Furthermore, Moradi, Pepe et al. (2015) (see Table 7 in their manuscript) and Korolev, Symonds et al. (2016) (see Table 3 in their manuscript) did extensive comparisons of other (non-deep-learning) studies and showed their respective approaches to result in better precision than other approaches in previous literature. Moradi, Pepe et al. (2015) studied progression with ADNI data (large sample of 825 subjects) using a regularized logistic regression approach to report classification accuracy of 74% using MRI biomarker only and 82% using their aggregate biomarker that used the patient age and clinical scores as features in addition to the MRI biomarker. Korolev, Symonds et al. (2016) worked with only ADNI-1 MCI subjects (n = 259) to predict progression to AD from MCI using a probabilistic, kernel-based pattern classification approach to report a prediction accuracy of 79.9% using MRI and clinical (cognitive and functional) scores. Our method predicted more accurately (82.7%) using a large sample of 828 subjects (MRI data alone) than these two multimodal, non-deep-learning studies and all studies reviewed in these two studies.

6.3.2.4 Multi-class (4-way) Diagnostic/Prognostic Classification

For the multi-class (4-way) case, the learning framework scored a cross-validated median accuracy of 54% that is higher than recent studies evaluating such a 4-way classification (as reviewed in Table 2 in Vieira, Pinaya et al. (2017)). Although this accuracy level is substantially higher than chance (25%), the appropriateness of the data trends learnt in this relatively much harder classification problem was further confirmed by in-depth ROC and feature projection analyses as discussed next. As an extension of binary ROC analysis, for each class, we estimated a single ROC curve by comparing it to all other classes (i.e. one vs all comparison). ROC curves for the multi-class case can also be estimated by micro-averaging which measures true and false positive rates by

considering each element of each class as a binary prediction, or by macro-averaging which essentially averages over the several class-specific classification metrics. In this analysis, the AD and CN classes reported a higher AUC followed by the micro-averaged and macro-average cases, whereas the pMCI and sMCI classes showed lower AUC (Figure 6-9A).

In the multi-class feature projection analyses (Figure 6-9B and Figure 6-9C), the 512-dimensional features at the output of the first fully-connected layer in the employed learning framework were projected onto a two-dimensional space using the tSNE algorithm (Maaten and Hinton 2008). The tSNE algorithm embeds similar observations as nearby points and non-similar observations as distant points with high probability; so more similar classes could be expected to cluster in vicinity of each other in the projection space. This feature projection analysis was performed to confirm the learning directionality of validated models in our multi-class classification case expecting majority observations for more similar classes being projected/clustered together.

Figure 6-9B demonstrates projections from a sample surrogate model (i.e. model validated for a sample cross-validation fold). Although the classes are not separable in the projection space, yet a clear pattern can be traced easily across the projection spectrum. More specifically, we can observe classes ordered in increasing severity of disease from left to right (i.e. CN, sMCI, pMCI and AD in this specific order) although some outlier observations do exist. The disease severity or the class pattern is further confirmed by coloring the same two-dimensional projections (as in Figure 6-9B) with the six clinical (cognitive and functional) scores (Figure 6-9C). The MMSE and RAVLT clinical scores reveal a clear increase across the spectrum (left through right), whereas the FAQ, CDRSB,

ADAS11 and ADAS13 clinical scores (by nature of score characterization) reveal a clear

decrease across the same spectrum.
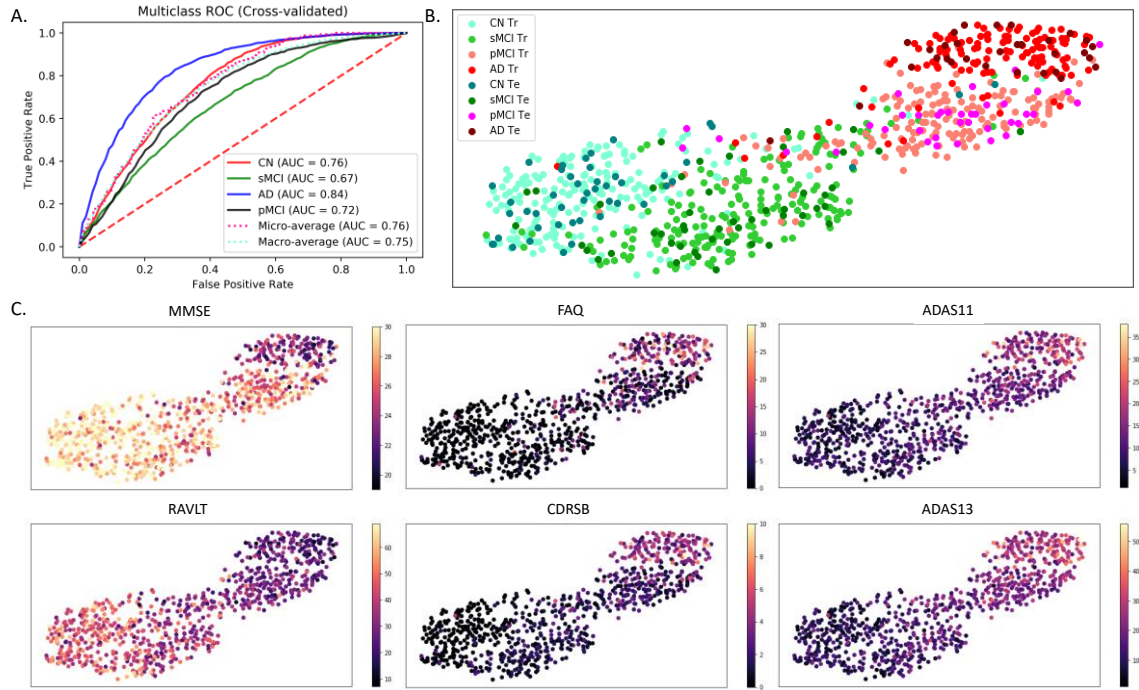
Figure 6-9: Multi-class ROC and Classification Projection Analysis. (A) For the multi-class classification, ROC analysis for each class was performed by comparing observations from that class to all other classes (i.e. one vs all comparison). Additionally, micro-averaged and macro-averaged ROC estimates were computed to find singular performance metrics for multi-class classification. Higher AUC was reported by the AD and CN classes followed by the micro-averaged and macro-average cases, while both MCI classes reported lower AUC. (B) and (C) A feature projection analysis was conducted to confirm appropriateness of the learning directionality in the multi-class classification task. In this analysis, the features at the output of the first fully-connected layer in a sample surrogate multi-class model were projected onto a two-dimensional space using the tSNE algorithm. Barring few outliers, the projections of the observations are appropriately ordered by disease severity in terms of diagnostic label (panel B) and clinical scores (panel C). In panel B, the 'Tr' abbreviation in the figure legend corresponds to the training samples whereas 'Te' corresponds to the test samples. In panel C, the following clinical scores were used: MMSE: Mini-Mental State Exam, FAQ: Functional Activities Questionnaire, CDRSB: Clinical Dementia Rating Sum of Boxes, ADAS: Alzheimer's Disease Assessment Scale, and RAVLT: Rey Auditory Verbal Learning Test.
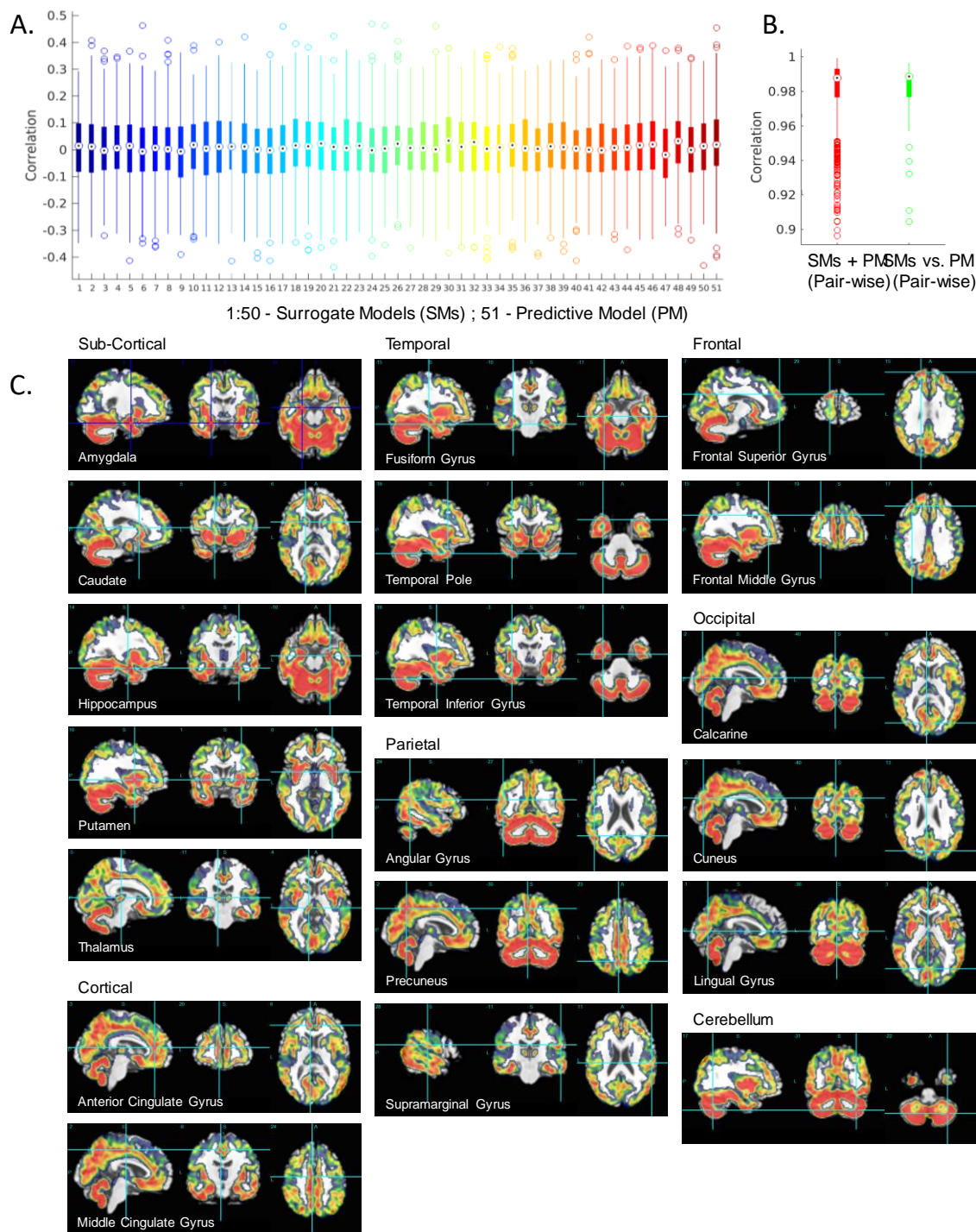
Figure 6-10: (A) The filters for the first convolutional layer were compared in each of the 50 surrogate models (columns 1 to 50 in panel A) as well as the final predictive model (column 51 in panel A) for the modified sMCI vs. pMCI (i.e. mixed-class) classification task. Low pair-wise correlations in the learnt 64 filters in each of these 51 models confirms appropriate learning directionality of the mixed-class framework in the training phase. (B)

The mean activations/features at the output of the first convolution layer (normalized and post non-linear activation) were projected back to the brain space to localize activations contributing most to the classification. The 3D activation maps were compared pairwise-across the 51 models pairwise (correlation boxplot on left in panel B); additionally, the 3D activation maps for the 50 surrogate models were compared to the maps from the final predictive model (correlation boxplot on right in panel B). In both cases, a very high median correlation value was observed thus confirming similar features being extracted across the different models. (C) This panel shows the spatial maps of the brain regions corresponding to the peak activations identified by the final predictive model. Hotter (towards red) color imply higher mean activations, while cooler (towards blue) colors imply lower mean activations. The discriminative brain regions at these peak activations were identified in correspondence to the AAL brain atlas.

6.3.2.5 Model Validation for the Mixed Class (modified inter-MCI) Classification Task

The mixed class (i.e. modified sMCI vs. pMCI) binary classification task was focused on to identify the most discriminative brain regions in early AD. To ensure proper learning in the training phase, additional tests were performed on filter weights and output activations at the first convolutional layer. As in the case of any CNN architecture, similar (i.e. highly correlated) filters almost certainly indicate incorrect convergence of the loss function and thus an inappropriate local minimum. To control for that, we performed a similarity analysis on the weights of the 64 (size 3 x 3 x 3) filters learnt at the first convolution layer as a sanity check. More specifically, the filter weights for each of the channels in the first convolutional layer were compared pair-wise in each of the 50 surrogate models as well as the final predictive model.

The boxplots in columns 1 to 50 in Figure 6-10A show the pair-wise correlations of filter weights for each of the 50 surrogate models, whereas those for the final predictive model are shown in the boxplot in column 51. Since low pair-wise correlations in the learnt 64 filters in each of these 51 models were observed, it can be concluded that the trained model indeed learnt the local minima.

While inference on discriminative brain regions was done from the features of the final predictive models that were trained on all data, ideally, projections of data samples into the representation space estimated by the surrogate models must be similar to confirm similar learning trends and robustness of the extracted features. For this comparison, the final predictive model and the 50 surrogate models for this classification task were compared in the mean activations (across the 64 channels) at the output of the first convolutional layer (batch-normalized and post non-linear activation).

A pairwise similarity (i.e. correlation) comparison of the 3D activation maps across these 51 models is shown on the left in Figure 6-10B, whereas the comparison of the similarity in activation maps for the 50 surrogate models to the activation maps from the final predictive model is shown on the right in the same panel. In both cases, a very high median correlation value was observed thus confirming similar discriminative features extracted across different surrogate models and the final predictive model.

6.3.2.6 Localizing Abnormalities: Discriminative Brain Regions

Peak activations of the identified brain regions which are most discriminative of progression of MCI to AD were localized by projecting the sub-sampled mean activations at the output of the first convolutional layer (batch-normalized and post non-linear activation) back to the brain space. Notably, the activations at the output of the first convolutional layer could be expected to be fine-tuned to small degrees in the deeper layers. However, we restricted our analysis to the first layer since there is a substantial loss of spatial resolution as we go deeper into the networks, and estimating and back-propagating the relative importance of the features at each layer needs dedicated developmental efforts

that are outside the scope of the current work. Hence, we restrict our abnormality localization analysis to features at the output of the first convolutional layer.

The brain regions at the peak activations were identified in correspondence to the AAL brain atlas. Figure 6-10C illustrates the spatial maps at the most activated sagittal, coronal and axial slices as tracked from the final predictive model for the modified sMCI vs. pMCI classification task. In this figure, hotter (towards the red spectrum) colors imply higher mean activations, while cooler (towards the blue spectrum) colors imply lower mean activations. Specifically, peak activations were observed in the sub-cortical regions including hippocampus, amygdala, caudate nucleus, putamen and thalamus, cortical regions including anterior cingulate gyrus and middle cingulate gyrus, temporal regions including fusiform gyrus, temporal pole, and temporal inferior gyrus, frontal superior/middle gyrus, cerebellum, parietal regions including angular gyrus, precuneus and supramarginal gyrus, and occipital regions including calcarine, cuneus and lingual gyrus. In the discussion section, we will discuss these discriminative brain regions in correspondence to several previously reported findings in the AD/MCI literature.

6.3.3 Dataset 2: Comparison of Unimodal and Multimodal Prediction Analyses

A three-way comparison of cross-validated prediction performance from the fMRI features, sMRI features and the fused features was conducted. The mean normalized accuracies for the fMRI, sMRI and multimodal prediction were 0.70, 0.75 and 0.78 respectively. Results evince that the prediction performance with the multimodal fused features significantly outperform ($p < 0.005$) that from either of the unimodal classification analyses as shown in Figure 6-11. Additionally, the sMRI modality significantly

outperformed the fMRI modality (p < 0.005). However, the improvement of multimodal prediction over that from the sMRI features corroborates the additional diagnostic information provided by the fMRI features derived from time-varying FC analyses.
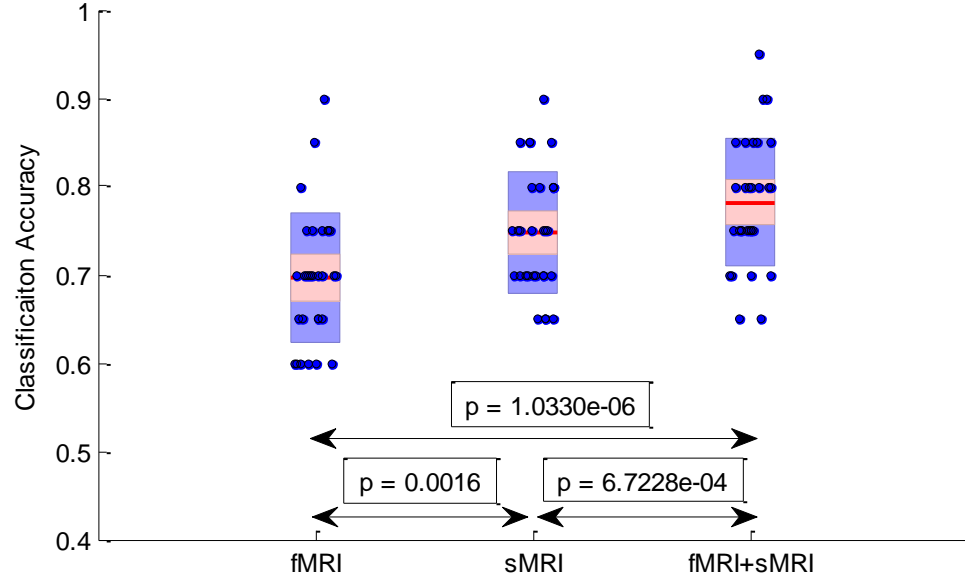
Figure 6-11: A comparison of accuracies from the two unimodal and multimodal prediction analyses. Multimodal prediction performance was found to be significantly better than the performance from the unimodal prediction analyses. The mean normalized accuracies for the fMRI, sMRI and multimodal prediction were 0.70, 0.75 and 0.78 respectively. A comparison of the cross-validation accuracies demonstrated significant differences (p < 0.005) between all three groups, with the p-values increasing the following order: fMRI vs. sMRI, sMRI vs. fMRI+sMRI, and fMRI vs. fMRI+sMRI.

6.4 Discussion

In this work, we extensively test the ability of the ResNets to learn abstract neuroanatomical alterations in sMRI data. The tested deep learning architecture provided close to the state of the art prognostic classification performance following which we focused on the inter-MCI classification task to predict the MCI sub-group who would progress to AD within three years. The principle progression analysis of our work is the

mixed-class (i.e. modified) inter-MCI classification task where we used principles of domain transfer learning (additionally training with data from other domains). This analysis bears high clinical relevance. Importantly, on the MRI data alone we achieved classification accuracy of 82.7% which is a significant improvement over state of the art with either MRI based (75.44% as reported in Lu, Popuri et al. (2018)) and very close to state of the art performance with multimodal results (83.3% as reported in Suk, Lee et al. (2015)). The accuracy in this modified inter-MCI class classification task is significantly higher than that in the standard inter-MCI case which suggests the performance improvement was also enabled by additional training information acquired from other (AD and CN) domains.

Furthermore, the learning directionality and trends were verified in the multiclass case by projecting the features at output of the first fully-connected layer onto a two-dimensional surface. The projection/clustering class sequence in Figure 6-9B and Figure 6-9C support the appropriateness of the extracted features and their association with the clinical scores, thus confirming the high learning capacity and potential of this deep architecture. The learning directionality and trends were further validated by additionally testing for similarity in the filter weights and activations at the first convolutional layer (Figure 6-10A and Figure 6-10B) for the different surrogate models and the final predictive model. Notably, the reported performance metrics were obtained from a large dataset (n = 828), a rigorous cross-validation procedure featuring 10 repeats and a sufficiently large (20%) test size in each of the folds (i.e. a total number of 50 large-sized stratified folds). These results evince that the ResNets can be considered well-suited to neuroimaging data and future studies to uncover further potential of such or similar architectures must be

undertaken. Additionally, a high level of conformance Next, we discuss the discriminative brain regions suggested by the ResNet in context to previous findings in literature.

AD is characterized by serious trouble in performing familiar tasks, solving problems, planning, reasoning, judgement and thinking, and generally features increased confusion and discomfort in speech, vision, reading, focusing, and spatial or temporal perception. Struggling with these symptoms, the person undergoes mood and personality changes and increasingly loses interest in favorite activities and social life. A sizable amount of previous work has related the above mentioned cognitive, behavioral and emotional phenomenon to specific structural changes in the brain, which we discuss next in context to the discriminative brain regions identified by the ResNet framework.

The hippocampus and amygdala subcortical regions in the medial temporal lobe have been consistently reported as most prominent discriminative regions in early AD. Hippocampus is strongly related to memory formation and recall, and recent evidence suggests more pronounced hippocampal atrophy in the progressive MCI class (Braak and Braak 1991, Visser, Verhey et al. 2002, Devanand, Pradhaban et al. 2007, Burton, Barber et al. 2009, Kantarci, Weigand et al. 2009, Risacher, Saykin et al. 2009, Walhovd, Fjell et al. 2010, Costafreda, Dinov et al. 2011). Similarly, structural changes in amygdala, a brain region mainly responsible for emotional experiences and expressions, have been related to personality changes, for example, increased irritability and anxiety, in AD (Unger, Lapham et al. 1991, Whitwell, Shiung et al. 2008, Poulin, Dautoff et al. 2011). Other highly activated subcortical regions included thalamus and the dorsal striatum (putamen and caudate). While the main function of thalamus is to relay motor and sensory signals to the cerebral cortex, and regulate consciousness and sleep, the dorsal striatum is believed to

contribute directly to decision-making subjective to desired goals. Observed aberrations in the dorsal striatum (putamen and caudate) and thalamus regions are typical of subjects with AD (Braak and Braak 1991, De Jong, Van Der Hiele et al. 2008, Jiji, Smitha et al. 2013, Cho, Kim et al. 2014, Aggleton, Pralus et al. 2016) with impairments in the thalamus in AD associated to deteriorating consciousness, bodily movement and coordination, attentional, and motivation levels and impairments in the dorsal striatum associated to very slow or absent decision-making abilities.

Apart from the above widely studied and highly discriminative medial temporal lobe, we also report peak activations in the fusiform gyrus, inferior temporal gyrus and temporal pole regions on the temporal lobe. These regions have been known to be associated with pattern (e.g. face, body, object, word, color, etc.) recognition and reported to be affected by AD in a few previous studies (Chan, Fox et al. 2001, Galton, Patterson et al. 2011). In the frontal lobe, peak activations were observed in the superior and middle frontal gyrus. These regions are also associated with decision making and problem solving, reportedly highly damaged in AD (Johnson, Jahng et al. 2005, Whitwell, Shiung et al. 2008, Sluimer, Van Der Flier et al. 2009) and are believed to lead to higher lethargy levels, bizarre/inappropriate behavior and situations of being stuck in a certain condition (repeating same things over and over again).

Besides the above discussed frontotemporal networks, AD is characterized by decline in important parietal networks such as precuneus (Scahill, Schott et al. 2002, Apostolova and Thompson 2008, Whitwell, Shiung et al. 2008, Fennema-Notestine, Hagler et al. 2009, Walhovd, Fjell et al. 2010, Bailly, Destrieux et al. 2015), and the angular and supramarginal gyrus regions (Walhovd, Fjell et al. 2010, Yun, Kwak et al. 2015). Cerebellum, a critical

brain region in several motor, cognitive and behavioral functions, in also more recently being increasingly suggested as a direct contributor to cognitive and neuropsychiatric deficits in AD (Guo, Tan et al. 2016, Schmahmann 2016, Jacobs, Hopkins et al. 2017) with deteriorating cerebellum health resulting in several symptoms such as lack of balance and coordination, tremors, slurred speech and abnormal eye movements in the elderly.

Cortical regions including anterior cingulate gyrus and middle cingulate gyrus that are primarily responsible for higher cognitive (i.e. decision-making) and emotional (e.g. social interactions, empathy, etc.) processes have also been suggested to be highly vulnerable in AD (Killiany, Gomez-Isla et al. 2000, Huang, Wahlund et al. 2002, Scahill, Schott et al. 2002, Jones, Barnes et al. 2006, Fennema-Notestine, Hagler et al. 2009, Bailly, Destrieux et al. 2015). Finally, damages to the occipital lobe are associated with increased misinterpretations of the surrounding environment (e.g. hallucinations, illusions, misidentification, misperceptions, etc.) and occipital regions comprising the calcarine, cuneus and lingual gyrus regions have indeed been reported to be compromised in progression to AD.

The above discussed findings add further evidence that the localized abnormal patterns in the brain structure could play a significant role in prediction of early AD biomarkers and are of potential clinical application. In fact, a few of the discriminative regions that we report are rarely used as prognostic biomarkers to study conversion of MCI to AD; our work and the citied literature in this discussion provide a compelling evidence of including these additional biomarkers to allow for a complete characterization of the structural changes in AD progression.

Finally, the three-way comparison of prediction performance from the fMRI, sMRI and the fused (fMRI + sMRI) features confirmed superior prediction performance through the fused features as compared to the unimodal features. This analysis also reported a significantly superior prediction performance using the non-linear sMRI features than the time-varying FC based fMRI features. Evidently, a significant improvement in the prediction accuracy from the fused feature space over the sMRI features validates the presence of complimentary diagnostic information available in the fMRI features. These observations indicate the benefits of using multimodal fusion, deep learning to extract non-linear sMRI features and time-varying FC approaches for estimating discriminative fMRI features.

6.4.1 Limitations and future scope

Here we note some basic limitations of our work that could be addressed in the future depending on algorithmic computational tractability, and availability of data resources and data processing algorithms. As with other neuroimaging studies, the foremost limitation is a limited training data size. In generic image processing applications, this limitation is often addressed with data augmentation procedures by using simple rotation, translation, scaling and other data transformations (also see (Castro, Ulloa et al. 2015, Ulloa, Plis et al. 2015) for more elaborate data augmentation examples with structural MRI). We expect even further increases in performance with employing such techniques in the future work. This broadens perspectives for our models that are already performing at or above the state of the art.

Interestingly, a recent study (Casanova, Hsu et al. 2012) demonstrated an increase in classification performance with increase in sample size using ADNI sMRI data. Similarly, in our work as well, we saw a substantial increase in performance with more training data being fed to the ResNet framework in the modified inter-MCI class classification task as compared to the standard inter-MCI class classification task. This makes a compelling case to test use of multiple datasets to extract features in a pooled or separate fashion, and then use the pooled or separate information to train the machine learning framework. With increasing data availability and standardization in data preprocessing and pooling procedures, further substantial improvement in diagnostic and/or prognostic classification performance could be expected in future multi-study deep learning research efforts.

Due to the computationally expensive nature of training deep CNNs, few limitations regarding computational tractability within realistic study time remain. This tends to restrict extensive fine-tuning of each involved hyperparameter through random or grid search analysis on multiple hyperparameters and additionally backing up statistical trends using methods such as Monte-Carlo. As such, the most important hyperparameters must be prioritized and optimized to estimate generic performance trends of the algorithm within the realistic study period. For this specific work, we optimized the initial learning rate and L2 weight decay parameter on a sample cross-validation fold using extensive grid analysis and retained the values for other dataset partitions. Although the same hyperparameters would likely achieve close to actual performance on other data folds, yet this fine-tuning could have a small effect on the performance of the respective surrogate models (e.g. reported performance metrics could be slightly lower than the original) but

also on that of the final predictive model. It must be noted that this limitation is for performance quantification only; it is least likely to affect the qualitative analysis (e.g. localizing discriminative brain regions) by a significant margin.

Choosing stopping criterion for learning a classifier typically involves a tradeoff between generalization error and learning time. While this study approximated the stopping criterion with information across all cross-validation folds, further detailed introspection using relatively unestablished but promising variants of early stopping criterion could be explored in future investigations (Prechelt 1998). Similarly, effect of algorithmic variations in bottleneck residual block structures (size and depth), training time, and loss optimization procedures could be understood in future studies to further enhance the prediction performance. Finally, while we focus on activations at the output of the first convolutional layer, we could expect sequential fine-tuning of such activations as we move down in the architecture. This however happens at the cost of substantial loss of spatial resolution. Independent frameworks are now being proposed to study multi-layer relevance propagation (Bach, Binder et al. 2015, Lapuschkin, Binder et al. 2016) in 2D image processing applications using deep CNN or ResNet frameworks. In fact, multi-layer relevance propagation is currently an independent, rich research topic as it is equally important to understand/interpret the predictions as predicting itself, and even more so in medical applications. However, interpreting these deep non-linear models and optimally representing extracted features is not trivial. In absence of a framework to allow for fine-tuned optimal representations of the features/activations in the used architecture, we restricted our analysis to the activations at the first convolutional layer as these representations could be considered as a good representation of the discriminative features

that are further fine-tuned to small degrees at each layer. Nonetheless, it would be interesting to explore any significant activation changes with more deep relevance propagation frameworks once they become available.

Several other approaches for enhancing predictive performance of AD progression could be explored in future work. Diagnosis for the subjects is currently established through clinical scores but diagnosis-specific neuroanatomical or neurofunctional abnormalities might actually not show in each subject in each class due to the heterogeneous nature of age-related dementia. In such a scenario, it could be interesting to constrain this heterogeneity by training the machine learning model on the most homogeneous samples (i.e. samples most representative of the given class) and then evaluate change in the performance of the diagnostic/prognostic classification or change in the feature space of interest. Another approach could be to fuse the low-dimensional clinical scores used to make the clinical diagnosis with the MRI features to further enrich feature learning process. This approach has reportedly resulted in enhanced performance in few studies as also suggested in Table 6-2. Other widely used low dimensional features chosen by experts (e.g. volumetric MRI features or similar features from other modalities) could also further enhance diagnostic/prognostic performance.

Chapter 7: Summary of the Dissertation and Future Research Directions

This doctoral dissertation proposes approaches to investigate robustness and statistical significance, and disease characterization and prediction utilities of time-varying FC state profiles of the human brain at rest. The building blocks of the novel approaches framed in this dissertation leveraged several advanced signal processing and machine learning tools including spatial ICA, temporal ICA, PCA, k-means clustering, tSNE, joint ICA, CCA, multiset CCA, ResNet, linear regression, and linear SVM. These concepts were pipelined in an integrative manner to probe robustness and statistical significance of the time-varying FC state profiles in Chapters 3 and 4, propose a blind source separation based multimodal data fusion framework for disease characterization in Chapter 5, and a deep learning based multimodal data fusion for prediction progression to disease in Chapter 6.

In the following sections, we summarize the major aspects and contributions of this dissertation and propose possible research directions that can be pursued going forward.

7.1 Summary of the Dissertation

In Chapters 3 and 4 of this dissertation, we employed the hard-clustering and fuzzy meta-state chronnectomic approaches to estimate time-varying FC state profiles in numerous, large independent partitions of a huge fMRI dataset. This mega-analysis reported high levels of replicability in the time-varying FC state profiles and corroborated the statistical significance of the associated FC state summary measures. We also found

that the time-varying FC state profiles were robust against variation in data quality, analysis, grouping, and decomposition methods.

In Chapter 5 of this dissertation, we proposed a novel blind-source separation based multimodal fusion framework to characterize schizophrenia by highlighting disrupted links in gray matter and FC strengths in brain connections in schizophrenia. Using the multivariate symmetric fusion approach of mCCA+jICA, we were able to identify two joint sources with significantly co-varying and group difference exhibiting gray matter and time-varying FC components that revealed disrupted links in schizophrenia. We discuss how results from this disease characterization framework conform to previously reported findings on gray matter and FC aberrations in Schizophrenia, the new findings reported in this study and ways to interpret results from this framework going forward. We suggest that studying such interactions can provide a useful way of evaluating structure-function relationships and characterizing schizophrenia or other brain conditions.

In chapter 6 of this dissertation, we proposed a novel multimodal framework based on deep learning of sMRI features and time-varying FC based fMRI features to predict progression of people with MCI to AD. The work undertaken in this chapter was aimed at testing the presence of any additional disease predictive value of the time-varying FC features and also exploring how multimodal frameworks based on deep learning and making use of time-varying FC based fMRI features can be extended to diagnosis and prediction of diseased brain conditions through neuroimaging data. Using a big sMRI dataset, we predicted the subset of MCI subjects that would progress to AD. This sMRI analysis reported better than state-of-the-art performance and boosted our confidence to use the extracted non-linear features in a multimodal framework to further boost the

prediction performance. Hence, the non-linear sMRI features extracted with the deep learning method were fused with the time-varying FC based fMRI features using CCA to estimate the multimodal prediction performance. Our preliminary, rigorously cross-validated results suggest a significant performance improvement with prediction from the fused (multimodal) feature space as compared to the individual (unimodal) feature spaces, thus highlighting the additional diagnostic information provided by use of fMRI features based on time-varying FC state profiles.

In summary, the approaches developed and tested in this dissertation evince high levels of robustness and highlight the utility of time-varying FC state profiles as potential biomarkers to characterize, diagnose and predict diseased brain conditions. The findings in this work argue in favor of the view of FC investigations of the brain that are centered on time-varying FC approaches, and additionally highlight the benefits of combining multiple neuroimaging data modalities via data fusion.

7.2 Future Research Directions

As discussed in the previous section, taken together, the findings from the work accomplished in this dissertation assume high significance in future studies on time-varying FC estimation and multimodal data fusion approaches in the neuroimaging literature. However, there are various interesting research directions and extensions to the proposed approaches that could be pursued in future as we discuss in the concluding part of this dissertation.

In this work, we evaluate robustness of two chronnectomic, time-varying FC estimation approaches, both based on estimation of temporal correlations using the sliding

window method. An important extension to the current replicability discussion could be to evaluate and compare robustness of several other commonly used time-varying approaches based on time-series correlations, dynamic conditional correlations, phase synchronization, time-frequency coherence and graph theory. Statistical significance of measures from these approaches could be tested and compared in the similar fashion. Furthermore, while we confirm replicability in the whole-brain patterns, we can dig a level deeper by attempting identification of specific brain connections that appear more robustly dynamic across independent groups, for example, by using the approach proposed in Zalesky, Fornito et al. (2014) and tested in Abrol, Damaraju et al. (2017). Finally, robustness of time-varying FC based measures could be studied in different homogeneous diagnostic groups and compared with similar measures from healthy controls for extensive validation of similarities and differences in FC.

Going forward, investigating the functional and neurophysiological relevance of the observed time-varying FC states, meta-states or other robust connectivity descriptors assumes critical importance and needs further confirmation. Demonstrating functional relevance is currently an active topic with several interesting works establishing direct links with ongoing cognitive function and effective cognitive performance (Craddock, James et al. 2012, Schaefer, Margulies et al. 2014, Gonzalez-Castillo, Hoy et al. 2015, Madhyastha, Askren et al. 2015, Shine, Bissett et al. 2016, Shine, Koyejo et al. 2016), identifying signatures of consciousness (Hutchison, Womelsdorf et al. 2013, Amico, Gomez et al. 2014, Hudson, Calderon et al. 2014, Barttfeld, Uhrig et al. 2015, Wang, Ong et al. 2016) , tracking day-dreaming/mind-wandering (Kucyi and Davis 2014, Kucyi 2017), and decoding signatures of sleep and awake states (Tagliazucchi and Laufs 2014). Additionally,

simultaneous recording of electrophysiological data in conjunction with BOLD fMRI data not only enables charting of the human brain activity at high spatial as well as high temporal resolutions, but also linking variability in FC fluctuations to external measures of neuronal activity. Recently found evidence of potential electrophysiological signatures of dynamic BOLD FC clearly hint fluctuations in the BOLD FC to be interesting i.e. having a neurophysiological origin (Tagliazucchi, von Wegner et al. 2012, Chang, Liu et al. 2013, Allen, Damaraju et al. 2017). Such preliminary observations clearly suggest that multi-modal studies may play a key role in determining neural or behavioral relevance of the observed FC states in the fMRI data. Future work would hence likely involve recognition of a multi-modal, multi-level theoretical framework that would very likely be able to capture the underlying physiological correspondences that enable switching of the established FC patterns.

Neuronal correlates of time-varying FC have been previously suggested in few studies (Liu, Chang et al. 2013, Thompson, Merritt et al. 2013, Kragel, Knodt et al. 2016), and more recently Matsui, Murakami et al. (2017) claims a link between time-varying FC and neuronal origins, however, a lot of additional work is still needed to affirm the correspondence of the time-varying FC state descriptions with underlying neuronal activity. Other lesser explored alternate approaches that have shown promise include casual manipulation of the FC states using pharmacology (Hutchison, Womelsdorf et al. 2013, Barttfeld, Uhrig et al. 2015, van den Brink, Pfeffer et al. 2016) or direct brain simulation techniques (Liu, Lee et al. 2015, Cocchi, Sale et al. 2016) to trace functional or neurophysiological relevance (Shine and Poldrack). We predict such tailored investigations probing the functional and neurophysiological relevance of the time-varying FC states will

play a major part in uncovering the underlying relationships we are pursuing; confirmation of replicability and statistical significance could thus be regarded as an initial step forward.

Future inferences from the disease characterization multimodal framework employed in Chapter 5 of this work could be further tested on multiple multimodal datasets featuring the studied diagnostic group. We anticipate that similar methods could be easily extended to the study of other brain conditions; likewise, different feature spaces, combinations of neuroimaging modalities and algorithms could be evaluated in the proposed fashion. Other potential factors such as subject's consciousness, anxiety levels in the scanner and disease risk levels could be investigated in future studies, for a fuller interpretation of the results.

Finally, the deep learning based multimodal disease prediction framework proposed in Chapter 6 of the dissertation could be improvised to make use of an end to end multimodal fusion approach that uses the same network to train data (raw or preprocessed) or features from all modalities. This unified framework would likely enable better tuning and optimization of network weights as compared to the unimodal training case as implemented in the current work. Furthermore, an extensive comparison across several other deep learning approaches could be conducted to identify the framework most suited for diagnostic classification and prediction applications using neuroimaging data. Also, while, in this study, we test this framework to study and predict progression to Alzheimer's disease (AD), application of this framework to study other diseases would be straightforward.

APPENDIX A

A.1 Resting State Networks

RSN REGIONS	BA	vol_cmm	max_act	peak_act (mm)		
				x	y	z
Subcorticial Networks						
Basal Ganglia (IC 33)	34	20925	34.39	-24	6	-3
Thalamus (IC 58)		20142	47.91	6	-12	15
Temporal Networks						
Superior Temporal Gyrus (IC 62)	42	73845	30.36	60	-21	9
Middle Temporal Gyrus (IC 75)	39	1108	23.07	-54	72	9
Transverse Temporal Gyrus (IC 94)	13	4563	20.52	45	-3	3
Somatomotor Networks						
Pre-Supplementary Motor Area (IC 18)	32	37098	35.53	0	6	45
Supplementary Motor Area (IC 36)	6	51057	63.2	0	9	72
Bi Paracentral Lobule (IC 49)		39852	108.21	0	-12	81
Left Precentral Gyrus (IC 54)	4	52704	44.68	-39	-24	66
Right Precentral Gyrus (IC 59)	4	47466	47.87	42	-24	66
Bi Postcentral Gyrus (IC 72)	6	68931	30.55	18	-24	72
Right Postcentral Gyrus (IC 74)	4	65151	45.37	60	-6	27
Postcentrala Gyrus (IC 99)		30996	72.81	18	-30	84
Default Mode Networks						
Bi Posterior Cingulate Cortex (IC 6)	23	39663	64.95	0	-54	15
Right Angular Gyrus (IC 12)	40	7047	31.91	54	-60	36
Bi Precuneus (1) (IC 30)	7	59751	40.33	0	-51	54
Precuneus (2) (IC 34)	7	44334	44.56	0	-60	36
Left Angular Gyrus (IC 42)	39	13851	30.33	-51	-60	33
Precuneus (3) (IC 84)	7	41634	64.82	0	-78	45
Anterior Cingulate Cortex (IC 90)	10	17577	46.37	0	51	0
Visual Networks						
Lingual Gyrus (IC 17)	30	47358	27.52	21	-51	0
Calcarine Gyrus (IC 25)	31	55836	33.08	3	-72	15
Cuneus Gyrus (IC 98)	19	58050	44.82	3	-93	30
Cognitive Control Netwoks						
Left Inferior Parietal Lobule (IC 1)	7	49005	34.1	-30	-81	45
Left Superior Parietal Lobule (IC 24)	10	486	7.9	-33	-66	54
Right Inferior Parietal Lobule (IC 37)	40	47412	29.13	54	-36	54
Bi Superior Parietal Lobule (IC 55)	7	56214	39.59	-24	-60	66
Right Superior Parietal Lobule (IC 92)	7	47142	36.23	36	-63	54
Frontal Networks						
Superior Medial Gyrus (1) (IC 10)	8	43119	55.58	0	48	51
Inferior Frontal Gyrus (IC 31)	47	45009	35.5	-42	18	-6
Medial Frontal Gyrus (IC 39)	9	14715	26.55	0	48	27
Left Superior Frontal Gyrus (IC 47)	10	6939	40.75	-33	60	6
Right Superior Frontal Gyrus (IC 85)	10	11016	43.73	30	63	3
Superior Medial Gyrus (2) (IC 89)	10	49437	49.62	0	66	21
Superior Frontal Gyrus (IC 100)	6	55971	69.81	3	27	66
Cerebellar Networks						
Bi Cerebellum (IC 8)		8559	33.68	0	-60	-18
Right Cerebellum (IC 26)		21465	26.93	39	-42	-45

Appendix A – Table 1: Resting State Networks (RSNs). Broadmann areas (BA), activation cluster volumes (vol_cmm), peak activation intensities (max_act) and peak activation coordinates (peak_act) corresponding to the RSN spatial maps.

A.2 Evaluation of time-resolved connectivity with the CPR null model

In this analysis, we considered the consistent phase randomized (CPR) null model (used in Hindriks, Adhikari et al. (2016) to evaluate time-resolved dFC using a linear and a non-linear test statistic as also tested using auto-regressive surrogate data in Zalesky, Fornito et al. (2014) and amplitude-adjusted phase randomized models in Betzel, Fukushima et al. (2016). Similar evidence as in Zalesky, Fornito et al. (2014) and Betzel, Fukushima et al. (2016) for presence of "dynamic" inter-regional connections that rejected this null model after FDR correction was found. More specifically, alike Hindriks, Adhikari et al. (2016) and following Zalesky, Fornito et al. (2014), we estimated the standard deviation across the time (i.e. window) dimension of the windowed FNC data (as the linear test statistic) and the same non-linear statistic as used in Zalesky, Fornito et al. (2014) for all subjects in a group. These test statistics could be considered as the extent of time-varying fluctuations in the correlation coefficients. For each subject, for each ROI-pair (referred to as a "connection" in the original work), a null distribution of these test statistics was estimated, and the connections that rejected the null hypothesis were retained for further analysis. For each subject, binary graphs highlighting only the top-10 most "dynamic" connections (approximately 1.5% of total number of connections as in Zalesky, Fornito et al. (2014)) were constructed and the degree of each region in these graphs was evaluated. This degree was summed across the subjects to frame an index of consistency of these dynamic connections (i.e. how consistently the regions were dynamic across the subjects). The regionally sorted versions of this index for the real and 1000 surrogate datasets are presented in SI Figure 1 below. Similar to Zalesky, Fornito et al. (2014), the vertical lines represent the FDR corrected p-values with a cut-off of 0.05; therefore, the

regions to the right of these vertical lines could be considered dynamic more consistently than that would be expected by chance alone. For the first group, the consistent regions were all but one (10 out of 11) found to be the same for both test statistics. Despite this preliminary evidence of dynamic nature of the inter-regional connections as conveyed by use of the CPR null model, results from use of this null model must be interpreted with caution, especially if they are to be used as evidence for or against non-stationary nature of the fMRI data, since the level to which this null model disrupts the relevant dynamics in the data is yet not clear (as it has yet not been framed mathematically or reviewed in detail in previous literature).
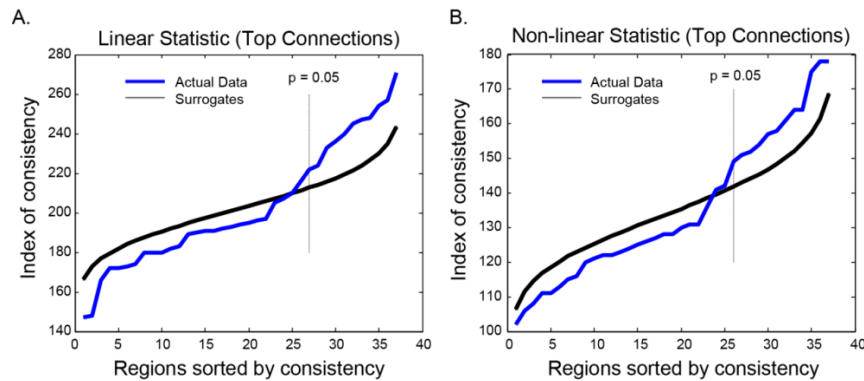
Appendix A – SI Figure 1: Evaluation of regions most consistently forming dynamic connections using an approach similar to Zalesky, Fornito et al. (2014). The plots show the regionally sorted index of consistency for real data (in blue) and mean of the index of consistency of the 1000 surrogate datasets (also regionally sorted) with the error bars (in black) for (A) the linear test statistic; and (B) the non-linear test statistic. The regions to the right of the $p = 0.05$ cutoff could be considered dynamic more consistently than that would be expected by chance alone.

References

Abou-Elseoud, A., T. Starck, J. Remes, J. Nikkinen, O. Tervonen and V. Kiviniemi (2010). "The effect of model order selection in group PICA." Hum Brain Mapp **31**(8): 1207-1216.

Abrol, A., M. Bhattarai, A. Federov, Y. Du, S. Plis and V. D. Calhoun (2018). "Deep Residual Learning for Neuroimaging: An application to Predict Progression to Alzheimer's Disease." Under Review.

Abrol, A., C. Chaze, E. Damaraju and V. D. Calhoun (2016). The chronnectome: Evaluating replicability of dynamic connectivity patterns in 7500 resting fMRI datasets. 2016 38th Annual International Conference of the IEEE Engineering in Medicine and Biology Society (EMBC).

Abrol, A., E. Damaraju, R. L. Miller, J. M. Stephen, E. D. Claus, A. R. Mayer and V. D. Calhoun (2017). "Replicability of time-varying connectivity patterns in large resting state fMRI samples." NeuroImage **163**.

Abrol, A., Z. Fu and V. D. Calhoun (2018). "Multimodal Data Fusion Enhances Prediction of Progression from Mild Cognitive Impairment to Alzheimer's Disease." In Preparation.

Abrol, A., B. Rashid, S. Rachakonda, E. Damaraju and V. D. Calhoun (2017). "Schizophrenia shows disrupted links between brain volume and dynamic functional connectivity." Frontiers in Neuroscience **11**.

Abrol, A., H. Rokham and V. D. Calhoun (2018). "Diagnostic and Prognostic Classification of Brain Disorders Using Deep Residual Learning on Structural MRI Data. ." Under Review

ADNI. "ADNI MRI Protocols." Retrieved 2017, from http://adni.loni.usc.edu/methods/documents/mri-protocols.

Aggleton, J. P., A. Pralus, A. J. D. Nelson and M. Hornberger (2016). Thalamic pathology and memory loss in early Alzheimer's disease: Moving the focus from the medial temporal lobe to Papez circuit. Brain. **139:** 1877-1890.

References

Alexander-Bloch, A., J. N. Giedd and E. Bullmore (2013). "Imaging structural co-variance between human brain regions." Nat Rev Neurosci **14**(5): 322-336.

Allen, E. and V. D. Calhoun (2012). "Extracting intrinsic functional networks with feature-based group independent component analysis." Proc. HBM, Beijing, China.

Allen, E. A., E. Damaraju, T. Eichele, L. Wu and V. D. Calhoun (2017). "EEG Signatures of Dynamic Functional Network Connectivity States." Brain Topography: 1-16.

Allen, E. A., E. Damaraju, S. M. Plis, E. B. Erhardt, T. Eichele and V. D. Calhoun (2012). "Tracking Whole-Brain Connectivity Dynamics in the Resting State." Cerebral Cortex.

Allen, E. A., E. B. Erhardt, E. Damaraju, W. Gruner, J. M. Segall, R. F. Silva, M. Havlicek, S. Rachakonda, J. Fries, R. Kalyanam, A. M. Michael, A. Caprihan, J. A. Turner, T. Eichele, S. Adelsheim, A. D. Bryan, J. Bustillo, V. P. Clark, S. W. Feldstein Ewing, F. Filbey, C. C. Ford, K. Hutchison, R. E. Jung, K. A. Kiehl, P. Kodituwakku, Y. M. Komesu, A. R. Mayer, G. D. Pearlson, J. P. Phillips, J. R. Sadek, M. Stevens, U. Teuscher, R. J. Thoma and V. D. Calhoun (2011). "A baseline for the multivariate comparison of resting state networks." Frontiers in Systems Neuroscience **5**.

Allen, E. A., E. B. Erhardt, Y. Wei, T. Eichele and V. D. Calhoun (2012). "Capturing inter-subject variability with group independent component analysis of fMRI data: a simulation study." Neuroimage **59**(4): 4141-4159.

Amico, E., F. Gomez, C. Di Perri, A. Vanhaudenhuyse, D. Lesenfants, P. Boveroux, V. Bonhomme, J.-F. Brichant, D. Marinazzo and S. Laureys (2014). "Posterior Cingulate Cortex-Related Co-Activation Patterns: A Resting State fMRI Study in Propofol-Induced Loss of Consciousness." PLOS ONE **9**(6): e100012.

Apostolova, L. G. and P. M. Thompson (2008). "Mapping progressive brain structural changes in early Alzheimer's disease and mild cognitive impairment." Neuropsychologia **46**: 1597-1612.

Arbabshirani, M. R., S. Plis, J. Sui and V. D. Calhoun (2017). "Single subject prediction of brain disorders in neuroimaging: Promises and pitfalls." NeuroImage **145**: 137-165.

References

Bach, S., A. Binder, G. Montavon, F. Klauschen, K. R. Müller and W. Samek (2015). "On pixel-wise explanations for non-linear classifier decisions by layer-wise relevance propagation." PLoS ONE **10**.

Bailly, M., C. Destrieux, C. Hommet, K. Mondon, J.-p. Cottier, E. Beaufils, E. Vierron, J. Vercouillie, M. Ibazizene, T. Voisin, P. Payoux, L. Barré, V. Camus, D. Guilloteau and M.-j. Ribeiro (2015). "Precuneus and Cingulate Cortex Atrophy and Hypometabolism in Patients with Alzheimer's Disease and Mild Cognitive Impairment: MRI and 18 F-FDG PET Quantitative Analysis Using FreeSurfer." BioMed Research International **2015**: 1-8.

Barttfeld, P., L. Uhrig, J. D. Sitt, M. Sigman, B. Jarraya and S. Dehaene (2015). "Signature of consciousness in the dynamics of resting-state brain activity." Proceedings of the National Academy of Sciences **112**(3): 887-892.

Bassett, D. S., E. Bullmore, B. A. Verchinski, V. S. Mattay, D. R. Weinberger and A. Meyer-Lindenberg (2008). "Hierarchical Organization of Human Cortical Networks in Health and Schizophrenia." The Journal of neuroscience : the official journal of the Society for Neuroscience **28**(37): 9239-9248.

Betzel, R. F., M. Fukushima, Y. He, X.-N. Zuo and O. Sporns (2016). "Dynamic fluctuations coincide with periods of high and low modularity in resting-state functional brain networks." NeuroImage **127**: 287-297.

Bießmann, F., S. Plis, F. C. Meinecke, T. Eichele and K.-R. Muller (2011). "Analysis of multimodal neuroimaging data." IEEE Reviews in Biomedical Engineering **4**: 26-58.

Binder, J. R., R. H. Desai, W. W. Graves and L. L. Conant (2009). "Where is the semantic system? A critical review and meta-analysis of 120 functional neuroimaging studies." Cereb Cortex **19**(12): 2767-2796.

Biswal, B., F. Z. Yetkin, V. M. Haughton and J. S. Hyde (1995). "Functional connectivity in the motor cortex of resting human brain using echo-planar MRI." Magn Reson Med **34**(4): 537-541.

References

Borgnat, P., P. Flandrin, P. Honeine, C. Richard and J. Xiao (2010). "Testing Stationarity with Surrogates: A Time-Frequency Approach." IEEE Transactions on Signal Processing(3459-3470): 3459-3470.

Braak, H. and E. Braak (1991). "Alzheimer's disease affects limbic nuclei of the thalamus." Acta Neuropathologica **81**: 261-268.

Braak, H. and E. Braak (1991). "Neuropathological stageing of Alzheimer-related changes." Acta Neuropathologica **82**: 239-259.

Bradford, A., M. E. Kunik, P. Schulz, S. P. Williams and H. Singh (2009). "Missed and Delayed Diagnosis of Dementia in Primary Care." Alzheimer Disease & Associated Disorders **23**: 306-314.

Britz, J., D. Van De Ville and C. M. Michel (2010). "BOLD correlates of EEG topography reveal rapid resting-state network dynamics." Neuroimage **52**(4): 1162-1170.

Buchanan, R. W., A. Francis, C. Arango, K. Miller, D. M. Lefkowitz, R. P. McMahon, P. E. Barta and G. D. Pearlson (2004). "Morphometric assessment of the heteromodal association cortex in schizophrenia." Am J Psychiatry **161**(2): 322-331.

Burton, E. J., R. Barber, E. B. Mukaetova-Ladinska, J. Robson, R. H. Perry, E. Jaros, R. N. Kalaria and J. T. O'Brien (2009). "Medial temporal lobe atrophy on MRI differentiates Alzheimer's disease from dementia with Lewy bodies and vascular cognitive impairment: a prospective study with pathological verification of diagnosis." Brain **132**: 195-203.

Cabral, C., L. Kambeitz-Ilankovic, J. Kambeitz, V. D. Calhoun, D. B. Dwyer, S. von Saldern, M. F. Urquijo, P. Falkai and N. Koutsouleris (2016). "Classifying Schizophrenia Using Multimodal Multivariate Pattern Recognition Analysis: Evaluating the Impact of Individual Clinical Profiles on the Neurodiagnostic Performance." Schizophrenia Bulletin **42**(suppl_1): S110-S117.

Calhoun, V. D. and T. Adali (2009). "Feature-based fusion of medical imaging data." IEEE Transactions on Information Technology in Biomedicine **13**: 711-720.

Calhoun, V. D. and T. Adali (2016). "Time-Varying Brain Connectivity in fMRI Data: Whole-brain data-driven approaches for capturing and characterizing dynamic states." IEEE Signal Processing Magazine **33**(3): 52-66.

Calhoun, V. D. and T. Adalı (2012). "Multi-subject Independent Component Analysis of fMRI: A Decade of Intrinsic Networks, Default Mode, and Neurodiagnostic Discovery." IEEE reviews in biomedical engineering **5**: 60-73.

Calhoun, V. D., T. Adali, N. R. Giuliani, J. J. Pekar, K. A. Kiehl and G. D. Pearlson (2006). "Method for multimodal analysis of independent source differences in schizophrenia: combining gray matter structural and auditory oddball functional data." Hum Brain Mapp **27**(1): 47-62.

Calhoun, V. D., T. Adali, G. D. Pearlson and J. J. Pekar (2001). "A method for making group inferences from functional MRI data using independent component analysis." Hum Brain Mapp **14**(3): 140-151.

Calhoun, V. D., J. Liu and T. Adali (2009). "A review of group ICA for fMRI data and ICA for joint inference of imaging, genetic, and ERP data." NeuroImage **45**(1 Suppl): S163-S172.

Calhoun, V. D., R. Miller, G. Pearlson and T. Adalı (2014). "The Chronnectome: Time-Varying Connectivity Networks as the Next Frontier in fMRI Data Discovery." Neuron **84**(2): 262-274.

Calhoun, V. D. and J. Sui (2016). "Multimodal fusion of brain imaging data: A key to finding the missing link(s) in complex mental illness." Biological psychiatry : cognitive neuroscience and neuroimaging **1**(3): 230-244.

Camara, E., A. Rodriguez-Fornells and T. F. Munte (2010). "Microstructural brain differences predict functional hemodynamic responses in a reward processing task." J Neurosci **30**(34): 11398-11402.

References

Camchong, J., I. I. I. A. W. MacDonald, C. Bell, B. A. Mueller and K. O. Lim (2011). "Altered Functional and Anatomical Connectivity in Schizophrenia." Schizophrenia Bulletin **37**(3): 640-650.

Caprihan, A., C. Abbott, J. Yamamoto, G. Pearlson, N. Perrone-Bizzozero, J. Sui and V. D. Calhoun (2011). "Source-Based Morphometry Analysis of Group Differences in Fractional Anisotropy in Schizophrenia." Brain Connectivity **1**(2): 133-145.

Casanova, R., F. C. Hsu and M. A. Espeland (2012). "Classification of Structural MRI Images in Alzheimer's Disease from the Perspective of Ill-Posed Problems." PLoS ONE **7**.

Casey, D. a., D. Antimisiaris and J. O'Brien (2010). "Drugs for Alzheimer's disease: are they effective?" P & T : a peer-reviewed journal for formulary management **35**: 208-211.

Castro, E., C. N. Gupta, M. Martínez-Ramón, V. D. Calhoun, M. R. Arbabshirani and J. Turner (2014). "Identification of Patterns of Gray Matter Abnormalities in Schizophrenia using Source-Based Morphometry and Bagging." Conference proceedings : ... Annual International Conference of the IEEE Engineering in Medicine and Biology Society. IEEE Engineering in Medicine and Biology Society. Annual Conference **2014**: 1513-1516.

Castro, E., A. Ulloa, S. M. Plis, J. A. Turner and V. D. Calhoun (2015). Generation of synthetic structural magnetic resonance images for deep learning pre-training. 2015 IEEE 12th International Symposium on Biomedical Imaging (ISBI).

Cavanna, A. E. and M. R. Trimble (2006). "The precuneus: a review of its functional anatomy and behavioural correlates." Brain **129**(Pt 3): 564-583.

Cetin, M. S., J. M. Houck, B. Rashid, O. Agacoglu, J. M. Stephen, J. Sui, J. Canive, A. Mayer, C. Aine, J. R. Bustillo and V. D. Calhoun (2016). "Multimodal Classification of Schizophrenia Patients with MEG and fMRI Data Using Static and Dynamic Connectivity Measures." Front Neurosci **10**: 466.

Chan, D., N. C. Fox, R. I. Scahill, W. R. Crum, J. L. Whitwell, G. Leschziner, A. M. Rossor, J. M. Stevens, L. Cipolotti and M. N. Rossor (2001). "Patterns of temporal lobe atrophy in semantic dementia and Alzheimer's disease." Annals of Neurology **49**: 433-442.

References

Chang, C. and G. H. Glover (2010). "Time-frequency dynamics of resting-state brain connectivity measured with fMRI." Neuroimage **50**(1): 81-98.

Chang, C., Z. Liu, M. C. Chen, X. Liu and J. H. Duyn (2013). "EEG correlates of time-varying BOLD functional connectivity." Neuroimage **72**: 227-236.

Chen, K., E. M. Reiman, Z. Huan, R. J. Caselli, D. Bandy, N. Ayutyanont and G. E. Alexander (2009). "Linking Functional and Structural Brain Images with Multivariate Network Analyses: A Novel Application of the Partial Least Square Method." NeuroImage **47**(2): 602-610.

Chen, Y., B. Shi, C. D. Smith and J. Liu (2015). Nonlinear feature transformation and deep fusion for Alzheimer's disease staging analysis. Lecture Notes in Computer Science (including subseries Lecture Notes in Artificial Intelligence and Lecture Notes in Bioinformatics). **9352:** 304-312.

Cheng, B., M. Liu, D. Zhang and B. C. Munsell (2015). "Domain Transfer Learning for MCI Coversion Prediction." Ieee Transaction on Biomedical Engineering **62**: 1805-1817.

Cho, H., J. H. Kim, C. Kim, B. S. Ye, H. J. Kim, C. W. Yoon, Y. Noh, G. H. Kim, Y. J. Kim, J. H. Kim, C. H. Kim, S. J. Kang, J. Chin, S. T. Kim, K. H. Lee, D. L. Na, J. K. Seong and S. W. Seo (2014). "Shape changes of the basal ganglia and thalamus in Alzheimer's disease: A three-year longitudinal study." Journal of Alzheimer's Disease **40**: 285-295.

Choe, A. S., M. B. Nebel, A. D. Barber, J. R. Cohen, Y. Xu, J. J. Pekar, B. Caffo and M. A. Lindquist (2017). "Comparing test-retest reliability of dynamic functional connectivity methods." NeuroImage **158**: 155-175.

Clos, M., R. Langner, M. Meyer, M. S. Oechslin, K. Zilles and S. B. Eickhoff (2014). "Effects of prior information on decoding degraded speech: An fMRI study." Human Brain Mapping **35**(1): 61-74.

Cocchi, L., M. V. Sale, L. L Gollo, P. T. Bell, V. T. Nguyen, A. Zalesky, M. Breakspear and J. B. Mattingley (2016). "A hierarchy of timescales explains distinct effects of local inhibition of primary visual cortex and frontal eye fields." eLife **5**: e15252.

References

Connolly, A., E. Gaehl, H. Martin, J. Morris and N. Purandare (2011). "Underdiagnosis of dementia in primary care: Variations in the observed prevalence and comparisons to the expected prevalence." <u>Aging and Mental Health</u> **15**: 978-984.

Correa, N., T. Adalı and V. D. Calhoun (2007). "Performance of blind source separation algorithms for fMRI analysis using a group ICA method." <u>Magnetic Resonance Imaging</u> **25**(5): 684-694.

Correa, N. M., T. Adali, Y.-O. Li and V. D. Calhoun (2010). "Canonical Correlation Analysis for Data Fusion and Group Inferences: Examining applications of medical imaging data." <u>IEEE signal processing magazine</u> **27**(4): 39-50.

Costafreda, S. G., I. D. Dinov, Z. Tu, Y. Shi, C. Y. Liu, I. Kloszewska, P. Mecocci, H. Soininen, M. Tsolaki, B. Vellas, L. O. Wahlund, C. Spenger, A. W. Toga, S. Lovestone and A. Simmons (2011). "Automated hippocampal shape analysis predicts the onset of dementia in mild cognitive impairment." <u>NeuroImage</u> **56**: 212-219.

Craddock, R. C., G. A. James, P. E. Holtzheimer, 3rd, X. P. Hu and H. S. Mayberg (2012). "A whole brain fMRI atlas generated via spatially constrained spectral clustering." <u>Hum Brain Mapp</u> **33**(8): 1914-1928.

Damaraju, E., E. A. Allen, A. Belger, J. M. Ford, S. McEwen, D. H. Mathalon, B. A. Mueller, G. D. Pearlson, S. G. Potkin, A. Preda, J. A. Turner, J. G. Vaidya, T. G. van Erp and V. D. Calhoun (2014). "Dynamic functional connectivity analysis reveals transient states of dysconnectivity in schizophrenia." <u>NeuroImage: Clinical</u> **5**: 298-308.

Damoiseaux, J. S., S. A. R. B. Rombouts, F. Barkhof, P. Scheltens, C. J. Stam, S. M. Smith and C. F. Beckmann (2006). "Consistent resting-state networks across healthy subjects." <u>Proceedings of the National Academy of Sciences of the United States of America</u> **103**(37): 13848-13853.

Dansereau, C., Y. Benhajali, C. Risterucci, E. M. Pich, P. Orban, D. Arnold and P. Bellec (2017). "Statistical power and prediction accuracy in multisite resting-state fMRI connectivity." <u>Neuroimage</u> **149**: 220-232.

References

De Jong, L. W., K. Van Der Hiele, I. M. Veer, J. J. Houwing, R. G. J. Westendorp, E. L. E. M. Bollen, P. W. De Bruin, H. A. M. Middelkoop, M. A. Van Buchem and J. Van Der Grond (2008). "Strongly reduced volumes of putamen and thalamus in Alzheimer's disease: An MRI study." Brain **131**: 3277-3285.

de Pasquale, F., S. Della Penna, A. Z. Snyder, C. Lewis, D. Mantini, L. Marzetti, P. Belardinelli, L. Ciancetta, V. Pizzella, G. L. Romani and M. Corbetta (2010). "Temporal dynamics of spontaneous MEG activity in brain networks." Proc Natl Acad Sci U S A **107**(13): 6040-6045.

Deng, L., J. Sun, L. Cheng and S. Tong (2016). "Characterizing dynamic local functional connectivity in the human brain." Scientific Reports **6**: 26976.

Devanand, D. P., G. Pradhaban, X. Liu, A. Khandji, S. De Santi, S. Segal, H. Rusinek, G. H. Pelton, L. S. Honig, R. Mayeux, Y. Stern, M. H. Tabert and M. J. De Leon (2007). "Hippocampal and entorhinal atrophy in mild cognitive impairment: Prediction of Alzheimer disease." Neurology **68**: 828-836.

Du, Y. and Y. Fan (2013). "Group information guided ICA for fMRI data analysis." NeuroImage **69**: 157-197.

Du, Y., Z. Fu, D. Lin, M. Salman, M. Rahaman, A. Abrol and V. D. Calhoun (2018). "Shared and Specific Changes of Functional Networks in Schizophrenia and Autism Spectrum Disorder." OHBM 2018.

Du, Y., G. D. Pearlson, Q. Yu, H. He, D. Lin, J. Sui, L. Wu and V. D. Calhoun (2016). "Interaction among subsystems within default mode network diminished in schizophrenia patients: A dynamic connectivity approach." Schizophr Res **170**(1): 55-65.

Eickhoff, S. B., K. E. Stephan, H. Mohlberg, C. Grefkes, G. R. Fink, K. Amunts and K. Zilles (2005). "A new SPM toolbox for combining probabilistic cytoarchitectonic maps and functional imaging data." Neuroimage **25**(4): 1325-1335.

References

Erhardt, E. B., S. Rachakonda, E. J. Bedrick, E. A. Allen, T. Adali and V. D. Calhoun (2011). "Comparison of multi-subject ICA methods for analysis of fMRI data." Hum Brain Mapp **32**(12): 2075-2095.

Falahati, F., E. Westman and A. Simmons (2014). Multivariate data analysis and machine learning in Alzheimer's disease with a focus on structural magnetic resonance imaging. Journal of Alzheimer's Disease. **41:** 685-708.

Fennema-Notestine, C., D. J. Hagler, L. K. McEvoy, A. S. Fleisher, E. H. Wu, D. S. Karow and A. M. Dale (2009). "Structural MRI biomarkers for preclinical and mild Alzheimer's disease." Human Brain Mapping **30**: 3238-3253.

Filippini, N., B. J. MacIntosh, M. G. Hough, G. M. Goodwin, G. B. Frisoni, S. M. Smith, P. M. Matthews, C. F. Beckmann and C. E. Mackay (2009). "Distinct patterns of brain activity in young carriers of the APOE-epsilon4 allele." Proc Natl Acad Sci U S A **106**(17): 7209-7214.

Fletcher, P. C., T. Shallice, C. D. Frith, R. S. Frackowiak and R. J. Dolan (1996). "Brain activity during memory retrieval. The influence of imagery and semantic cueing." Brain **119 (Pt 5)**: 1587-1596.

Ford, J. M., D. H. Mathalon, S. Whitfield, W. O. Faustman and W. T. Roth (2002). "Reduced communication between frontal and temporal lobes during talking in schizophrenia." Biol Psychiatry **51**(6): 485-492.

Fox, M. D. and M. E. Raichle (2007). "Spontaneous fluctuations in brain activity observed with functional magnetic resonance imaging." Nat Rev Neurosci **8**(9): 700-711.

Fox, M. D., A. Z. Snyder, J. L. Vincent, M. Corbetta, D. C. Van Essen and M. E. Raichle (2005). "The human brain is intrinsically organized into dynamic, anticorrelated functional networks." Proceedings of the National Academy of Sciences of the United States of America **102**(27): 9673.

Fu, Z., Y. Tu, X. Di, Y. Du, G. D. Pearlson, J. A. Turner, B. B. Biswal, Z. Zhang and V. D. Calhoun (2017). "Characterizing dynamic amplitude of low-frequency fluctuation and

its relationship with dynamic functional connectivity: An application to schizophrenia." NeuroImage.

Fujiwara, H., K. Hirao, C. Namiki, M. Yamada, M. Shimizu, H. Fukuyama, T. Hayashi and T. Murai (2007). "Anterior cingulate pathology and social cognition in schizophrenia: A study of gray matter, white matter and sulcal morphometry." NeuroImage **36**(4): 1236-1245.

GAAIN. (2017). "The Global Alzheimer's Association Interactive Network, GAAIN Data." from www.gaaindata.org/partners/online.html.

Galton, C. J., K. Patterson, K. Graham, M. Uk, M. a. L. Ralph and G. Williams (2011). "Differing patterns of temporal atrophy in Alzheimer ' s disease." New York **10**: 220-225.

Garrity, A. G., G. D. Pearlson, K. McKiernan, D. Lloyd, K. A. Kiehl and V. D. Calhoun (2007). "Aberrant "default mode" functional connectivity in schizophrenia." Am J Psychiatry **164**(3): 450-457.

Giuliani, N. R., V. D. Calhoun, G. D. Pearlson, A. Francis and R. W. Buchanan (2005). "Voxel-based morphometry versus region of interest: a comparison of two methods for analyzing gray matter differences in schizophrenia." Schizophr Res **74**(2-3): 135-147.

Glahn, D. C., A. R. Laird, I. Ellison-Wright, S. M. Thelen, J. L. Robinson, J. L. Lancaster, E. Bullmore and P. T. Fox (2008). "Meta-analysis of gray matter anomalies in schizophrenia: application of anatomic likelihood estimation and network analysis." Biol Psychiatry **64**(9): 774-781.

Glerean, E., J. Salmi, J. M. Lahnakoski, I. P. Jaaskelainen and M. Sams (2012). "Functional magnetic resonance imaging phase synchronization as a measure of dynamic functional connectivity." Brain Connect **2**(2): 91-101.

Gonzalez-Castillo, J., C. W. Hoy, D. A. Handwerker, M. E. Robinson, L. C. Buchanan, Z. S. Saad and P. A. Bandettini (2015). "Tracking ongoing cognition in individuals using brief, whole-brain functional connectivity patterns." Proceedings of the National Academy of Sciences **112**(28): 8762-8767.

References

Groves, A. R., C. F. Beckmann, S. M. Smith and M. W. Woolrich (2011). "Linked independent component analysis for multimodal data fusion." NeuroImage **54**(3): 2198-2217.

Guo, C. C., R. Tan, J. R. Hodges, X. Hu, S. Sami and M. Hornberger (2016). "Network-selective vulnerability of the human cerebellum to Alzheimer's disease and frontotemporal dementia." Brain **139**: 1527-1538.

Gupta, C. N., V. D. Calhoun, S. Rachakonda, J. Chen, V. Patel, J. Liu, J. Segall, B. Franke, M. P. Zwiers, A. Arias-Vasquez, J. Buitelaar, S. E. Fisher, G. Fernandez, T. G. M. van Erp, S. Potkin, J. Ford, D. Mathalon, S. McEwen, H. J. Lee, B. A. Mueller, D. N. Greve, O. Andreassen, I. Agartz, R. L. Gollub, S. R. Sponheim, S. Ehrlich, L. Wang, G. Pearlson, D. C. Glahn, E. Sprooten, A. R. Mayer, J. Stephen, R. E. Jung, J. Canive, J. Bustillo and J. A. Turner (2015). "Patterns of Gray Matter Abnormalities in Schizophrenia Based on an International Mega-analysis." Schizophrenia Bulletin **41**(5): 1133-1142.

Haghighat, M., M. Abdel-Mottaleb and W. Alhalabi (2016). "Fully automatic face normalization and single sample face recognition in unconstrained environments." Expert Systems with Applications **47**: 23-34.

Hagmann, P., L. Cammoun, X. Gigandet, R. Meuli, C. J. Honey, V. J. Wedeen and O. Sporns (2008). "Mapping the Structural Core of Human Cerebral Cortex." PLOS Biology **6**(7): e159.

Hall, D. A., C. Fussell and A. Q. Summerfield (2005). "Reading fluent speech from talking faces: typical brain networks and individual differences." J Cogn Neurosci **17**(6): 939-953.

Handwerker, D. A., V. Roopchansingh, J. Gonzalez-Castillo and P. A. Bandettini (2012). "Periodic changes in fMRI connectivity." Neuroimage **63**(3): 1712-1719.

He, B. J., A. Z. Snyder, J. M. Zempel, M. D. Smyth and M. E. Raichle (2008). "Electrophysiological correlates of the brain's intrinsic large-scale functional architecture." Proceedings of the National Academy of Sciences **105**(41): 16039.

References

He, K., X. Zhang, S. Ren and J. Sun (2016). Deep Residual Learning for Image Recognition. 2016 IEEE Conference on Computer Vision and Pattern Recognition (CVPR)**:** 770-778.

He, K., X. Zhang, S. Ren and J. Sun (2016). Identity mappings in deep residual networks. Lecture Notes in Computer Science (including subseries Lecture Notes in Artificial Intelligence and Lecture Notes in Bioinformatics). **9908 LNCS:** 630-645.

Himberg, J., A. Hyvarinen and F. Esposito (2004). "Validating the independent components of neuroimaging time series via clustering and visualization." Neuroimage **22**(3): 1214-1222.

Hindriks, R., M. H. Adhikari, Y. Murayama, M. Ganzetti, D. Mantini, N. K. Logothetis and G. Deco (2016). "Can sliding-window correlations reveal dynamic functional connectivity in resting-state fMRI?" NeuroImage **127**: 242-256.

Honey, C. J., O. Sporns, L. Cammoun, X. Gigandet, J. P. Thiran, R. Meuli and P. Hagmann (2009). "Predicting human resting-state functional connectivity from structural connectivity." Proceedings of the National Academy of Sciences **106**(6): 2035-2040.

Huang, C., L.-O. Wahlund, L. Svensson, B. Winblad and P. Julin (2002). "Cingulate cortex hypoperfusion predicts Alzheimer's disease in mild cognitive impairment." BMC Neurology **2**: 9.

Hudson, A. E., D. P. Calderon, D. W. Pfaff and A. Proekt (2014). "Recovery of consciousness is mediated by a network of discrete metastable activity states." Proceedings of the National Academy of Sciences **111**(25): 9283-9288.

Hulshoff Pol, H. E., H. G. Schnack, R. C. Mandl, N. E. van Haren, H. Koning, D. L. Collins, A. C. Evans and R. S. Kahn (2001). "Focal gray matter density changes in schizophrenia." Arch Gen Psychiatry **58**(12): 1118-1125.

Hutchison, R. M. and J. B. Morton (2015). "Tracking the Brain's Functional Coupling Dynamics over Development." The Journal of Neuroscience **35**(17): 6849.

References

Hutchison, R. M., T. Womelsdorf, E. A. Allen, P. A. Bandettini, V. D. Calhoun, M. Corbetta, S. Della Penna, J. H. Duyn, G. H. Glover, J. Gonzalez-Castillo, D. A. Handwerker, S. Keilholz, V. Kiviniemi, D. A. Leopold, F. de Pasquale, O. Sporns, M. Walter and C. Chang (2013). "Dynamic functional connectivity: promise, issues, and interpretations." Neuroimage **80**: 360-378.

Hutchison, R. M., T. Womelsdorf, J. S. Gati, S. Everling and R. S. Menon (2013). "Resting-state networks show dynamic functional connectivity in awake humans and anesthetized macaques." Human Brain Mapping **34**(9): 2154-2177.

Ioffe, S. and C. Szegedy (2015). "Batch Normalization: Accelerating Deep Network Training by Reducing Internal Covariate Shift." CoRR **abs/1502.0**.

Jacobs, H. I. L., D. A. Hopkins, H. C. Mayrhofer, E. Bruner, F. W. van Leeuwen, W. Raaijmakers and J. D. Schmahmann (2017). "The cerebellum in Alzheimer's disease: evaluating its role in cognitive decline." Brain.

Jiji, S., K. A. Smitha, A. K. Gupta, V. P. M. Pillai and R. S. Jayasree (2013). "Segmentation and volumetric analysis of the caudate nucleus in Alzheimer's disease." European Journal of Radiology **82**: 1525-1530.

Johnson, N. A., G.-H. Jahng, M. W. Weiner, B. L. Miller, H. C. Chui, W. J. Jagust, M. L. Gorno-Tempini and N. Schuff (2005). "Pattern of Cerebral Hypoperfusion in Alzheimer Disease and Mild Cognitive Impairment Measured with Arterial Spin-labeling MR Imaging: Initial Experience." Radiology **234**: 851-859.

Jones, B. F., J. Barnes, H. B. M. Uylings, N. C. Fox, C. Frost, M. P. Witter and P. Scheltens (2006). "Differential regional atrophy of the cingulate gyrus in Alzheimer disease: A volumetric MRI study." Cerebral Cortex **16**: 1701-1708.

Kantarci, K., S. D. Weigand, S. A. Przybelski, M. M. Shiung, J. L. Whitwell, S. Negash, D. S. Knopman, B. F. Boeve, P. C. O'Brien, R. C. Petersen and C. R. Jack (2009). "Risk of dementia in MCI: Combined effect of cerebrovascular disease, volumetric MRI, and 1H MRS." Neurology **72**: 1519-1525.

References

Keator, D. B., T. G. van Erp, J. A. Turner, G. H. Glover, B. A. Mueller, T. T. Liu, J. T. Voyvodic, J. Rasmussen, V. D. Calhoun, H. J. Lee, A. W. Toga, S. McEwen, J. M. Ford, D. H. Mathalon, M. Diaz, D. S. O'Leary, H. Jeremy Bockholt, S. Gadde, A. Preda, C. G. Wible, H. S. Stern, A. Belger, G. McCarthy, B. Ozyurt and S. G. Potkin (2016). "The Function Biomedical Informatics Research Network Data Repository." <u>Neuroimage</u> **124**(Pt B): 1074-1079.

Kettenring, J. R. (1971). "Canonical Analysis of Several Sets of Variables." <u>Biometrika</u> **58**(3): 433-451.

Killiany, R. J., T. Gomez-Isla, M. Moss, R. Kikinis, T. Sandor, F. Jolesz, R. Tanzi, K. Jones, B. T. Hyman and M. S. Albert (2000). "Use of structural magnetic resonance imaging to predict who will get Alzheimer's disease." <u>Annals of neurology</u> **47**: 430-439.

Kingma, D. P. and J. L. Ba (2015). "Adam: a Method for Stochastic Optimization." <u>International Conference on Learning Representations 2015</u>: 1-15.

Kiviniemi, V., T. Starck, J. Remes, X. Long, J. Nikkinen, M. Haapea, J. Veijola, I. Moilanen, M. Isohanni, Y. F. Zang and O. Tervonen (2009). "Functional segmentation of the brain cortex using high model order group PICA." <u>Hum Brain Mapp</u> **30**(12): 3865-3886.

Korolev, I. O., L. L. Symonds, A. C. Bozoki and A. s. D. N. Alzheimer's Disease Neuroimaging Initiative (2016). "Predicting Progression from Mild Cognitive Impairment to Alzheimer's Dementia Using Clinical, MRI, and Plasma Biomarkers via Probabilistic Pattern Classification." <u>PloS one</u> **11**: e0138866.

Kragel, P. A., A. R. Knodt, A. R. Hariri and K. S. LaBar (2016). "Decoding Spontaneous Emotional States in the Human Brain." <u>PLoS Biology</u> **14**(9): e2000106.

Krizhevsky, A., I. Sutskever and G. E. Hinton (2012). "ImageNet Classification with Deep Convolutional Neural Networks." <u>Advances In Neural Information Processing Systems</u>: 1-9.

Kucyi, A. (2017). "Just a thought: How mind-wandering is represented in dynamic brain connectivity." NeuroImage.

Kucyi, A. and K. D. Davis (2014). "Dynamic functional connectivity of the default mode network tracks daydreaming." NeuroImage **100**: 471-480.

Lahat, D., T. Adali and C. Jutten (2015). "Multimodal data fusion: an overview of methods, challenges, and prospects." Proceedings of the IEEE **103**(9): 1449-1477.

Lancaster, J. L., M. G. Woldorff, L. M. Parsons, M. Liotti, C. S. Freitas, L. Rainey, P. V. Kochunov, D. Nickerson, S. A. Mikiten and P. T. Fox (2000). "Automated Talairach atlas labels for functional brain mapping." Hum Brain Mapp **10**(3): 120-131.

Lapuschkin, S., A. Binder, G. Montavon, K.-R. Müller and W. Samek (2016). "The Layer-wise Relevance Propagation Toolbox for Artificial Neural Networks." Journal of Machine Learning Research **17**: 1-5.

Laumann, T. O., A. Z. Snyder, A. Mitra, E. M. Gordon, C. Gratton, B. Adeyemo, A. W. Gilmore, S. M. Nelson, J. J. Berg, D. J. Greene, J. E. McCarthy, E. Tagliazucchi, H. Laufs, B. L. Schlaggar, N. U. Dosenbach and S. E. Petersen (2016). "On the Stability of BOLD fMRI Correlations." Cereb Cortex.

Leonardi, N. and D. Van De Ville (2015). "On spurious and real fluctuations of dynamic functional connectivity during rest." Neuroimage **104**: 430-436.

Li, F., L. Tran, K. H. Thung, S. Ji, D. Shen and J. Li (2015). "A Robust Deep Model for Improved Classification of AD/MCI Patients." IEEE Journal of Biomedical and Health Informatics **19**: 1610-1616.

Li, J., D. Zhang, A. Liang, B. Liang, Z. Wang, Y. Cai, M. Gao, Z. Gao, S. Chang, B. Jiao, R. Huang and M. Liu (2017). "High transition frequencies of dynamic functional connectivity states in the creative brain." **7**: 46072.

References

Li, X., D. Zhu, X. Jiang, C. Jin, X. Zhang, L. Guo, J. Zhang, X. Hu, L. Li and T. Liu (2014). "Dynamic functional connectomics signatures for characterization and differentiation of PTSD patients." Human Brain Mapping **35**(4): 1761-1778.

Liegeois, R., T. O. Laumann, A. Z. Snyder, H. J. Zhou and B. T. T. Yeo (2017). "Interpreting Temporal Fluctuations In Resting-State Functional Connectivity MRI." bioRxiv.

Liégeois, R., E. Ziegler, C. Phillips, P. Geurts, F. Gómez, M. A. Bahri, B. T. T. Yeo, A. Soddu, A. Vanhaudenhuyse, S. Laureys and R. Sepulchre (2016). "Cerebral functional connectivity periodically (de)synchronizes with anatomical constraints." Brain Structure and Function **221**(6): 2985-2997.

Lindquist, M. A., Y. Xu, M. B. Nebel and B. S. Caffo (2014). "Evaluating dynamic bivariate correlations in resting-state fMRI: a comparison study and a new approach." Neuroimage **101**: 531-546.

Litjens, G., T. Kooi, B. E. Bejnordi, A. A. A. Setio, F. Ciompi, M. Ghafoorian, J. A. W. M. van der Laak, B. van Ginneken and C. I. Sánchez (2017). A survey on deep learning in medical image analysis. Medical Image Analysis. **42:** 60-88.

Liu, J., H. J. Lee, A. J. Weitz, Z. Fang, P. Lin, M. Choy, R. Fisher, V. Pinskiy, A. Tolpygo, P. Mitra, N. Schiff and J. H. Lee (2015). "Frequency-selective control of cortical and subcortical networks by central thalamus." eLife **4**: e09215.

Liu, J., G. Pearlson, A. Windemuth, G. Ruano, N. I. Perrone-Bizzozero and V. Calhoun (2009). "Combining fMRI and SNP data to investigate connections between brain function and genetics using parallel ICA." Hum Brain Mapp **30**(1): 241-255.

Liu, M., D. Zhang and D. Shen (2014). "Hierarchical fusion of features and classifier decisions for Alzheimer's disease diagnosis." Human Brain Mapping **35**: 1305-1319.

Liu, S., S. Liu, W. Cai, S. Pujol, R. Kikinis and D. D. Feng (2015). Multi-phase feature representation learning for neurodegenerative disease diagnosis. 1st Australasian

References

Conference on Artificial Life and Computational Intelligence, ACALCI 2015, February 5, 2015 - February 7. **8955:** 350-359.

Liu, X., C. Chang and J. H. Duyn (2013). "Decomposition of Spontaneous Brain Activity into Distinct fMRI Co-activation Patterns." Frontiers in Systems Neuroscience **7**.

Liu, X. and J. H. Duyn (2013). "Time-varying functional network information extracted from brief instances of spontaneous brain activity." Proc Natl Acad Sci U S A **110**(11): 4392-4397.

Lu, D., K. Popuri, G. W. Ding, R. Balachandar and M. F. Beg (2018). "Multimodal and Multiscale Deep Neural Networks for the Early Diagnosis of Alzheimer's Disease using structural MR and FDG-PET images." Scientific Reports **8**: 5697.

Maaten, L. v. d. and G. E. Hinton (2008). "Visualizing Data using t-SNE." Journal of Machine Learning Research **9**(Nov): 2579-2605.

Madhyastha, T. M., M. K. Askren, P. Boord and T. J. Grabowski (2015). "Dynamic Connectivity at Rest Predicts Attention Task Performance." Brain Connectivity **5**(1): 45-59.

Makris, N., J. M. Goldstein, D. Kennedy, S. M. Hodge, V. S. Caviness, S. V. Faraone, M. T. Tsuang and L. J. Seidman (2006). "Decreased volume of left and total anterior insular lobule in schizophrenia." Schizophr Res **83**(2-3): 155-171.

Mantini, D., M. G. Perrucci, C. Del Gratta, G. L. Romani and M. Corbetta (2007). "Electrophysiological signatures of resting state networks in the human brain." Proc Natl Acad Sci U S A **104**(32): 13170-13175.

Margulies, D. S., A. M. Kelly, L. Q. Uddin, B. B. Biswal, F. X. Castellanos and M. P. Milham (2007). "Mapping the functional connectivity of anterior cingulate cortex." Neuroimage **37**(2): 579-588.

Markesbery, W. R. (2010). Neuropathologic alterations in mild cognitive impairment: A review. Journal of Alzheimer's Disease. **19:** 221-228.

References

Martinez-Montes, E., P. A. Valdes-Sosa, F. Miwakeichi, R. I. Goldman and M. S. Cohen (2004). "Concurrent EEG/fMRI analysis by multiway Partial Least Squares." Neuroimage **22**(3): 1023-1034.

Matsui, T., T. Murakami and K. Ohki (2017). "Neuronal origin of the temporal dynamics of spontaneous BOLD activity correlation." bioRxiv.

McKeown, M. J., S. Makeig, G. G. Brown, T. P. Jung, S. S. Kindermann, A. J. Bell and T. J. Sejnowski (1998). "Analysis of fMRI data by blind separation into independent spatial components." Hum Brain Mapp **6**(3): 160-188.

McKeown, M. J. and T. J. Sejnowski (1998). "Independent component analysis of fMRI data: examining the assumptions." Hum Brain Mapp **6**(5-6): 368-372.

Michael, A. M., S. A. Baum, T. White, O. Demirci, N. C. Andreasen, J. M. Segall, R. E. Jung, G. Pearlson, V. P. Clark, R. L. Gollub, S. C. Schulz, J. L. Roffman, K. O. Lim, B.-C. Ho, H. J. Bockholt and V. D. Calhoun (2010). "Does function follow form?: Methods to fuse structural and functional brain images show decreased linkage in schizophrenia." NeuroImage **49**(3): 2626-2637.

Miller, R. L., A. Abrol, T. Adali, Y. Levin-Schwarz and V. D. Calhoun (2018). "Resting-State fMRI Dynamics and Null Models: Perspectives, Sampling Variability, and Simulations." **12**(551).

Miller, R. L., M. Yaesoubi, J. A. Turner, D. Mathalon, A. Preda, G. Pearlson, T. Adali and V. D. Calhoun (2016). "Higher Dimensional Meta-State Analysis Reveals Reduced Resting fMRI Connectivity Dynamism in Schizophrenia Patients." PLoS ONE **11**(3): e0149849.

Moradi, E., A. Pepe, C. Gaser, H. Huttunen and J. Tohka (2015). "Machine learning framework for early MRI-based Alzheimer's conversion prediction in MCI subjects." NeuroImage **104**: 398-412.

References

Nieuwenhuis, M., N. E. van Haren, H. E. Hulshoff Pol, W. Cahn, R. S. Kahn and H. G. Schnack (2012). "Classification of schizophrenia patients and healthy controls from structural MRI scans in two large independent samples." Neuroimage **61**(3): 606-612.

Olesen, P. J., Z. Nagy, H. Westerberg and T. Klingberg (2003). "Combined analysis of DTI and fMRI data reveals a joint maturation of white and grey matter in a fronto-parietal network." Brain Res Cogn Brain Res **18**(1): 48-57.

Ongur, D., M. Lundy, I. Greenhouse, A. K. Shinn, V. Menon, B. M. Cohen and P. F. Renshaw (2010). "Default mode network abnormalities in bipolar disorder and schizophrenia." Psychiatry Res **183**(1): 59-68.

Pascual-Marqui, R. D., C. M. Michel and D. Lehmann (1995). "Segmentation of brain electrical activity into microstates: model estimation and validation." IEEE Trans Biomed Eng **42**(7): 658-665.

Peruzzo, D., U. Castellani, C. Perlini, M. Bellani, V. Marinelli, G. Rambaldelli, A. Lasalvia, S. Tosato, K. De Santi, V. Murino, M. Ruggeri and P. Brambilla (2015). "Classification of first-episode psychosis: a multi-modal multi-feature approach integrating structural and diffusion imaging." Journal of Neural Transmission **122**(6): 897-905.

Plis, S. M., D. R. Hjelm, R. Slakhutdinov, E. A. Allen, H. J. Bockholt, J. D. Long, H. Johnson, J. Paulsen, J. Turner and V. D. Calhoun (2014). "Deep learning for neuroimaging: A validation study." Frontiers in Neuroscience.

Poulin, S. P., R. Dautoff, J. C. Morris, L. F. Barrett and B. C. Dickerson (2011). "Amygdala atrophy is prominent in early Alzheimer's disease and relates to symptom severity." Psychiatry Research - Neuroimaging **194**: 7-13.

Prechelt, L. (1998). Early stopping--But when? Neural Networks: Tricks of the Trade**:** 55-69.

Preti, M. G., T. A. W. Bolton and D. Van De Ville (2016). "The dynamic functional connectome: State-of-the-art and perspectives." NeuroImage.

References

Price, C. J. (2010). "The anatomy of language: a review of 100 fMRI studies published in 2009." Annals of the New York Academy of Sciences **1191**(1): 62-88.

Prichard, D. and J. Theiler (1994). "Generating surrogate data for time series with several simultaneously measured variables." Phys Rev Lett **73**: 951-954.

Pytorch. (2017). Pytroch Resnet Architecture Retrieved 2017, from www.github.com/pytorch/vision/blob/master/torchvision/models/resnet.py.

Rashid, B., M. R. Arbabshirani, E. Damaraju, M. S. Cetin, R. Miller, G. D. Pearlson and V. D. Calhoun (2016). "Classification of schizophrenia and bipolar patients using static and dynamic resting-state fMRI brain connectivity." NeuroImage **134**: 645-657.

Rashid, B., E. Damaraju, G. D. Pearlson and V. D. Calhoun (2014). "Dynamic Connectivity States Estimated from Resting fMRI Identify Differences among Schizophrenia, Bipolar Disorder, and Healthy Control Subjects." Frontiers in Human Neuroscience **8**.

Rathore, S., M. Habes, M. A. Iftikhar, A. Shacklett and C. Davatzikos (2017). A review on neuroimaging-based classification studies and associated feature extraction methods for Alzheimer's disease and its prodromal stages. NeuroImage. **155:** 530-548.

Richard, C., A. Ferrari, H. Amoud, P. Honeine, P. Flandrin and P. Borgnat (2010). Statistical hypothesis testing with time-frequency surrogates to check signal stationarity. 2010 IEEE International Conference on Acoustics, Speech and Signal Processing.

Risacher, S., A. Saykin, J. Wes, L. Shen, H. Firpi and B. McDonald (2009). "Baseline MRI Predictors of Conversion from MCI to Probable AD in the ADNI Cohort." Current Alzheimer Research **6**: 347-361.

Rugg, M. and R. Henson (2002). "Episodic memory retrieval: an (event-related) functional neuroimaging perspective." The Cognitive Neuroscience of Memory Encoding and Retrieval. Psychology Press

Rykhlevskaia, E., G. Gratton and M. Fabiani (2008). "Combining structural and functional neuroimaging data for studying brain connectivity: a review." Psychophysiology **45**(2): 173-187.

Sakoglu, U., G. D. Pearlson, K. A. Kiehl, Y. M. Wang, A. M. Michael and V. D. Calhoun (2010). "A method for evaluating dynamic functional network connectivity and task-modulation: application to schizophrenia." MAGMA **23**(5-6): 351-366.

Scahill, R. I., J. M. Schott, J. M. Stevens, M. N. Rossor and N. C. Fox (2002). "Mapping the evolution of regional atrophy in Alzheimer's disease: Unbiased analysis of fluid-registered serial MRI." Proceedings of the National Academy of Sciences **99**: 4703-4707.

Schaefer, A., D. S. Margulies, G. Lohmann, K. J. Gorgolewski, J. Smallwood, S. J. Kiebel and A. Villringer (2014). "Dynamic network participation of functional connectivity hubs assessed by resting-state fMRI." Frontiers in Human Neuroscience **8**(195).

Schmahmann, J. D. (2016). Cerebellum in Alzheimer's disease and frontotemporal dementia: Not a silent bystander. Brain. **139:** 1314-1318.

Schreiber, T. and A. Schmitz (2000). "Surrogate time series." Physica D: Nonlinear Phenomena **142**(3): 346-382.

Schultz, C. C., P. Fusar-Poli, G. Wagner, K. Koch, C. Schachtzabel, O. Gruber, H. Sauer and R. G. M. Schlösser (2012). "Multimodal functional and structural imaging investigations in psychosis research." European Archives of Psychiatry and Clinical Neuroscience **262**(2): 97-106.

Segall, J. M., E. A. Allen, R. E. Jung, E. B. Erhardt, S. K. Arja, K. Kiehl and V. D. Calhoun (2012). "Correspondence between structure and function in the human brain at rest." Frontiers in Neuroinformatics **6**: 10.

Shehzad, Z., A. M. Kelly, P. T. Reiss, D. G. Gee, K. Gotimer, L. Q. Uddin, S. H. Lee, D. S. Margulies, A. K. Roy, B. B. Biswal, E. Petkova, F. X. Castellanos and M. P. Milham (2009). "The resting brain: unconstrained yet reliable." Cereb Cortex **19**(10): 2209-2229.

References

Shen, D., G. Wu and H.-I. Suk (2017). "Deep Learning in Medical Image Analysis." Annual Review of Biomedical Engineering **19**: 221-248.

Shenton, M. E., C. C. Dickey, M. Frumin and R. W. McCarley (2001). "A review of MRI findings in schizophrenia." Schizophr Res **49**(1-2): 1-52.

Shenton, M. E., R. Kikinis, F. A. Jolesz, S. D. Pollak, M. LeMay, C. G. Wible, H. Hokama, J. Martin, D. Metcalf, M. Coleman and et al. (1992). "Abnormalities of the left temporal lobe and thought disorder in schizophrenia. A quantitative magnetic resonance imaging study." N Engl J Med **327**(9): 604-612.

Shi, J., X. Zheng, Y. Li, Q. Zhang and S. Ying (2018). "Multimodal Neuroimaging Feature Learning with Multimodal Stacked Deep Polynomial Networks for Diagnosis of Alzheimer's Disease." IEEE Journal of Biomedical and Health Informatics **22**: 173-183.

Shine, James M., Patrick G. Bissett, Peter T. Bell, O. Koyejo, Joshua H. Balsters, Krzysztof J. Gorgolewski, Craig A. Moodie and Russell A. Poldrack (2016). "The Dynamics of Functional Brain Networks: Integrated Network States during Cognitive Task Performance." Neuron **92**(2): 544-554.

Shine, J. M., O. Koyejo and R. A. Poldrack (2016). "Temporal metastates are associated with differential patterns of time-resolved connectivity, network topology, and attention." Proceedings of the National Academy of Sciences **113**(35): 9888-9891.

Shine, J. M. and R. A. Poldrack "Principles of dynamic network reconfiguration across diverse brain states." NeuroImage.

Shmuel, A. and D. A. Leopold (2008). "Neuronal correlates of spontaneous fluctuations in fMRI signals in monkey visual cortex: Implications for functional connectivity at rest." Hum Brain Mapp **29**(7): 751-761.

Silva, R. F., S. M. Plis, J. Sui, M. S. Pattichis, T. Adali and V. D. Calhoun (2016). "Blind Source Separation for Unimodal and Multimodal Brain Networks: A Unifying Framework for Subspace Modeling." IEEE J Sel Top Signal Process **10**(7): 1134-1149.

References

Simonyan, K. and A. Zisserman (2015). "VGG : Very Deep Convolutional Networks for Large-Scale Image Recognition." International Conference on Learning Representations (ICRL): 1-14.

Skudlarski, P., K. Jagannathan, K. Anderson, M. C. Stevens, V. D. Calhoun, B. A. Skudlarska and G. Pearlson (2010). "Brain connectivity is not only lower but different in schizophrenia: a combined anatomical and functional approach." Biol Psychiatry 68(1): 61-69.

Sluimer, J. D., W. M. Van Der Flier, G. B. Karas, R. Van Schijndel, J. Barnes, R. G. Boyes, K. S. Cover, S. D. Olabarriaga, N. C. Fox, P. Scheltens, H. Vrenken and F. Barkhof (2009). "Accelerating regional atrophy rates in the progression from normal aging to Alzheimer's disease." European Radiology 19: 2826-2833.

Smith, S. M., P. T. Fox, K. L. Miller, D. C. Glahn, P. M. Fox, C. E. Mackay, N. Filippini, K. E. Watkins, R. Toro, A. R. Laird and C. F. Beckmann (2009). "Correspondence of the brain's functional architecture during activation and rest." Proceedings of the National Academy of Sciences 106(31): 13040-13045.

Sockeel, S., D. Schwartz, M. Pélégrini-Issac and H. Benali (2016). "Large-Scale Functional Networks Identified from Resting-State EEG Using Spatial ICA." PLOS ONE 11(1): e0146845.

Sporns, O. (2013). "Network attributes for segregation and integration in the human brain." Current Opinion in Neurobiology 23(2): 162-171.

Srivastava, R. K., K. Greff and J. Schmidhuber (2015). "Training Very Deep Networks." NIPS: 1-9.

Stephen, J. M., B. A. Coffman, R. E. Jung, J. R. Bustillo, C. J. Aine and V. D. Calhoun (2013). "Using joint ICA to link function and structure using MEG and DTI in schizophrenia." NeuroImage 83(Supplement C): 418-430.

Sugranyes, G., M. Kyriakopoulos, D. Dima, J. O'Muircheartaigh, R. Corrigall, G. Pendelbury, D. Hayes, V. D. Calhoun and S. Frangou (2012). "Multimodal analyses

identify linked functional and white matter abnormalities within the working memory network in schizophrenia." Schizophrenia Research **138**(2): 136-142.

Sui, J., T. Adali, G. D. Pearlson and V. D. Calhoun (2009). "An ICA-based method for the identification of optimal FMRI features and components using combined group-discriminative techniques." Neuroimage **46**(1): 73-86.

Sui, J., T. Adali, Q. Yu, J. Chen and V. D. Calhoun (2012). "A review of multivariate methods for multimodal fusion of brain imaging data." J Neurosci Methods **204**(1): 68-81.

Sui, J., H. He, G. D. Pearlson, T. Adali, K. A. Kiehl, Q. Yu, V. P. Clark, E. Castro, T. White, B. A. Mueller, B. C. Ho, N. C. Andreasen and V. D. Calhoun (2013). "Three-way (N-way) fusion of brain imaging data based on mCCA+jICA and its application to discriminating schizophrenia." Neuroimage **66**: 119-132.

Sui, J., G. Pearlson, A. Caprihan, T. Adali, K. A. Kiehl, J. Liu, J. Yamamoto and V. D. Calhoun (2011). "Discriminating schizophrenia and bipolar disorder by fusing fMRI and DTI in a multimodal CCA+ joint ICA model." Neuroimage **57**(3): 839-855.

Sui, J., G. D. Pearlson, Y. Du, Q. Yu, T. R. Jones, J. Chen, T. Jiang, J. Bustillo and V. D. Calhoun (2015). "In search of multimodal neuroimaging biomarkers of cognitive deficits in schizophrenia." Biol Psychiatry **78**(11): 794-804.

Sui, J., Q. Yu, H. He, G. D. Pearlson and V. D. Calhoun (2012). "A Selective Review of Multimodal Fusion Methods in Schizophrenia." Frontiers in Human Neuroscience **6**: 27.

Suk, H.-I., S.-W. Lee and D. Shen (2015). "Deep sparse multi-task learning for feature selection in Alzheimer's disease diagnosis." Brain structure & function.

Suk, H.-I., S.-W. Lee, D. Shen and f. t. A. s. D. N. Initiative (2017). "Deep Ensemble Learning of Sparse Regression Models for Brain Disease Diagnosis." Medical Image Analysis.

Suk, H. I., S. W. Lee and D. Shen (2014). "Hierarchical feature representation and multimodal fusion with deep learning for AD/MCI diagnosis." NeuroImage **101**: 569-582.

Suk, H. I., S. W. Lee and D. Shen (2015). "Latent feature representation with stacked auto-encoder for AD/MCI diagnosis." Brain Structure and Function **220**: 841-859.

Suk, H. I. and D. Shen (2013). Deep Learning Based Feature Representation for AD/MCI Classification. Medical Image Computing and Computer-Assisted Intervention (MICCAI), 16th International Conference. **8150:** 583-590.

Sun, Q.-S., S.-G. Zeng, Y. Liu, P.-A. Heng and D.-S. Xia (2005). "A new method of feature fusion and its application in image recognition." Pattern Recognition **38**(12): 2437-2448.

Szegedy, C., W. Liu, Y. Jia, P. Sermanet, S. Reed, D. Anguelov, D. Erhan, V. Vanhoucke and A. Rabinovich (2015). Going deeper with convolutions(Inception, GoogLeNet). Proceedings of the IEEE Computer Society Conference on Computer Vision and Pattern Recognition. **07-12-June:** 1-9.

Tagliazucchi, E. and H. Laufs (2014). "Decoding wakefulness levels from typical fMRI resting-state data reveals reliable drifts between wakefulness and sleep." Neuron **82**(3): 695-708.

Tagliazucchi, E., F. von Wegner, A. Morzelewski, V. Brodbeck and H. Laufs (2012). "Dynamic BOLD functional connectivity in humans and its electrophysiological correlates." Front Hum Neurosci **6**: 339.

Theiler, J., S. Eubank, A. Longtin, B. Galdrikian and J. Doyne Farmer (1992). "Testing for nonlinearity in time series: the method of surrogate data." Physica D: Nonlinear Phenomena **58**(1): 77-94.

Thompson, G. J., M. D. Merritt, W.-J. Pan, M. E. Magnuson, J. K. Grooms, D. Jaeger and S. D. Keilholz (2013). "Neural correlates of time-varying functional connectivity in the rat." NeuroImage **83**: 826-836.

Thompson, P. M., C. Vidal, J. N. Giedd, P. Gochman, J. Blumenthal, R. Nicolson, A. W. Toga and J. L. Rapoport (2001). "Mapping adolescent brain change reveals dynamic wave of accelerated gray matter loss in very early-onset schizophrenia." Proc Natl Acad Sci U S A **98**(20): 11650-11655.

References

Turner, J. A., V. D. Calhoun, A. Michael, T. G. van Erp, S. Ehrlich, J. M. Segall, R. L. Gollub, J. Csernansky, S. G. Potkin, B. C. Ho, J. Bustillo, S. C. Schulz, Fbirn and L. Wang (2012). "Heritability of multivariate gray matter measures in schizophrenia." Twin Res Hum Genet **15**(3): 324-335.

Tzourio-Mazoyer, N., B. Landeau, D. Papathanassiou, F. Crivello, O. Etard, N. Delcroix, B. Mazoyer and M. Joliot (2002). "Automated anatomical labeling of activations in SPM using a macroscopic anatomical parcellation of the MNI MRI single-subject brain." Neuroimage **15**(1): 273-289.

Ulaş, A., U. Castellani, P. Mirtuono, M. Bicego, V. Murino, S. Cerruti, M. Bellani, M. Atzori, G. Rambaldelli, M. Tansella and P. Brambilla (2011). Multimodal Schizophrenia Detection by Multiclassification Analysis. Progress in Pattern Recognition, Image Analysis, Computer Vision, and Applications: 16th Iberoamerican Congress, CIARP 2011, Pucón, Chile, November 15-18, 2011. Proceedings. C. San Martin and S.-W. Kim. Berlin, Heidelberg, Springer Berlin Heidelberg**:** 491-498.

Ulloa, A., S. Plis, E. Erhardt and V. Calhoun (2015). Synthetic structural magnetic resonance image generator improves deep learning prediction of schizophrenia. 2015 IEEE 25th International Workshop on Machine Learning for Signal Processing (MLSP).

Uludag, K. and A. Roebroeck (2014). "General overview on the merits of multimodal neuroimaging data fusion." Neuroimage **102 Pt 1**: 3-10.

Unger, J. W., L. W. Lapham, T. H. McNeill, T. A. Eskin and R. W. Hamill (1991). "The amygdala in Alzheimer's disease: Neuropathology and Alz 50 Immunoreactivity." Neurobiology of Aging **12**: 389-399.

van den Brink, R. L., T. Pfeffer, C. M. Warren, P. R. Murphy, K.-D. Tona, N. J. A. van der Wee, E. Giltay, M. S. van Noorden, S. A. R. B. Rombouts, T. H. Donner and S. Nieuwenhuis (2016). "Catecholaminergic Neuromodulation Shapes Intrinsic MRI Functional Connectivity in the Human Brain." The Journal of Neuroscience **36**(30): 7865-7876.

References

van den Heuvel, M. P., R. C. Mandl, R. S. Kahn and H. E. Hulshoff Pol (2009). "Functionally linked resting-state networks reflect the underlying structural connectivity architecture of the human brain." Hum Brain Mapp **30**(10): 3127-3141.

Van Dijk, K. R., T. Hedden, A. Venkataraman, K. C. Evans, S. W. Lazar and R. L. Buckner (2010). "Intrinsic functional connectivity as a tool for human connectomics: theory, properties, and optimization." J Neurophysiol **103**(1): 297-321.

Vieira, S., W. H. L. Pinaya and A. Mechelli (2017). Using deep learning to investigate the neuroimaging correlates of psychiatric and neurological disorders: Methods and applications. Neuroscience and Biobehavioral Reviews. **74:** 58-75.

Visser, P. J., F. R. J. Verhey, P. A. M. Hofman, P. Scheltens and J. Jolles (2002). "Medial temporal lobe atrophy predicts Alzheimer's disease in patients with minor cognitive impairment." Journal of Neurology Neurosurgery and Psychiatry **72**: 491-497.

Walhovd, K. B., A. M. Fjell, J. Brewer, L. K. McEvoy, C. Fennema-Notestine, D. J. Hagler Jr, R. G. Jennings, D. Karow, A. M. Dale and A. s. D. N. Initiative (2010). "Combining MR imaging, positron-emission tomography, and CSF biomarkers in the diagnosis and prognosis of Alzheimer disease." AJNR.American journal of neuroradiology **31**: 347-354.

Wang, C., J. L. Ong, A. Patanaik, J. Zhou and M. W. L. Chee (2016). "Spontaneous eyelid closures link vigilance fluctuation with fMRI dynamic connectivity states." Proceedings of the National Academy of Sciences **113**(34): 9653-9658.

Weiner, M. W., D. P. Veitch, P. S. Aisen, L. A. Beckett, N. J. Cairns, R. C. Green, D. Harvey, C. R. Jack, W. Jagust, J. C. Morris, R. C. Petersen, A. J. Saykin, L. M. Shaw, A. W. Toga and J. Q. Trojanowski (2017). Recent publications from the Alzheimer's Disease Neuroimaging Initiative: Reviewing progress toward improved AD clinical trials. Alzheimer's and Dementia. **13:** e1-e85.

Whitwell, J. L., M. M. Shiung, S. A. Przybelski, S. D. Weigand, D. S. Knopman, B. F. Boeve, R. C. Petersen and C. R. Jack (2008). "MRI patterns of atrophy associated with progression to AD in amnestic mild cognitive impairment." Neurology **70**: 512-520.

References

Wilkins, C. H., K. L. Wilkins, M. Meisel, M. Depke, J. Williams and D. F. Edwards (2007). "Dementia undiagnosed in poor older adults with functional impairment." Journal of the American Geriatrics Society **55**: 1771-1776.

Xie, S., R. Girshick, P. Dollár, Z. Tu and K. He (2017). Aggregated residual transformations for deep neural networks. Proceedings - 30th IEEE Conference on Computer Vision and Pattern Recognition, CVPR 2017. **2017-Janua:** 5987-5995.

Xu, L., K. M. Groth, G. Pearlson, D. J. Schretlen and V. D. Calhoun (2009). "Source-Based Morphometry: The Use of Independent Component Analysis to Identify Gray Matter Differences With Application to Schizophrenia." Human brain mapping **30**(3): 711-724.

Xu, L., G. Pearlson and V. D. Calhoun (2009). "Joint source based morphometry identifies linked gray and white matter group differences." NeuroImage **44**(3): 777-789.

Yaesoubi, M., E. A. Allen, R. L. Miller and V. D. Calhoun (2015). "Dynamic coherence analysis of resting fMRI data to jointly capture state-based phase, frequency, and time-domain information." Neuroimage **120**: 133-142.

Yaesoubi, M., R. L. Miller and V. D. Calhoun (2015). "Mutually temporally independent connectivity patterns: A new framework to study the dynamics of brain connectivity at rest with application to explain group difference based on gender." NeuroImage **107**: 85-94.

Yang, H., J. Liu, J. Sui, G. Pearlson and V. D. Calhoun (2010). "A Hybrid Machine Learning Method for Fusing fMRI and Genetic Data: Combining both Improves Classification of Schizophrenia." Frontiers in Human Neuroscience **4**: 192.

Yang, Z., R. C. Craddock, D. S. Margulies, C. G. Yan and M. P. Milham (2014). "Common intrinsic connectivity states among posteromedial cortex subdivisions: Insights from analysis of temporal dynamics." Neuroimage **93 Pt 1**: 124-137.

Yu, Q., E. B. Erhardt, J. Sui, Y. Du, H. He, D. Hjelm, M. S. Cetin, S. Rachakonda, R. L. Miller, G. Pearlson and V. D. Calhoun (2015). "Assessing dynamic brain graphs of time-varying connectivity in fMRI data: application to healthy controls and patients with schizophrenia." Neuroimage **107**: 345-355.

References

Yu, Q., J. Sui, S. Rachakonda, H. He, G. Pearlson and V. D. Calhoun (2011). "Altered Small-World Brain Networks in Temporal Lobe in Patients with Schizophrenia Performing an Auditory Oddball Task." Frontiers in Systems Neuroscience **5**: 7.

Yun, H. J., K. Kwak and J. M. Lee (2015). "Multimodal discrimination of Alzheimer's disease based on regional cortical atrophy and hypometabolism." PLoS ONE **10**.

Zalesky, A. and M. Breakspear (2015). "Towards a statistical test for functional connectivity dynamics." NeuroImage **114**: 466-470.

Zalesky, A., A. Fornito, L. Cocchi, L. L. Gollo and M. Breakspear (2014). "Time-resolved resting-state brain networks." Proceedings of the National Academy of Sciences **111**(28): 10341-10346.

Zeiler, M. D. and R. Fergus (2014). "Visualizing and Understanding Convolutional Networks arXiv:1311.2901v3 [cs.CV] 28 Nov 2013." Computer Vision–ECCV 2014 **8689**: 818-833.

Zuo, X. N., C. Kelly, J. S. Adelstein, D. F. Klein, F. X. Castellanos and M. P. Milham (2010). "Reliable intrinsic connectivity networks: test-retest evaluation using ICA and dual regression approach." Neuroimage **49**(3): 2163-2177.

Zuo, X. N. and X. X. Xing (2014). "Test-retest reliabilities of resting-state FMRI measurements in human brain functional connectomics: a systems neuroscience perspective." Neurosci Biobehav Rev **45**: 100-118.